



TECHNISCHE
UNIVERSITÄT
WIEN

Local Currents in Granular High Temperature Superconductors

DISSERTATION

Ausgeführt zum Zwecke der Erlangung des akademischen Grades
Doktor der technischen Wissenschaften

eingereicht an der Technischen Universität Wien
Fakultät für Physik

von

Dipl.-Ing. Sigrid Kagerbauer, geb. Holleis

Matrikelnummer: 0826686

unter der Leitung von
Privatdoz. Dipl.-Ing. Dr.techn. Michael Eisterer

E141
Atominstitut

Wien, 8. September 2022

Abstract

Coated conductors based on high temperature superconducting (HTS) materials are a viable alternative to conventional superconductors for high-field applications such as magnets for particle accelerators or future fusion reactors. The search for cheap and simple production techniques as well as the optimization of the current carrying capacity of these conductors is an ongoing process. Granularity is one of the main performance limitations in HTS materials and the production of coated conductors is demanding and expensive due to stringent texture requirements. Scanning Hall probe microscopy (SHPM) in combination with electron microscopy (EM) allows for a detailed investigation of local current limitations such as grain boundaries and inhomogeneities in the superconducting layer.

In this thesis, the investigations on the global and local current carrying capabilities of three different HTS materials are presented, ranging from highly-developed YBCO films on commercial technical templates and novel attempts of Fe(Se,Te) films on metallic tapes with simple architectures to early-stage samples of lesser studied thallium-based films. Using local current density maps, obtained by high-resolution SHPM, a quantitative statistical analysis of the magnetic granularity was developed.

Undoped and BHO-doped YBCO films with thicknesses from 250 nm to 2 μm , deposited on RABiTS and IBAD-MgO based templates were studied. BHO-doping presents a promising route for the optimization of YBCO films, as the macroscopic critical current density, J_c , is enhanced and its field dependence is reduced due to the introduction of artificial pinning centers. The investigations with SHPM and EM show that the higher J_c can also be attributed to an enhanced film growth with the reduction of porosity and refinement of secondary phases which leads to a reduction of granularity with doping and film thickness. High local currents were

measured in the films on RABiTS that show the potential for further optimization of YBCO films based on this template type.

The relaxed texture requirements of iron-based superconductors fuel hope for the realization of cheap coated conductors. Therefore, Fe(Se,Te) films on RABiTS templates with a single buffer layer were studied and SHPM measurements show the magnetic granularity of these films. EM analysis reveals that, similar to YBCO, the out-of-plane orientation of underlying Ni-W grains in the substrate has a severe impact on the growth of Fe(Se,Te) films.

Early-stage Tl-1223 films on textured silver and single crystalline substrate were studied in order to assess the feasibility of this compound as a coating in the FCC beam screen. Promising high critical temperatures and high local current densities were found, however, the film growth has to be optimized in order to achieve a better phase purity and film coverage on the substrate.

Kurzfassung

Auf hochtemperatursupraleitenden (HTS) Materialien basierende Bandleiter stellen eine vielversprechende Alternative zu konventionellen Supraleitern für Hochfeldanwendungen, wie beispielsweise Magnete für Teilchenbeschleuniger oder zukünftige Fusionsreaktoren, dar. Dafür werden laufend einfache und billige Produktionstechniken gesucht und die Optimierung der Strombelastbarkeit der Bandleiter wird erforscht. Der Stromtransport in HTS Materialien wird hauptsächlich durch die Granularität begrenzt, dadurch sind aufwendige und teure Texturverfahren für Bandleiter notwendig um limitierende Korngrenzen im Supraleiter möglichst zu vermeiden. Mittels Rasterhallsondenmikroskopie kombiniert mit Elektronenmikroskopie können lokale Strombegrenzungen und Inhomogenitäten in der supraleitenden Schicht optimal untersucht werden.

In dieser Arbeit werden die lokalen und globalen Stromtransportfähigkeiten von drei sehr unterschiedlichen HTS Materialien präsentiert. Es wurden hochentwickelte YBCO Filme auf kommerziellen metallischen Substraten, neuartige Fe(Se,Te) Filme auf einfachen und billigen metallischen Substraten, sowie wenig erforschte Thallium-basierte Filme untersucht. Dabei wurde aus lokalen Stromdichteverteilungen eine quantitative statistische Analyse der magnetischen Granularität entwickelt.

Es wurden undotierte und BHO-dotierte YBCO Filme auf RABiTS- und IBAD-MgO-basierten Substraten mit supraleitenden Schichtdicken von 250 nm bis 2 μ m untersucht. Das Dotieren mit BHO ist eine vielversprechende Strategie zur Optimierung von YBCO Filmen, da die makroskopische kritische Stromdichte durch zusätzliche Verankerungszentren erhöht wird. Die Untersuchungen mit Rasterhallsonden- und Elektronenmikroskopie zeigen, dass das Dotieren mit BHO zu einem besseren Schichtwachstum und weiters zu einer Reduktion der magnetischen Granularität führt, da weniger Fremdphasen und Löcher in der supraleitenden Schicht zu finden sind.

Die hohen gemessenen Ströme in den YBCO Filmen auf RABiTS zeigen das Potential für die weitere Entwicklung von supraleitenden Schichten auf diesem Substrattyp auf.

Experimente haben gezeigt, dass Eisensupraleiter weniger aufwendig texturiert werden müssen, daher hofft man auf die Produktion von billigen Bandleitern. Dazu wurden Fe(Se,Te) Filme auf einfachen RABiTS Substraten mit nur einer Pufferschicht untersucht, allerdings zeigen die Hall-Messungen auch in diesen Filmen eine hohe magnetische Granularität. Anhand von Elektronenmikroskopie Analysen sieht man, dass die Orientierung von einzelnen Substratkörnern einen starken Einfluss auf das Wachstum der supraleitenden Schicht hat.

Erste Tl-1223 Filme auf texturierten Silbersubstraten und Einkristallen wurden im Rahmen eines CERN Projektes untersucht. Tl-1223 könnte als supraleitende Beschichtung des Strahlrohrs eines neuen Teilchenbeschleunigers dienen. Auch in diesem Material wurden hohe lokale Stromdichten gemessen, allerdings muss die Probenherstellung noch optimiert werden, um eine bessere Phasenreinheit und durchgehende supraleitende Schicht zu erreichen.

Acknowledgments

I want to thank my advisor Michael Eisterer for supporting the research for this thesis and for all the good and productive discussions we had over the years. I learned a lot and my time working in his research group will always bring back happy memories. Thank you also for all the conferences and project meetings we attended together, whether it was in Geneva, Berlin, Genoa, Amsterdam, Barcelona, Seattle, Brussels, Glasgow, Santa Margherita Ligure or Dresden, we always had a good time together with international colleagues. I want to thank all my colleagues at the Atominstitut: Franz, Thomas, Hannes, May, David, Murph, David, Mattia, Raphael, Flo and Alex. Thank you for all the good times we had together in the office, in the lab and at every party.

I want to thank Johannes Bernardi for all the hours we spent together at the TEM, for supporting my research on the microstructure of superconductors and for all the electron microscopy workshops and conferences we attended together. Thanks also to the entire USTEM team for the fruitful discussions and for teaching me how to operate the various electron microscopy systems.

I wish to thank Ruben Hühne and his team at the IFW Dresden for the preparation of samples and for the productive collaboration that led to the bigger part of this thesis.

I want to express my gratitude to Judy Wu and John Durrell for taking the time and effort to review this thesis.

I want to thank my family and friends for the continuous mental support during my time of research and writing.

Finally, I want to thank my colleague, my best friend and now my husband Daniel for always supporting me in every possible way and for accepting me and loving me for who I am.

I love you with all my heart.

Nomenclature

The following list describes frequently used acronyms and symbols in this work. If not stated otherwise, SI units are used throughout this thesis.

Acronyms

ABF	Annular bright field
BSE	Backscattered electron
EBS	Electron backscatter diffraction
EDX	Energy dispersive X-ray analysis
FCC	Future circular collider
FIB	Focused ion beam
GB	grain boundary
HAADF	High-angle annular dark field
HTS	High temperature superconductivity/superconductor
IBAD	Ion beam assisted deposition
IBS	Iron-based superconductors
IPF	Inverse pole figure
PLD	Pulsed laser deposition

RABiTS	Rolling assisted biaxially textured substrate
SEM	Scanning electron microscopy/microscope
SE	Secondary electron
SHPM	Scanning Hall probe microscopy
SQUID	Superconducting quantum interference device
STEM	Scanning transmission electron microscopy
TEM	Transmission electron microscopy/microscope
TKD	Transmission Kikuchi diffraction

Symbols

χ	magnetic susceptibility
μ	mean local critical current density
σ_n	relative standard deviation of the local critical current density
J_x	local critical current density in the x -direction
J_y	local critical current density in the y -direction
J_c^G	global critical current density
J_c^L	local critical current density
m	magnetic moment
m_{irr}	irreversible magnetic moment
T_c	critical temperature

List of Tables

3.1	T_c and J_c^G in self-field of BHO-doped and pure YBCO films.	36
3.2	Mean J_c^L values and relative standard deviation of YBCO films on RABiTS.	43
3.3	Thickness, buffer layers and substrate architectures of Fe(Se,Te) films.	62

List of Figures

1.2.1	Common grain boundaries in a superconducting thin film.	7
1.3.1	Schematic structure of RABiTS and IBAD-MgO coated conductors.	8
2.2.1	AC susceptibility measurement of a superconducting thin film.	12
2.2.2	Typical magnetization hysteresis loop and calculated global critical current density.	12
2.2.3	Wide area Hall scanner.	14
2.2.4	Bean's critical state model.	15
2.2.5	Typical measurement of a remnant field profile at 77 K.	16
2.2.6	Laser cutter set up.	16
2.2.7	Lasered and magnetically detected polar bear.	17
2.2.8	Micro Hall scanner.	18
2.2.9	Digital light microscope: surface roughness and tilt.	19
2.2.10	Typical measurement of a remnant field profile at 5 K.	19
2.2.11	Coordinate system of the inversion algorithm.	21
2.2.12	Typical local current density maps at 77 K and 5 K.	22
2.2.13	Area selection of J_c^L -matrix for statistical analysis.	23
2.2.14	Histogram plots of the local critical current density values.	23
2.3.1	Interaction volume in a scanning electron microscope.	25
2.3.2	Comparison between secondary electron image and backscattered electron image.	25
2.3.3	Preparation of a TEM lamella using a focused ion beam.	27
2.3.4	Operation modes of a transmission electron microscope.	28
2.3.5	Bright field imaging and dark field imaging in TEM mode.	29

2.3.6	Diffraction pattern and high-resolution imaging in TEM mode.	30
2.3.7	Annular bright field and high-angle annular dark field imaging in STEM mode.	30
2.3.8	Typical EDX spectrum.	32
2.3.9	Example of EDX elemental mapping.	32
2.3.10	Experimental setup for EBSD and TKD.	33
3.1.1	T_c of pure and BHO-doped YBCO films.	36
3.1.2	J_c^G of BHO-doped and pure YBCO films at 5 K, 30 K and 77 K.	37
3.1.3	Remnant field profiles at 77 K of BHO-doped and pure YBCO films.	39
3.1.4	Local current density maps at 77 K of BHO-doped and pure YBCO films.	39
3.1.5	High-resolution J_c^L maps of the 500 nm BHO-doped and pure YBCO films.	40
3.1.6	J_c^L distributions of the 500 nm BHO-doped and pure YBCO spots on RABiTS.	41
3.1.7	J_c^L distributions with respect to film thickness at 5 K.	42
3.1.8	J_c^L maps of the 2 μm BHO-doped YBCO spots.	42
3.1.9	Local current density maps of the YBCO films on IBAD-MgO templates.	44
3.1.10	J_c^L distributions of YBCO films on RABiTS and IBAD-MgO.	44
3.1.11	SEM images of all BHO-doped and pure YBCO films.	46
3.1.12	SEM images of the high- and low- J_c^L spots of the 2 μm BHO-doped film.	47
3.1.13	TEM images of spot 1 and spot 2 of the 2 μm BHO-doped film.	48
3.1.14	Overlay of current maps and SEM images for the 2 μm YBCO films.	49
3.1.15	TEM images of the lamella taken from the 2 μm pure YBCO film.	50
3.1.16	Overlay of current maps and SEM images for the 500 nm pure YBCO film.	51
3.1.17	Preparation of TEM lamellae across grain boundaries in the 500 nm films.	52
3.1.18	TEM images of the 500 nm pure YBCO film on RABiTS.	53
3.1.19	TEM images of the 500 nm BHO-doped film on RABiTS.	54
3.1.20	EBSD maps of the 500 nm BHO-doped and pure YBCO films on RABiTS.	56
3.1.21	Mean relative standard deviation versus doping, sample thickness and temperature.	58
3.1.22	Comparison of the J_c^L distributions at 5 K and 77 K.	60
3.2.1	AC susceptibility measurements of FST thin films on various substrates.	63
3.2.2	Global critical current density of FST films at 5 K.	64

3.2.3	Global critical current density of FST films at various temperatures.	65
3.2.4	Remnant field profiles of FST films at 5 K.	66
3.2.5	Digital light microscope images of FST films.	67
3.2.6	Local critical current density maps of FST films on RABiTS and IBAD-MgO.	68
3.2.7	J_c^L distributions of the FST films on RABiTS and IBAD-MgO.	68
3.2.8	SEM images of the surface morphology of FST films on RABiTS and IBAD-MgO.	69
3.2.9	Digital light microscope images of the FST film on RABiTS	70
3.2.10	Preparation of a FIB lamella across a grain boundary in the FST film.	71
3.2.11	TEM images of a lamella across a grain boundary in the FST film.	71
3.2.12	Diffraction pattern of the substrate GB in the FST film.	72
3.2.13	TKD maps of the FST film on RABiTS	73
3.2.14	SEM image of the Y_2O_3 buffer layer.	75
3.2.15	J_c^L distributions of the FST films compared to YBCO at 5 K.	76
3.3.1	AC susceptibility of a Tl-based film on Ag substrate.	78
3.3.2	Hall scans of a Tl-based sample on Ag substrate at 5 K.	79
3.3.3	Hall scans of a Tl-based sample on STO substrate at 5 K.	79
3.3.4	J_c^L map of a Tl-1223 grain cluster on STO substrate.	80
3.3.5	Digital light microscope images of a Tl-based film on Ag substrate.	80
3.3.6	EDX phase map of a Tl-based film on Ag substrate.	81
3.3.7	SEM images of a Tl-based film on STO substrate.	81
3.3.8	TEM images of the Tl-1223 film on STO substrate	82
A.1	J_c^G of BHO-doped and pure YBCO films at 65 K.	97
A.2	J_c^G of BHO-doped and pure YBCO films at various thicknesses and temperatures.	98
B.1	Remnant field maps and J_c^L maps of the BHO-doped YBCO films.	99
B.2	Remnant field maps and J_c^L maps of the pure YBCO films.	99
B.3	High-resolution maps of the 2 μ m BHO-doped spots on RABiTS.	100
B.4	High-resolution maps of the 1 μ m BHO-doped spots on RABiTS.	101
B.5	High-resolution maps of the 500 nm BHO-doped spots on RABiTS.	102
B.6	High-resolution maps of the 250 nm BHO-doped spots on RABiTS.	103

B.7	High-resolution maps of the 500 nm BHO-doped spots on IBAD-MgO.	104
B.8	High-resolution maps of the 2 μm pure spots on RABiTS.	105
B.9	High-resolution maps of the 1 μm pure spots on RABiTS.	106
B.10	High-resolution maps of the 500 nm pure spots on RABiTS.	107
B.11	High-resolution maps of the 250 nm pure spots on RABiTS.	108
B.12	High-resolution maps of the 1 μm pure spots on IBAD-MgO.	109
C.1	J_c^L distributions of the BHO-doped and pure YBCO spots.	110
D.1	TEM images of the 1 μm BHO-doped YBCO film.	111
D.2	TEM images of the 1 μm pure YBCO film.	112
D.3	TEM images of the 250 nm BHO-doped YBCO film.	113
D.4	TEM images of the 250 nm pure YBCO film.	114

Contents

Nomenclature	vi
List of Tables	vii
List of Figures	viii
1 Introduction	1
1.1 Motivation and Outline of this Thesis	3
1.2 Magnetic Properties and Granularity of HTS	5
1.3 Coated Conductors	7
2 Experimental Methods	9
2.1 Samples	9
2.2 Magnetic Characterization	11
2.2.1 SQUID Magnetometer	11
2.2.2 Wide Area Hall Scanner	13
2.2.3 Micro Hall Scanner	17
2.2.4 Local Current Density Distribution	20
2.3 Microstructural Characterization	24
2.3.1 Scanning Electron Microscopy	24
2.3.2 Focused Ion Beam	26
2.3.3 Transmission Electron Microscopy	27
2.3.4 Analytical Electron Microscopy	31

3 Results and Discussion	34
3.1 YBCO	34
3.1.1 Experimental Results	35
3.1.1.1 Superconducting Properties: Macroscopic Magnetic Properties	35
3.1.1.2 Superconducting Properties: Magnetic Granularity	38
3.1.1.3 Microstructure	45
3.1.2 Discussion	57
3.2 Fe(Se,Te)	61
3.2.1 Experimental Results	61
3.2.1.1 Superconducting Properties	62
3.2.1.2 Microstructure	69
3.2.2 Discussion	73
3.3 Tl-1223	77
3.3.1 Experimental Results	77
3.3.1.1 Superconducting Properties	77
3.3.1.2 Microstructure	80
3.3.2 Discussion	83
4 Conclusion and Outlook	84
Bibliography	87
Appendix	97
A YBCO - Macroscopic Magnetic Properties	97
B YBCO - High-resolution SHPM	99
C YBCO - Statistical Analysis	110
D YBCO - TEM	111

Chapter 1

Introduction

Since the discovery of high temperature superconductivity (HTS) in the cuprates in 1986 [1], many possible applications have been envisioned for this material class. They exhibit a high critical temperature of up to 130 K and a high upper critical field, which makes them a viable alternative to conventional superconductors like NbTi and Nb₃Sn for high-field magnets in particle accelerators and future fusion reactors [2–9]. Furthermore, due to their ability to carry nearly loss-free currents over large distances, and the fact, that cooling with cheap and abundant liquid nitrogen is sufficient, other potential applications range from power transmission cables to magnetic energy-storage devices, transformers, fault current limiters and motors [10, 11]. However, for all these power applications the superconducting material needs to be formed into a long, strong and flexible conductor, which is a demanding and expensive procedure due to the brittle nature of the ceramic HTS materials [12]. Two main routes have been established for the preparation of cuprate-based high performance conductors, namely multifilamentary wires of the Bi-Sr-Ca-Cu-O (BiSCCO) family, prepared by the powder in tube method where superconducting filaments are stacked in a silver sheath [13, 14], and coated conductors based on the (RE)Ba₂Cu₃O_{7-δ} (RE = rare earth element, REBCO) family where a thin layer of superconducting material is deposited on metallic templates [15–17]. The most popular established routes for the production of such coated conductors are the use of rolling assisted biaxially textured substrates (RABiTS) of Ni-W based alloys [18], and the growth of textured buffer layers by ion

beam assisted deposition (IBAD) on stainless steel or Hastelloy substrates [19]. At the moment, REBCO-based coated conductors are the highest performing HTS wires and the optimization of their current carrying capacity is an ongoing process. A promising route for the increase of their performance is the introduction of artificial pinning centers such as BaMO_3 ($M =$ (transition) metal, e.g. Zr, Hf, Ir, Sn) perovskites, as well as Ba_2YNbO_6 (BYNO) and Ba_2YTaO_6 (BYTO) double perovskites and the mixed compound BYNTO [20–32]. These materials are known to self-assemble into c -axis oriented nanorods or platelets in the ab -plane with a typical diameter or thickness of a few nanometers. It was found that the incorporation of BaHfO_3 (BHO) leads to smaller nanorods compared to the other perovskites and therefore to effective vortex pinning at low temperatures and high magnetic fields [33]. The addition of BHO also leads to a negligible decrease in the critical temperature which is beneficial for the performance at liquid nitrogen temperatures [34].

One of the main performance limitations of HTS materials is granularity and conductors are expensive due to stringent texture requirements. While BiSCCO-based conductors only need a uniaxial texture which can be easily obtained by thermo-mechanical treatments of the substrate, REBCO-based conductors require a complex biaxial texturing process. It was found, that the inter-granular current density strongly depends on the misalignment of adjacent grains in this material. As a result, the macroscopic critical current density is severely reduced by even moderate misalignment angles [35, 36]. Both these compound families have their advantages and disadvantages, however, some applications require even more than what these two cuprates can offer. The future circular collider (FCC) study, for example, presented a conceptual design for a next generation particle accelerator at the CERN site [37]. In this collider, the protons are steered by 16 T dipole magnets inside a beam screen, which is held at a temperature of 50 K for cryogenic efficiency. Copper, which is the beam screen coating in the Large Hadron Collider (LHC), exhibits a much too high surface resistance under these extreme operation conditions in order to guarantee a stable proton beam. The only known materials to have a smaller surface resistance at 50 K are HTS materials. A coating made of BiSCCO cannot be realized due to the high anisotropy of the material which limits the applicability at high magnetic fields to temperatures below 20 K and the tubular geometry of the beam screen does not allow a direct coating with REBCO due to the required biaxial texture. While the use of commercially available

REBCO coated conductors inside the beam screen is being studied [38], another, technologically less exploited, compound of the cuprate family has also been proposed for this application, namely the thallium-based compounds [39, 40]. Especially the $\text{Tl}(\text{Bi,Pb})\text{Sr}(\text{Ba})\text{CaCuO}$ (Tl-1223) compound exhibits a low anisotropy, similar to the REBCO-based compounds, and one of the highest known transition temperatures at ambient pressure of about 125 K. At the same time, Tl-1223 is crystallographically similar to the BiSCCO-based HTS and has a tendency to establish a uniaxial texture when grown on untextured silver [41, 42]. This material may therefore have the potential to combine the strengths of REBCO and BiSCCO.

Another big family of HTS materials appeared with the discovery of iron-based superconductors (IBS) in 2008 [43], which shortly after led to the discovery of numerous different compounds of this new class of high temperature superconductors. While the IBS compounds exhibit lower critical temperatures of up to 40 K, the upper critical field is similarly high to that of the cuprates [44], which makes them a viable candidate for high-field applications at low operating temperatures [45, 46]. Furthermore, due to the metallic nature of the IBS, the production of tapes and wires is easier compared to the brittle ceramic cuprates. The texture requirement seems relaxed, as this material class allows for higher misalignment angles between adjacent grains before the current across the respective grain boundary (GB) is substantially suppressed [44, 47, 48]. This fuels hope for the cheap production of powder-in-tube wires [49–51] or coated conductors with simple architectures [52–58] based on this material class.

1.1 Motivation and Outline of this Thesis

The main goal of this thesis was to gain a better understanding of the local current transport in HTS materials, relate limitations of the critical current to microstructural features and investigate the subsequent implications on the macroscopic critical current density. The investigations on three very different HTS materials in the form of superconducting thin films are presented here and range from the highly developed cuprate superconductor $\text{YBa}_2\text{Cu}_3\text{O}_{7-\delta}$ (YBCO) and the well-studied iron-based superconductor $\text{FeSe}_{0.5}\text{Te}_{0.5}$ (Fe(Se,Te)) to early-stage samples of the known but technologically unexploited superconductor $\text{Tl}(\text{Bi,Pb})\text{Sr}(\text{Ba})_2\text{Ca}_2\text{Cu}_3\text{O}_{9+x}$ (Tl-1223).

The magnetic measurements that were performed for this thesis, as well as the microstruc-

tural analysis are described in Chapter 2. Scanning Hall probe microscopy (SHPM) is a powerful tool for the investigation of magnetic granularity and in combination with scanning and transmission electron microscopy (SEM/TEM), the current flow in superconducting grains and across grain boundaries can be related to local defects and inhomogeneities in the film growth. The importance of this analysis method for applications was demonstrated in [59], where we investigated commercial YBCO tapes on their quench behavior for superconducting fault current limiters. Images of the YBCO tape in a liquid nitrogen bath were taken with a high-speed camera in order to record the first milliseconds during a quench. The recordings revealed lines of bubbles along the tape where energy dissipation occurred first. With SHPM, we could identify these lines as areas of inhomogeneous current flow and with SEM we found disturbances in the superconducting film growth at the positions where the first bubbles are generated.

The experimental results on the three HTS materials, as well as a discussion on the findings for each material, are presented in Chapter 3. The first section describes the experiments that were performed on undoped and BHO-doped YBCO films of various thicknesses on technical templates. Previous works have shown that pulsed laser deposited YBCO films on RABiTS templates result in a superconducting layer that closely follows the granular nature of the underlying Ni-W grains with varying porosity and grooved grain boundaries which leads to a high degree of magnetic granularity in these films [60]. Furthermore, it was found, that the addition of artificial pinning centers such as BHO leads to a denser microstructure of the superconducting film and an increase in the macroscopic critical current density [24, 61–63]. The results presented in this thesis concentrate on the effects of doping, film thickness and temperature on the magnetic granularity and introduce a quantitative statistical evaluation of the granularity for a more comprehensive understanding of the beneficial effects of BHO-doping.

The second section shows results on Fe(Se,Te) films on technical templates and single crystalline substrates. It was shown, that iron-based superconductors allow for a higher misalignment angle between neighboring grains, before the macroscopic critical current density is heavily suppressed [44, 47, 48]. This fuels hope for the production of cheap coated conductors with simple architectures. Conventional IBAD-MgO and RABiTS metal tapes have many buffer and diffusion layers underneath the superconducting film in order to achieve the required texture. To reduce the complexity, it was attempted to deposit Fe(Se,Te) films directly on Invar substrates,

however, the resulting films were not superconducting due to nickel poisoning [58]. Other experiments demonstrated the successful growth of Fe(Se,Te) on RABiTS templates using a single CeO₂ buffer layer [58]. In this thesis, the magnetic granularity of Fe(Se,Te) films on RABiTS with a single Y₂O₃ layer is investigated and prospects of the RABiTS route for IBS coated conductors are discussed.

The third section shows results of early-stage Tl-1223 samples that were prepared to study the feasibility of this material to substitute the standard copper coating in the beam screen of the future circular collider at CERN. Especially the sample preparation by electrochemical solution is a cheap and scalable technique that could be considered for direct deposition on the tubular surface of the beam screen.

Finally, Chapter 4 presents the conclusions and a future outlook. The most important findings of this thesis were published in [40, 64, 65].

1.2 Magnetic Properties and Granularity of HTS

All HTS materials are so-called type-II superconductors and their macroscopic behavior, such as the response to an external magnetic field, is described by the Ginzburg-Landau theory [66]. The theory introduces two characteristic lengths, namely the magnetic penetration depth, λ , and the superconducting coherence length, ξ , which define the lower and upper critical field, H_{c1} and H_{c2} , respectively. For very small magnetic fields, $H < H_{c1}$, all magnetic field is expelled and the superconductor is in the Meissner phase, similar to a type-I superconductor. For higher fields $H > H_{c1}$, the magnetic field enters the superconductor from the surface in the form of flux lines (vortices). The superconducting state breaks down at fields higher than H_{c2} , which is substantially higher than the thermodynamical critical field which limits superconductivity in type-I superconductors, making high-field applications possible. In a simplified version, the structure of a flux line can be described as a normal conducting core with a radius of the order of ξ surrounded by an area of shielding currents with a radius of approximately λ . In reality, the density of superconducting electrons is zero only in the center of the flux line and increases on the length scale of ξ in radial direction to its equilibrium value. If a current is applied to a type-II superconductor, a Lorentz force acts on these flux lines which start to move, causing a dissipation

of energy which leads to a resistance. In order to achieve a dissipation-free current transport the flux lines need to be effectively pinned. Technical type-II superconductors exhibit defects, such as nanoparticles, dislocations and planar defects, which act as pinning centers for vortices and keep them from moving. This so-called vortex pinning is therefore an essential concept in order to achieve high critical current densities for applications. The critical current, which is the maximum current a superconductor can carry, can be determined directly by applying an increasing current and measuring the resistance of a sample. Alternatively, the critical current can be determined indirectly by magnetization measurements, where the critical current density, J_c , corresponds to the flux line density gradient inside the sample. A phenomenological model for the calculation of J_c from magnetization measurements was developed by Bean [67] and is described in more detail in Chapter 2.2.2. Both measurement methods give information on the macroscopic critical current of a superconductor. For the investigation of granular superconductors, a local measurement method such as scanning Hall probe microscopy is more meaningful and the critical current density can be determined by an inversion of Biot Savart's law [68], as described in Chapter 2.2.4.

The fundamental problem of granularity in HTS materials arises from the fact, that applications usually require long length conductors and single crystals cannot be grown in such lengths. Therefore, polycrystalline wires where the supercurrent has to cross many grain boundaries (GBs) are inevitable [69]. In a superconducting material, many nuclei are present during the transformation from the precursor phase to the desired superconducting phase. As a consequence a network of GBs is formed in the material which influences the current transport in a superconducting sample. If the GBs are not obstructive, the current can flow in the entire sample. If, however, the GBs block the current, many small current loops are formed. The current transport in HTS materials therefore has to be differentiated into the inter-grain or global current, i.e. the current flowing from one grain to the next, and the intra-grain current, i.e. the current flowing inside a superconducting grain. In order to study the behavior of currents passing from one grain to another grain over a GB, many bicrystal experiments were performed [35, 48]. It was found that, above a certain misalignment angle between the grains, the GBs form so-called Josephson junctions or weak-links, and the global critical current density is heavily suppressed. An exponential decrease of J_c was observed, when the GB misorientation angle exceeds a critical angle

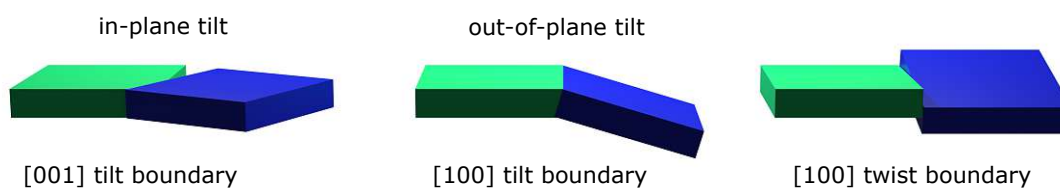


Figure 1.2.1: Common grain boundaries in a superconducting thin film. The [001] tilt boundary shows an in-plane tilt between two grains, while the [100] tilt boundary and [100] twist boundary show the out-of-plane tilt between grains.

which may be as low as 3° – 5° in cuprate superconductors [35, 36]. Experiments on iron-based superconductors suggest a much higher critical angle of 9° in this material class [48].

Grain boundaries can be classified by the rotation along a certain axis. Some examples, which are typically found in epitaxially grown HTS films, are shown in Figure 1.2.1. The [001] tilt grain boundary exhibits a so-called in-plane tilt, where the c -axis of the crystal is the rotation axis and the angle between the differently oriented ab -planes of both grains define the misalignment. In the case of the [100] tilt boundary, the rotation axis is along the GB itself and the misalignment angle is defined as the difference in orientation of the c -axis of the grains, i.e. an out-of-plane tilt. The [100] twist boundary also exhibits an out-of-plane tilt, only in this case the rotation axis is perpendicular to the GB. While all three types of GBs have detrimental effects on the macroscopic critical current density above a certain GB misalignment angle, especially the out-of-plane tilt of underlying substrate grains can have a severe impact on the superconducting film growth.

1.3 Coated Conductors

To overcome the problem of granularity in REBCO materials, the coated conductor technology was developed where an epitaxial texture is imposed on the superconducting layer. The commercially available coated conductors are composed of metallic substrates with a thickness of about $50\ \mu\text{m}$, buffer layers with a thickness of a few nanometers, a REBCO layer of around $1\ \mu\text{m}$ as well as protection and stabilizer layers of silver and copper, respectively. Two main routes have been established for the production of coated conductors [36], a schematic of both types is shown

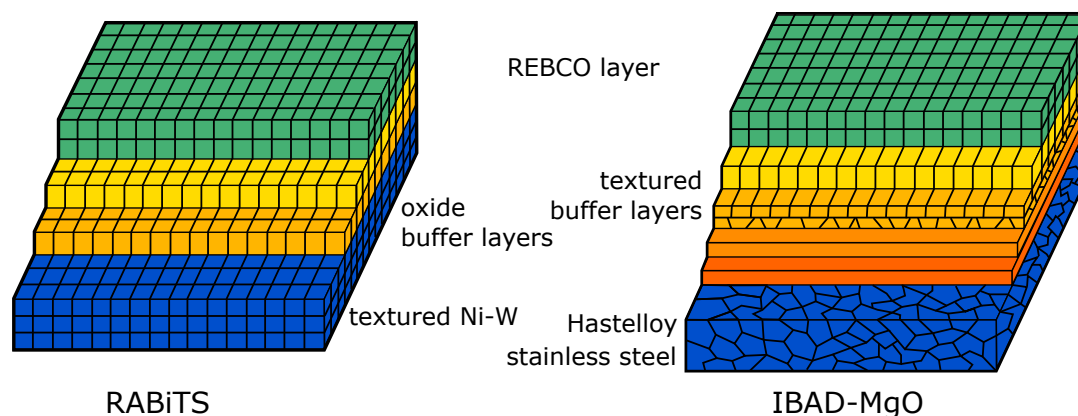


Figure 1.3.1: Schematic structure of RABiTS (left panel) and IBAD-MgO (right panel) coated conductors.

in Figure 1.3.1.

The first production method relies on the use of rolling assisted biaxially textured substrates (RABiTS) where the crystallographic preferential texture is generated via rolling and recrystallization of a Ni-W based alloy [18]. The alignment of the REBCO layer is achieved through epitaxial growth of subsequent layers onto the textured substrate. The buffer layers are usually oxides that reproduce and even improve the texture of the underlying substrate, however, many features of the grain boundaries in the REBCO layer are strongly influenced by the grain structure of the metallic template. The second production method uses ion beam assisted deposition (IBAD) where a preferred texture is generated in the buffer layers [19]. Polycrystalline stainless steel or Hastelloy is usually used as a substrate and many buffer layers are necessary for this type of coated conductor. The texture is usually achieved in the MgO buffer layer through the bombardment of the film with ions as it grows [70] and this layer is responsible for the texture in the subsequent layers and the superconducting film. Another technique, which also introduces the texture in the buffer layer, is the so-called inclined substrate deposition (ISD) where the deposition of the buffer layer is done with an inclination to the substrate normal [71]. Although in recent years the IBAD-MgO route has been the preferred choice for the production of coated conductors, superconducting thin films grown on RABiTS based templates offer a perfect playground for investigations on granularity.

Chapter 2

Experimental Methods

The goal of this thesis was to gain a better understanding of the relationship between superconducting properties and microstructure of HTS thin films. Usually, much information and knowledge is lost, if one person conducts the magnetization experiments and another person performs the microstructural characterization. For this reason, it was agreed, that I would study both areas of expertise and conduct or organize all experiments myself. By doing so, it was possible to determine an area of interest from a remnant magnetic field map and localize the same exact area in an electron image. The magnetic characterization was conducted at the Atominstitut, TU Wien under the guidance of Michael Eisterer and the microstructural characterization was performed using the instruments at the electron microscopy facility USTEM, TU Wien under the instruction of Johannes Bernardi.

2.1 Samples

Superconducting thin films of three different material compounds were investigated for this thesis. $\text{YBa}_2\text{Cu}_3\text{O}_{7-\delta}$ (YBCO) and $\text{FeSe}_{0.5}\text{Te}_{0.5}$ (FST) thin films were prepared via pulsed laser deposition (PLD) at IFW Dresden, while $\text{Tl}(\text{Bi,Pb})\text{Sr}(\text{Ba})_2\text{Ca}_2\text{Cu}_3\text{O}_{9+x}$ (Tl-1223) films were prepared by electrochemical deposition at CNR-SPIN.

For the preparation of the YBCO films two kinds of technical templates were used as substrates, namely a RABiTS Ni-9at.%W tape with a $\text{La}_2\text{Zr}_2\text{O}_7/\text{CeO}_2$ buffer layer system (pro-

vided by Deutsche Nanoschicht GmbH) and a Hastelloy tape with a $\text{Al}_2\text{O}_3/\text{Y}_2\text{O}_3/\text{IBAD-MgO}/\text{MgO}/\text{LaMnO}_3/\text{Gd:CeO}_2$ buffer layer architecture (provided by S-Innovations). The pulsed laser deposition was done with a KrF excimer laser with a wavelength of $\lambda = 248$ nm with a laser repetition rate of 5 Hz. The number of pulses was 2500, 5000, 10 000 and 20 000, which corresponds to film thicknesses of 250 nm, 500 nm, 1 μm and 2 μm , respectively. Undoped and 10 % BHO-doped YBCO films were prepared in a 0.4 mbar oxygen atmosphere and the temperature of the substrate was kept at 810 °C. The samples were then annealed for a short time at an oxygen partial pressure of 400 mbar at 765 °C to compensate for oxygen loss during film growth. Finally, the YBCO films were cooled to room temperature at a rate of 10 °C/min.

For the preparation of FST films, the same IBAD-MgO Hastelloy tapes were used, as well as Ni-5at.%W RABiTS templates with a $\text{La}_2\text{Zr}_2\text{O}_7/\text{CeO}_2$ buffer architecture (provided by Deutsche Nanoschicht GmbH) and Ni-9at.%W RABiTS templates with a single Y_2O_3 buffer layer. The Y_2O_3 layer was grown with a thickness of 50 nm via PLD in an Ar/ H_2 atmosphere at a pressure of 3×10^{-2} mbar. A few films were also prepared on single crystalline substrates such as MgO and CaF_2 . The superconducting films were grown by PLD using a KrF excimer laser ($\lambda = 248$ nm) in an ultra-high vacuum (UHV) chamber with a base pressure below 10^{-8} mbar. The laser repetition rate was 7 Hz and the temperature was set to 360 °C. The film thickness was again controlled by the pulse number. After the deposition, the films were cooled to room temperature in UHV.

The Tl-1223 films were prepared on textured Ag ribbons [72] and SrTiO_3 (STO) single crystalline substrates by electrochemical deposition in a three-electrode system in a flat cell. The STO substrate was metallized via sputtering before the deposition process. The respective substrate, a platinum grid and Ag/ AgNO_3 in Dimethyl Sulfoxide (DMSO) were used as working, counter and reference electrode, respectively. The film deposition was performed around -3 V for 600 s with a commercial potentiostat. The samples were then dried in vacuum at 120 °C and annealed at 885 °C for 10 minutes in a three-zone tube furnace using a gold foil crucible. Since thallium oxide is volatile above 710 °C, the sample had to be kept in a thallium atmosphere which was realized by using Tl_2O_3 powder and Tl-1223 pellets. More details on the production process can be found in [40].

2.2 Magnetic Characterization

The global critical current density, critical temperature and local critical current density distributions of thin films were determined magnetically. For the experiments a commercial SQUID magnetometer was used as well as scanning Hall probe microscopy setups that were built in-house. The following section describes the experiments that were conducted along with necessary sample preparations and gives an overview of the experimental setups as well as details on the evaluation of the obtained results.

2.2.1 SQUID Magnetometer

The critical temperature, T_c , and the global critical current density, J_c^G , of thin films were determined by means of magnetization measurements using a superconducting quantum interference device (SQUID) magnetometer (MPMS, Quantum Design). This is a complex measurement device which uses flux quantization in a superconducting ring and the Josephson effect to precisely determine the magnetic moment of a sample. A detailed description of the functional principle and applications of SQUID magnetometers can be found in [73]. A common method to determine T_c are AC susceptibility measurements, where the Meissner state of a superconducting sample is probed by applying a small AC magnetic field (typically 30 μT) and measuring the response of the sample. Above T_c superconductors usually have a small susceptibility χ , while in the superconducting state the sample is a perfect diamagnet with $\chi = -1$. In AC measurements the susceptibility is divided into an in-phase (χ') and out-of-phase (χ'') component, as can be seen in Figure 2.2.1. The former follows the same curve as the measured magnetic moment m , while the latter is a measure for energy dissipation in the superconductor during the transition from the normal conducting into the superconducting state which is shown in the form of a peak. The AC susceptibility measurements in this thesis were performed by inserting the sample and then cooling down to 5 K in zero-field in order to center the sample in the SQUID magnetometer. Then the temperature was set above T_c to avoid any contribution to the signal from a trapped field inside the sample. The magnetic moment was then measured while ramping down the temperature (usually to 5 K or 2 K). T_c in this thesis is defined as T_c^{onset} , which is the temperature that exhibits the first significant non-zero susceptibility.

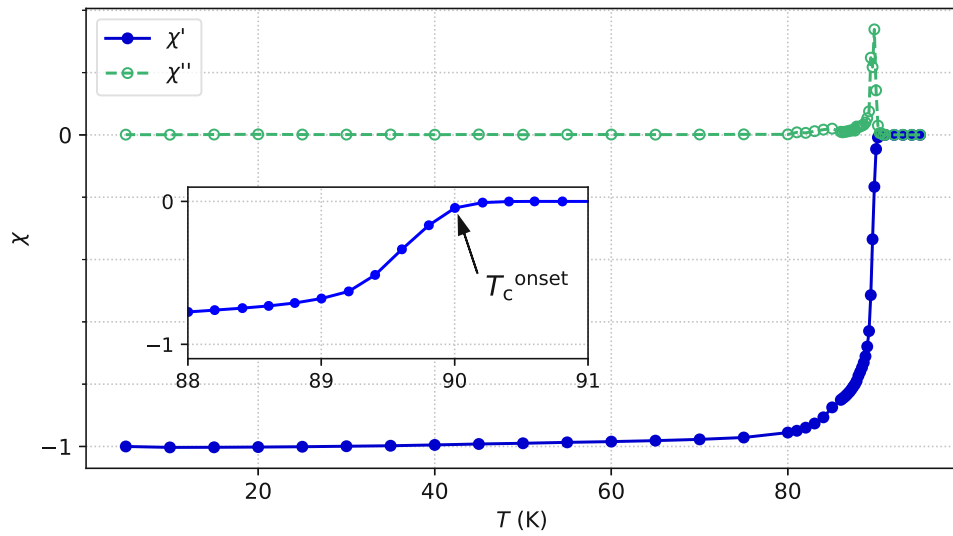


Figure 2.2.1: AC susceptibility measurement of a superconducting thin film. The in-phase component χ' follows the curve of the measured magnetic moment m . The out-of-phase component χ'' is a measure for energy dissipation and can be observed in the form of a peak. The inset illustrates the definition of T_c^{onset} .

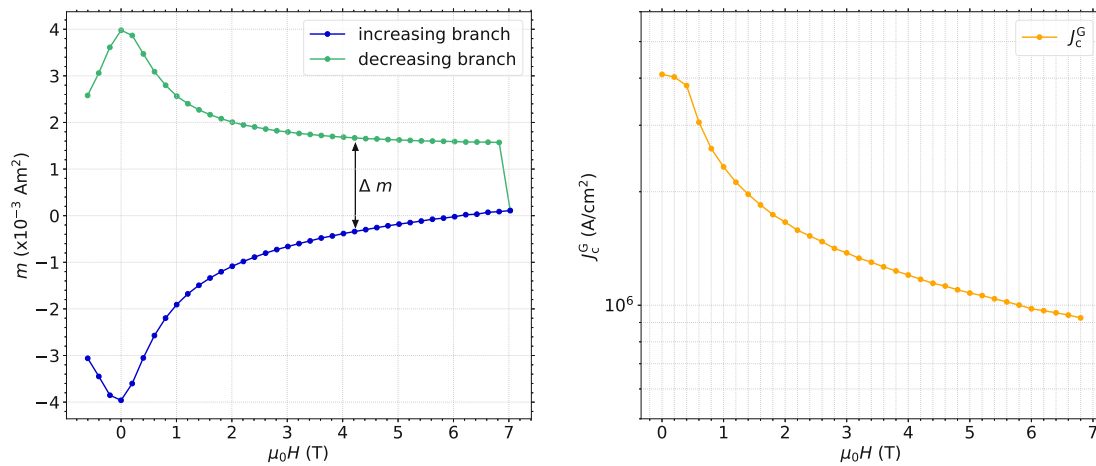


Figure 2.2.2: Typical magnetization hysteresis loop (left panel) and calculated global critical current density (right panel).

The global critical current density J_c^G can be determined magnetically through so-called magnetization hysteresis loops where the magnetic moment of a sample is measured at increasing and decreasing applied magnetic fields. The evaluation of J_c^G is based on Bean's critical state model [67], and the definition of the magnetic moment

$$\vec{m} = \frac{1}{2} \int \vec{r} \times \vec{J} d^3r, \quad (2.2.1)$$

which results from a current density \vec{J} . The global critical current density of a cuboid sample with dimensions a, b, c and $a \geq b$ can be calculated with

$$J_c^G = \frac{4 |m_{\text{irr}}|}{a b^2 c (1 - b/3a)}, \quad (2.2.2)$$

where $m_{\text{irr}} = \Delta m/2$ is the irreversible magnetic moment and Δm is the difference of the magnetic moment in the decreasing and increasing field branch, see Figure 2.2.2. For the measurement of the hysteresis loop, the sample is fully magnetized with a negative magnetic field applied parallel to its c -axis (typically -3 T) and the magnetic moment is then measured from a certain small negative applied field to 7 T (increasing branch) and back (decreasing branch). The calculated J_c^G is typically visualized using a logarithmic scale on the y -axis.

2.2.2 Wide Area Hall Scanner

The wide area Hall scanner at the Atominstitut is the standard instrument for pre-characterization of high temperature superconducting (HTS) samples. The scanner, sketched in Figure 2.2.3, operates in a liquid nitrogen bath. A vertical rod is moved in the x -, y - and z -direction by three stepper motors which are positioned outside the liquid nitrogen bath. The smallest possible step size is $10 \mu\text{m}$ in all three directions. The Hall probe (HHP-VC, Arepoc), which is mounted at the end of a bendable carbon fiber cantilever, has an active area of $50 \times 50 \mu\text{m}^2$. It is mounted with an angle of about 3° with respect to the surface horizontal in order to assure that the active area is the closest point to the sample surface. Two strain gauges on the cantilever, arranged as part of a Wheatstone bridge, are used to test the contact at the sample surface. The scanner has a scan range of about $30 \times 10 \text{ cm}^2$ and a spatial resolution of $50 \mu\text{m}$.

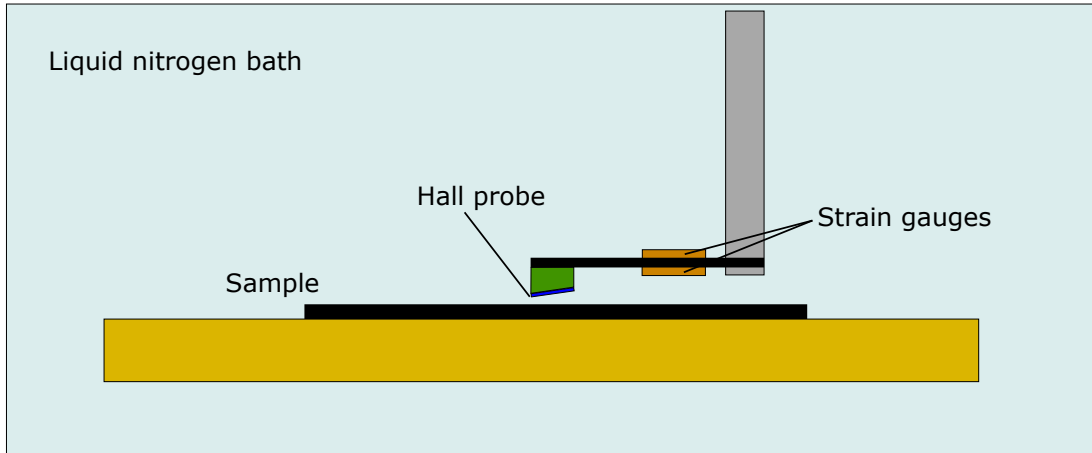


Figure 2.2.3: Sketch of the wide area Hall scanner setup inside the liquid nitrogen bath.

With this setup remnant field profiles of HTS samples are mapped in the x - and y -direction at 77 K. In order to understand how a remnant field profile is developed inside a superconductor, Bean's critical state model [67] has to be considered again. The model states that the only possible current density inside a superconductor is the critical current density which is assumed to be constant and field independent inside the whole sample. Figure 2.2.4 illustrates the magnetization process of an infinitely long sample with radius r . An increasing external magnetic field results in a flux density gradient inside the sample which represents the critical current density in this area. At an external field H^* the magnetic flux reaches the center of the sample, i.e. the critical current flows inside the whole sample. A further increase of the external magnetic field merely shifts the field profile inside the sample to higher values while the critical current density stays constant. A decrease of the external field leads to a flux density gradient in the opposite direction, as can be seen in the right panel of Figure 2.2.4. The magnetization profile begins to reverse at the edges, while it still stays the same in the center. Once the external field is decreased to zero, a remnant field profile remains inside the sample with a maximum height of H^* . In order to achieve a fully reversed field profile a superconductor has to be magnetized with an external magnetic field of at least $2H^*$.

For the measurement process with the wide area Hall scanner, a sample is immersed in liquid nitrogen and a permanent magnet is dragged above the sample surface to achieve the magnetization described above. Contact at the sample surface is tested in the center and on

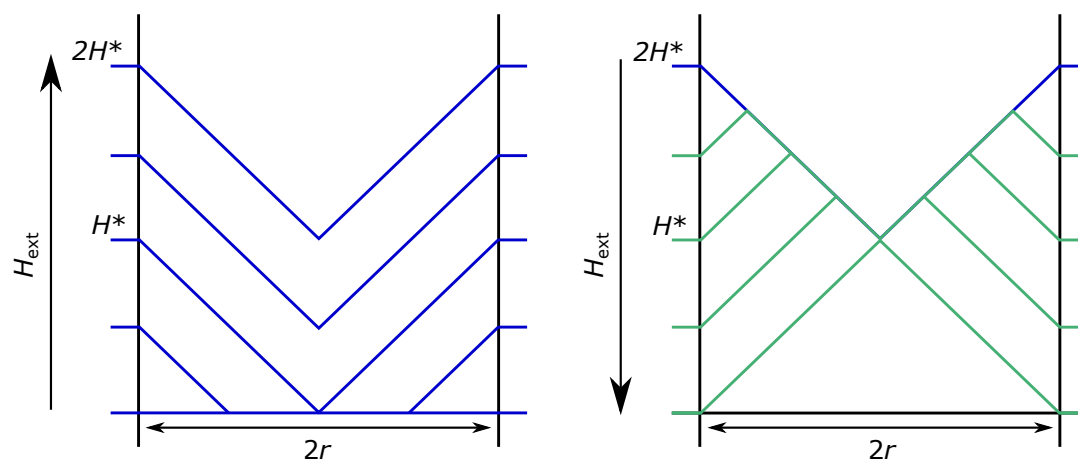


Figure 2.2.4: Bean's critical state model. Magnetization inside the sample at increasing (left panel) and decreasing (right panel) external magnetic field.

all four edges of the sample and the distance of the Hall probe to the sample surface is set to approximately $30\ \mu\text{m}$. The remnant field profile of the superconductor is then mapped with a certain step size in the x - and y -direction. In the case of thin film superconductors the obtained field profile differs from the theoretical profile, as can be seen in the left panel of Figure 2.2.5. Due to the demagnetization in thin samples, the self-field of the superconductor is reversed near the sample edges. This so-called return field increases with thinner samples, at the same time the self-field peak in the center of the sample becomes sharper. The right panel of Figure 2.2.5 shows a typical measured remnant field profile of a thin film superconductor at $77\ \text{K}$.

In order to prepare samples for high-resolution Hall mapping in the micro Hall scanner, round spots with a diameter of $500\ \mu\text{m}$ - $1000\ \mu\text{m}$ where either chemically etched or prepared by a laser cutter, which uses the same setup as the wide area Hall scanner. Instead of the cantilever and Hall probe, a rod carrying a laser diode with a wave length of $405\ \text{nm}$ (SLD-405-150, CNI) is moved by the stepper motors, see Figure 2.2.6 left panel. The laser beam is focused on the sample surface and moved in a certain pattern over the superconductor. Areas that are hit by the focused laser beam are destroyed. Typically a round spot and a satellite spot, that can be used to find the right orientation of the sample, are omitted by the laser, as can be seen in the right panel of Figure 2.2.6. Figure 2.2.7 shows that any shape can be constructed by the laser cutter and magnetically detected by the Hall scanner.

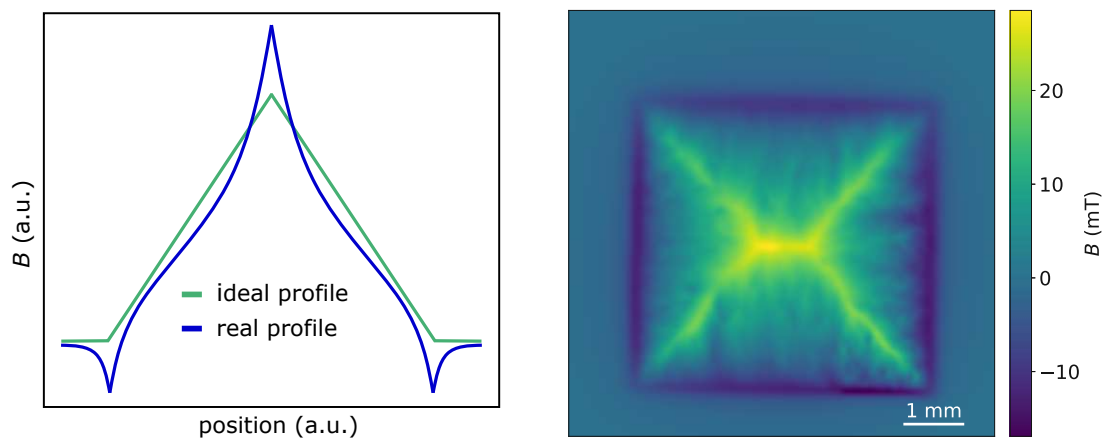


Figure 2.2.5: Comparison of ideal and real field profile (left panel) and typical measurement of a remnant field profile at 77 K (right panel).

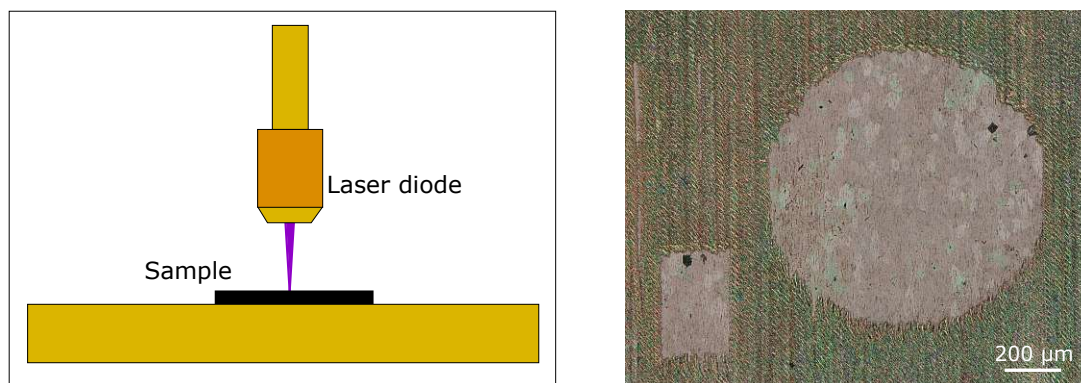


Figure 2.2.6: Sketch of the laser cutter set up (left panel) and example of a lasered sample (right panel). A round spot and a satellite spot for sample orientation are omitted by the laser.

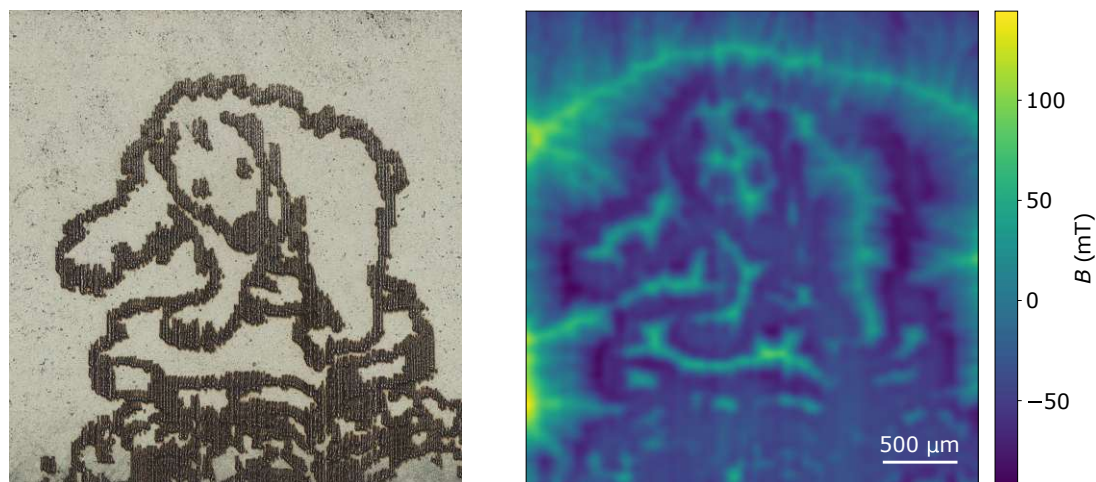


Figure 2.2.7: The group logo of the Superconductivity and Low Temperature physics group, a polar bear, lasered onto the surface of a superconductor (left panel). The polar bear can clearly be detected in the remnant field of the superconductor (right panel).

2.2.3 Micro Hall Scanner

The micro Hall scanner is built as an insert in an 8 T cryostat, which enables self-field as well as in-field measurements at temperatures from 4 K – 300 K. A sketch of the setup is shown in the left panel of Figure 2.2.8. Piezo-based low temperature nanopositioners with resistive encoders (ANPz51/RES/LT and ANPx51/RES/LT, attocube) are used to move a sample stage (z -direction) and a cantilever (x - and y -direction) with a precision of 1 μm . A Hall probe with an active area of $400 \times 400 \text{ nm}^2$ (CSHP-400, MAGCAM) is mounted at the end of a carbon fiber cantilever with an angle of 3° with respect to the surface horizontal and contact at the sample surface is monitored by two strain gauges, arranged as part of a Wheatstone bridge. The distance of the active area of the Hall probe to the sample surface can be as little as 1 μm , depending on the flatness of the sample. A laser microscope image of the active area of the Hall probe, which is positioned at the tip of the cantilever, can be seen in the right panel of Figure 2.2.8. The negative voltage output of the Hall probe is electrically connected to the sample stage and thus the sample itself, in order to avoid artifacts of a potential difference in the measured Hall voltage. The micro Hall scanner has a scan range of $3 \times 3 \text{ mm}^2$ and a spatial resolution of 1 μm .

For the measurement process, a sample is mounted on the sample stage with vacuum grease

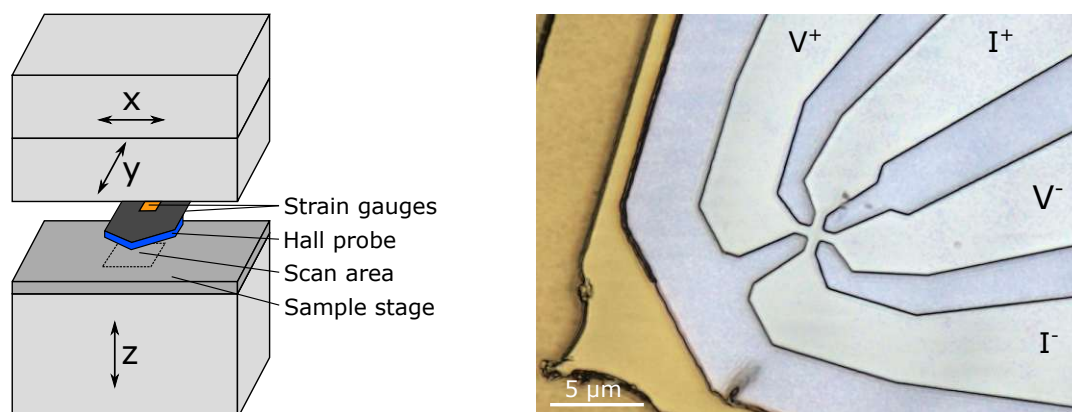


Figure 2.2.8: Sketch of the micro Hall scanner (left panel) and laser microscope image of the tip of the Hall probe (right panel).

and the surface roughness and sample tilt is checked with a digital light microscope (VHX-6000, Keyence), as can be seen in Figure 2.2.9. If the tilt is below $10\ \mu\text{m}$, the sample is electrically connected to the sample stage with conductive silver, the tip of the Hall probe is positioned at the center of the sample and contact at the sample surface is tested at room temperature. The setup is then inserted into the cryostat and cooled to a certain temperature in zero field.

Once the desired temperature is reached, a small magnetic field is applied, and the superconducting spot is centered with line scans in the x - and y -direction by its Meissner signal. Contact to the sample surface is tested at the center and the four edges of the sample. Next, the Hall probe is moved away from the superconductor, the sample is magnetized by applying an external field that is greater than $2H^*$ and the Hall voltage, U_H , is recorded as a function of the applied field in order to determine the Hall constant $A_H = H/U_H$. Since the Hall probe is quite fragile and the Hall constant easily changes when the tip goes into contact with the sample surface, this calibration needs to be done before each measurement. After the external field is removed, the temperature is set to a smaller value in order to freeze the remnant field profile of the superconductor. This so-called undercooling method reduces relaxation and guarantees a stable field profile. The distance between the tip of the Hall probe and the sample is set as small as possible (usually $3 - 5\ \mu\text{m}$) and the measurement is started.

Figure 2.2.10 shows two typical field profiles of a granular superconductor at 5 K. First, a big scan area with a coarse step size is chosen, in order to see the lasered spot and satellite (left

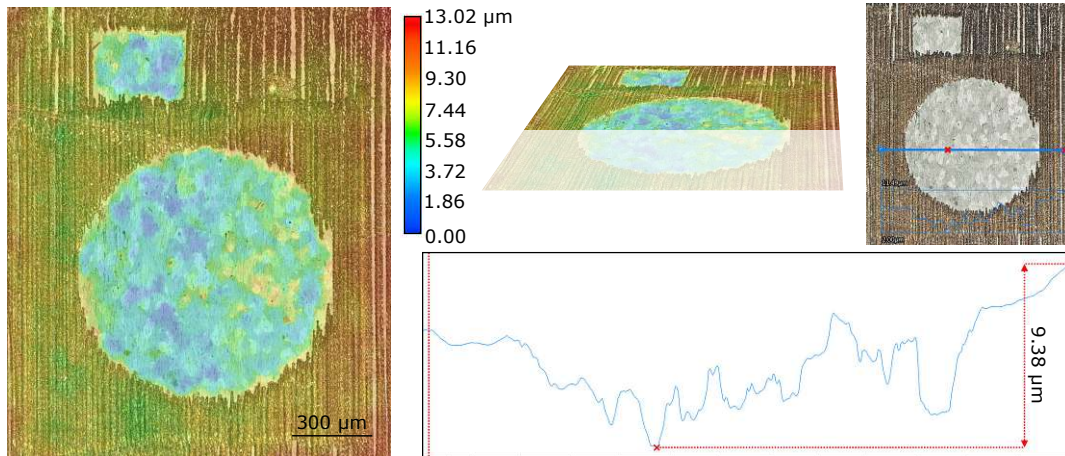


Figure 2.2.9: Preparation with a digital light microscope. The sample tilt and surface roughness is checked before each measurement with the micro Hall scanner.

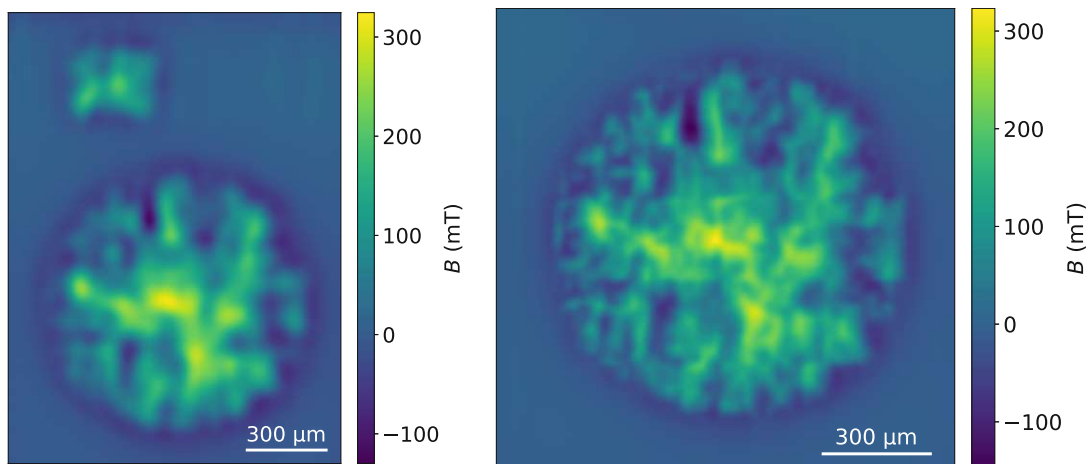


Figure 2.2.10: Typical measurement of a remnant field profile at 5 K. First the entire area with satellite spot is scanned with a larger step size of 21 μm (left panel), afterwards only the spot of interest is scanned with a small step size of 7 μm (right panel).

panel). With this, the right orientation of the sample can be easily found, when comparing the remnant field profile to the microstructure. Afterwards a higher resolution scan with a smaller step size is conducted for further analysis (right panel). In the higher resolution scan features become much sharper, showing that the micro Hall scanner is an excellent tool for investigations of granularity.

2.2.4 Local Current Density Distribution

The local critical current density J_c^L was calculated by an inversion of Biot Savart's law using the local B -field obtained from Hall measurements [68]. The algorithm uses a sample with its surface in the xy -plane, where the z -component of the B -field is measured. The scan area is divided into cubic volume elements with a constant magnetization \vec{M} , as can be seen in Figure 2.2.11. The measured B -field is expressed as a function of M

$$B(\vec{r}) = \mu_0 M(\vec{r}) + \frac{\mu_0}{4\pi} \int \int dx' dy' \frac{M(x', y')(z - z')}{[(x - x')^2 + (y - y')^2 + (z - z')^2]^{3/2}} \Big|_{d+c}^d, \quad (2.2.3)$$

where d is the distance of the active area of the Hall probe to the sample surface and c is the thickness of the superconducting layer. In the case of an infinitely thick sample ($z - z' \rightarrow \infty$), the second term in Equation 2.2.3 vanishes and $\vec{B} = \mu_0 \vec{M}$ inside the sample and $\vec{B} = 0$ ($\vec{M} = 0$) elsewhere. For finite geometries the integral must be solved in order to obtain \vec{M} . Summing over all cubic elements leads to the matrix equation

$$B_{i,j} = \sum_{k=1}^{n_x} \sum_{l=1}^{n_y} K_{i,j,k,l} M_{k,l}. \quad (2.2.4)$$

The components $M_{k,l}$ are obtained by inversion of Equation 2.2.4, and the critical current density is expressed as the curl of the obtained magnetization

$$\vec{J} = \vec{\nabla} \times \vec{M}. \quad (2.2.5)$$

The inversion algorithm was found to work well for thin superconducting samples, where the critical current is assumed to flow in the xy -plane, if the distance d and the step sizes Δx , Δy

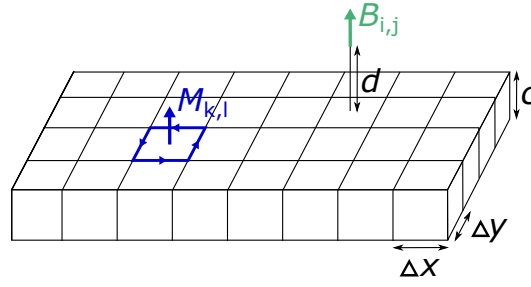


Figure 2.2.11: Coordinate system of the inversion algorithm.

satisfy the condition

$$\Delta x, \Delta y \geq d + c. \quad (2.2.6)$$

Therefore, for all measurements the step size and distance of the Hall probe were chosen to satisfy this condition.

The inversion algorithm calculates the absolute values of the local critical current density $J_c^L = \sqrt{J_x^2 + J_y^2}$ as well as the current densities J_x in the x -direction and J_y in the y -direction. This can be visualized in an image plot, where the colors represent the absolute values J_c^L , while J_x and J_y are represented by arrows showing the direction of current flow, as can be seen in Figure 2.2.12. The left panel shows a typical J_c^L distribution at 77 K, where the trapped field profile was obtained in the wide area Hall scanner with a spatial resolution of 50 μm (cf. Figure 2.2.5 right panel). Closed loops of currents flow around the superconducting area and the magnitude of J_c^L is homogeneously distributed. Two types of discontinuity lines can be observed due to the rectangular shape of the sample, namely a horizontal zero- J_c^L line in the center and two diagonal lines. The former corresponds to currents flowing in opposite directions while the latter appear where the currents change direction. These types of blind spots caused by geometric constraints are mostly avoided when mapping a circular sample. Therefore, round spots were prepared for investigations with the micro Hall scanner. The right panel in Figure 2.2.12 shows a typical J_c^L distribution of a granular superconductor at 5 K, where the trapped field profile was obtained with a spatial resolution of 7 μm (cf. Figure 2.2.10 right panel). The granular nature of the sample is represented by meandering currents that lead to some areas with high J_c^L and other areas with low J_c^L .

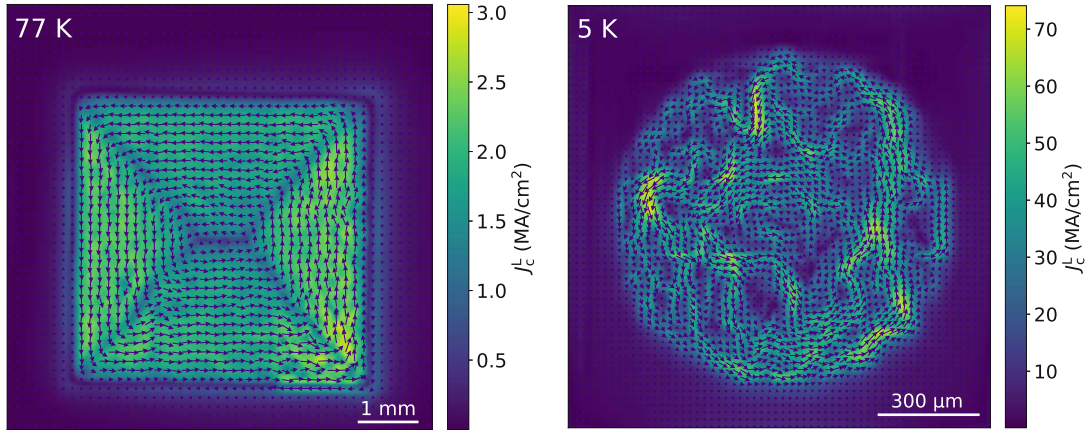


Figure 2.2.12: Typical local current density maps. The J_c^L map at 77 K has a spatial resolution of 50 μm (left panel), while the J_c^L map at 5 K was obtained with a spatial resolution of 7 μm (right panel).

In order to assess the granularity of various thin films from Hall measurements in a quantitative manner, a statistical analysis was employed, such that only J_c^L values that are within the sample borders are taken into account. Various geometrical forms such as rectangles, circles and ellipses are used to choose an area in the current density map that contains as many J_c^L values as possible. At the same time, the area is chosen with some distance to the borders in order to omit current density values that are affected by geometric imperfections at the edges, see Figure 2.2.13. A matrix of zeros is generated with the same dimension as the J_c^L -matrix and ones are written within the chosen area. The new matrix is multiplied element-wise with the original J_c^L -matrix and zeros are converted to NaNs in order to obtain a matrix that just contains the J_c^L values of interest. The same procedure is done for the J_x - and J_y -matrices to obtain the J_x and J_y values of interest.

These values can now be visualized in a histogram plot, see Figure 2.2.14. The critical current density values are displayed at the x -axis and the height of the bars indicate how often respective J_c^L values occur. In order to compare the histograms of different samples of various sizes, the heights are normalized by the total number of points, which gives the probability density. While the height, width and shape of the J_c^L distribution gives information about the average critical current density and the granularity, the histogram plots of the J_x and J_y values show how much current flows in the positive and negative x - and y -direction. The average local critical current

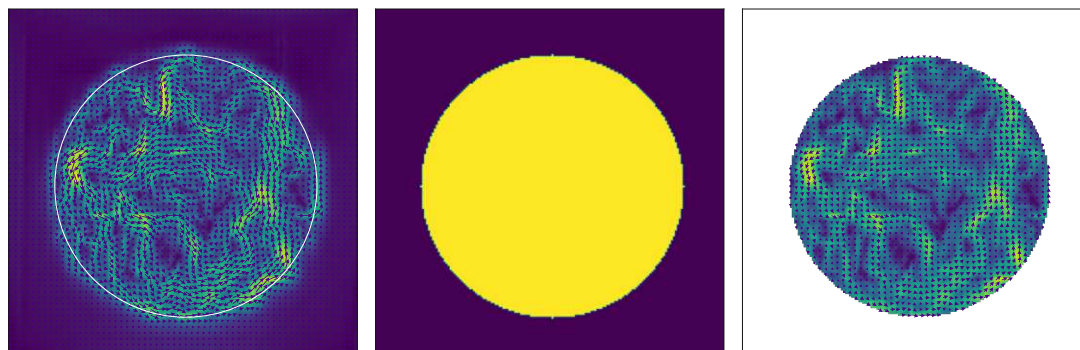


Figure 2.2.13: Area selection of J_c^L -matrix for statistical analysis. An area within the sample borders is chosen with a geometrical form (left panel). A matrix of zeros is generated and ones are written within the chosen area (middle panel). The new matrix is multiplied element-wise with the original J_c^L -matrix and zeros are converted to NaNs in order to obtain a matrix that just contains the J_c^L values of interest (right panel).

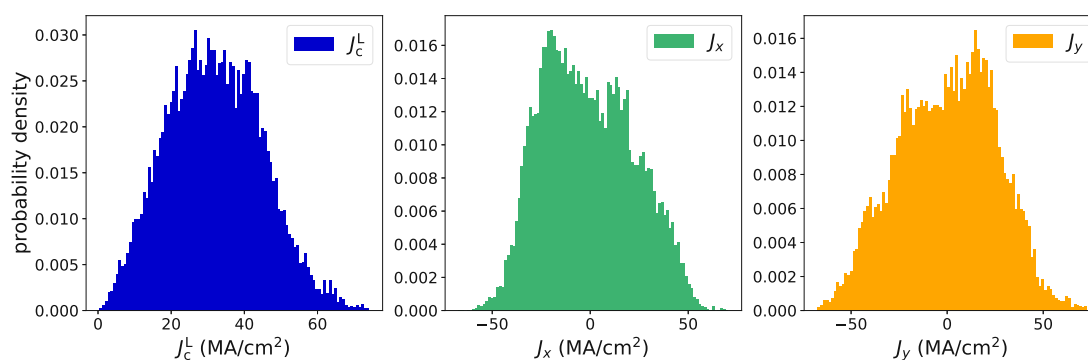


Figure 2.2.14: Histogram plots of the absolute values of the local critical current density (left panel), the current density in x -direction (middle panel) and the current density in y -direction (right panel).

density of various samples can be compared by calculating the mean J_c^L value, $\mu = \frac{1}{N} \sum_{i=1}^N J_c^L i$, of each sample, with N being the total number of J_c^L values. The magnetic granularity in this thesis is represented by the relative standard deviation

$$\sigma_n = \frac{\sigma}{\mu}, \quad (2.2.7)$$

which is defined as the ratio of the standard deviation σ and its respective mean value μ .

2.3 Microstructural Characterization

The microstructural characterization of superconducting samples was conducted at the electron microscopy facility USTEM, TU Wien. The following sections give a brief overview of the scanning electron microscope for surface investigations, the focused ion beam for sample preparation, the transmission electron microscope for in-depth characterization as well as analytical electron microscopy for investigations on the chemical composition and grain orientation of superconductors.

2.3.1 Scanning Electron Microscopy

A scanning electron microscope (SEM) is a very useful instrument with various detection techniques that enable investigations of the surface quality, chemical composition and grain alignment. All SEM experiments for this thesis were conducted using a FEI Quanta 250 FEGSEM with an acceleration voltage of 30 kV. For the experiments, a sample is mounted on a sample stage with either carbon tape or conductive silver in order to assure electrical contact and avoid charging effects. The primary electron beam hits the sample surface and depending on the acceleration voltage of the primary beam and the chemical composition of the sample, an interaction volume of a few micrometers is formed inside the sample, see Figure 2.3.1.

Two different imaging techniques were employed, using either secondary electrons (SE) or backscattered electrons (BSE). The detection of SE gives information about the surface topography, since these are low energy electrons coming from inelastic interactions of the primary beam and sample atoms within the first few nanometers. The SE detector is an Everhart-Thornley de-

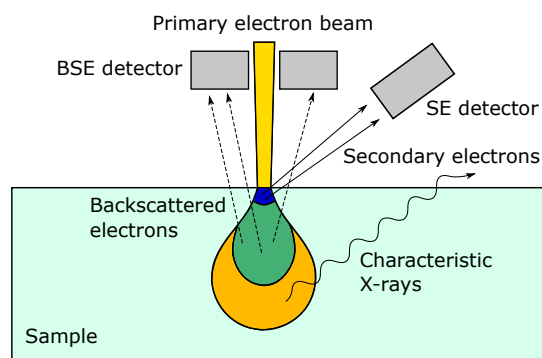


Figure 2.3.1: Interaction volume in a scanning electron microscope. Secondary electrons are emitted from the first few nanometers below the sample surface, while backscattered electrons and characteristic X-rays come from a depth of 1 μm or more.

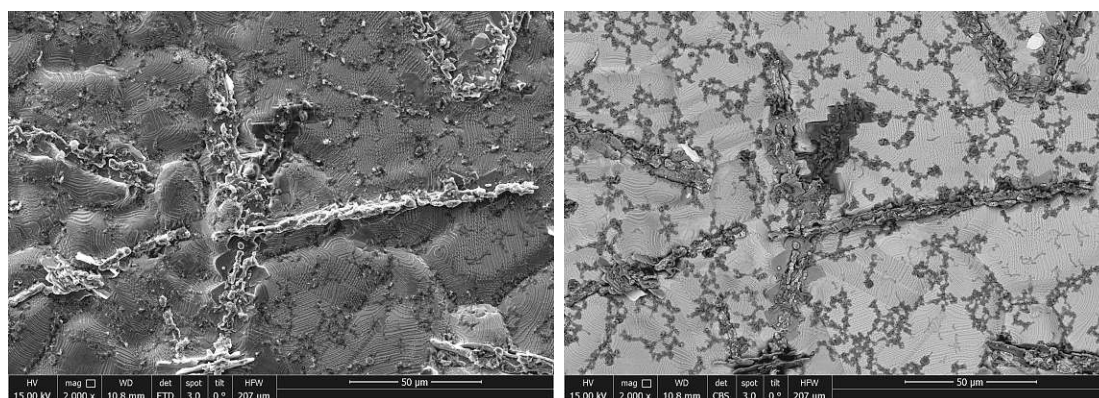


Figure 2.3.2: Comparison between secondary electron image (left panel) and backscattered electron image (right panel). The surface topography can be identified in the SE image, while the gray scale contrast in the BSE image gives information about the chemical composition.

tector, which is a type of collector-scintillator-photomultiplier system. The detector is positioned at an angle with respect to the sample surface to optimize the detection of SE. Therefore, structures and edges that are facing the detector appear brighter in the image. The detection of BSE gives information on the chemical composition of the sample. Electrons from the primary beam are reflected or elastically scattered from the interaction volume inside the sample. The primary electrons are backscattered stronger at heavy elements with high atomic numbers compared to light elements. Therefore, areas containing heavy elements appear brighter in the BSE image, which gives a first idea on the chemical composition of the sample. A comparison of the two imaging techniques on the same sample area can be found in Figure 2.3.2. For investigations on the actual chemical composition of a sample, the detection of characteristic X-rays is a common method, which will be described in Chapter 2.3.4.

2.3.2 Focused Ion Beam

In order to prepare samples for transmission electron microscopy (TEM) investigations, thin TEM lamellae were produced using a focused ion beam (FIB). In the course of the experiments for this thesis, first a FEI Quanta 200 3D DualBeam FIB was used, and later a new ThermoFisher Scios 2 system. Both systems feature a vertical electron column and a gallium ion column at an angle of 52° with respect to the vertical. Both the electron and ion beam can be used for imaging, but it has to be considered that using the ion beam leads to damages on the sample surface. Depending on the tilt of the sample stage, either the electron beam (0° tilt) or the ion beam (52° tilt) is perpendicular to the sample surface. The preparation of a TEM lamella follows the same steps in both systems and is illustrated in Figure 2.3.3(a–f).

First, an appropriate area is chosen in the electron image (e.g. across a grain boundary). A protective layer of carbon or tungsten (depending on the FIB system) is deposited on the sample surface in a rectangular area of $20\ \mu\text{m} \times 2\ \mu\text{m}$ by using the electron beam (a). This area is located in the ion image and a thick protective layer of tungsten or platinum is deposited on top of the first layer by using the ion beam (b). Next, the ion beam is used to cut into the sample on three sides of the protective layer. In order to cut out a wedge-shaped lamella, the sample stage is tilted by a few degrees with respect to the ion beam axis, i.e. $52^\circ \pm 5^\circ$ (c). The lamella is

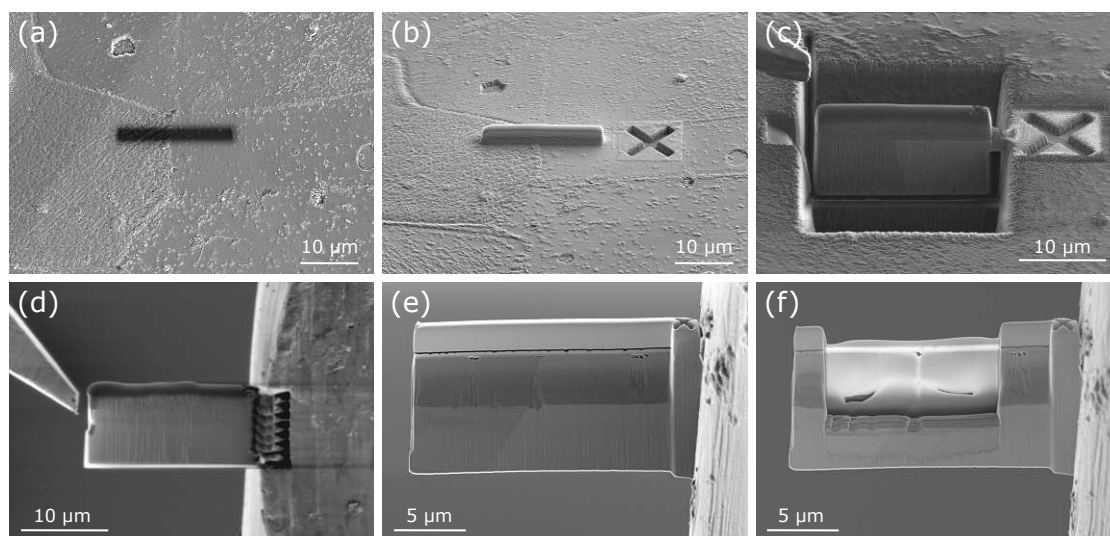


Figure 2.3.3: Preparation of a TEM lamella using a focused ion beam.

attached to a needle by means of tungsten deposition, cut free from the sample surface and lifted out of its original place. Now the lamella can be attached to a TEM grid (d). The standard grid is made of copper, which was used for iron-based superconductors. For the cuprates however, a molybdenum grid was used, in order to avoid an additional copper signal from the grid when identifying the chemical composition of the superconductor. Once the lamella is attached to the grid, the thinning process can begin (e). The ion beam is used to cut material from both sides of the lamella while tilting the sample stage again by a few degrees to maintain the wedge shape. A window is cut into the lamella for better stability and the ion beam current is reduced several times, until the window is as thin as 100 nm or less (f). During the thinning process, particular attention has to be paid to the thickness decrease of the protective layer. At least a thin layer has to stay on top of the lamella, otherwise the sample surface will be damaged. If the window in the lamella appears bright in the electron image and holes start to appear in the substrate, the lamella is thin enough and ready for TEM investigations.

2.3.3 Transmission Electron Microscopy

A full description of the theory and all functionalities of a transmission electron microscope (TEM) would be out of scope of this thesis, hence literature should be consulted for a more

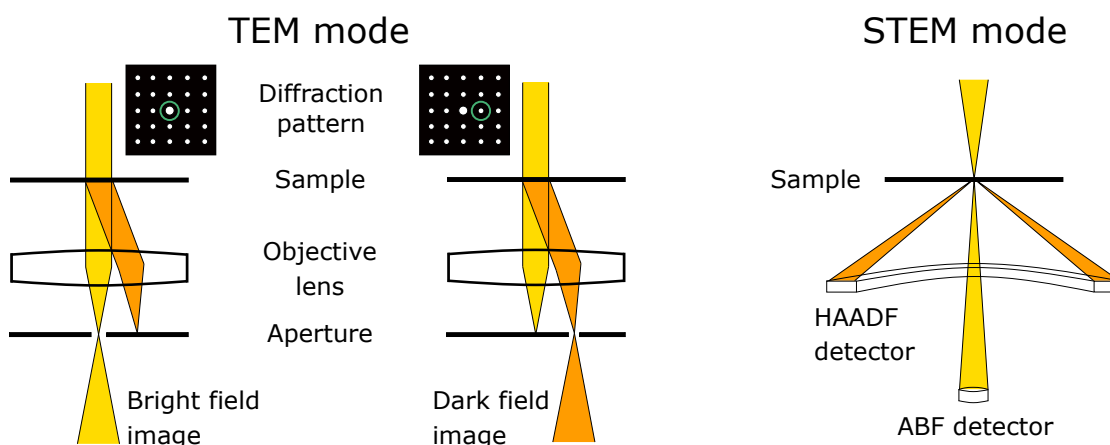


Figure 2.3.4: Operation modes of a transmission electron microscope.

comprehensive description [74]. Instead, a small overview of the measurement methods that were used will be given. All TEM experiments were conducted using a FEI TECNAI F20 with an acceleration voltage of 200 kV. For the investigations the sample has to be electron transparent with a thickness of 100 nm or less. The microscope can be operated in two different modes, namely TEM mode and STEM (scanning TEM) mode. A very simplified sketch of the two operation modes is presented in Figure 2.3.4.

In TEM mode, the current through the beam steering electromagnetic lenses is chosen in such a way that the beam is nearly parallel when passing through the sample. The most common imaging technique in TEM mode makes use of bright field (BF) images, where the transmitted electrons are selected by an aperture and scattered electrons are blocked. Crystalline areas and areas with heavy elements appear dark, while amorphous areas and vacuum appear bright in the image. A useful technique for the investigation of granular samples is the acquisition of dark field (DF) images. Here, electrons that are scattered in the sample are selected by an aperture, while the transmitted beam is blocked. Depending on the position of the aperture, different areas appear bright in the DF image which is useful for the visualization of grain boundaries. Figure 2.3.5 shows an example of a BF image (left panel) and a DF image (right panel) of the same sample area.

In TEM mode, diffraction patterns can be obtained if the electromagnetic lenses are excited in such a way that initially parallel beams intersect in the back focal plane of the objective

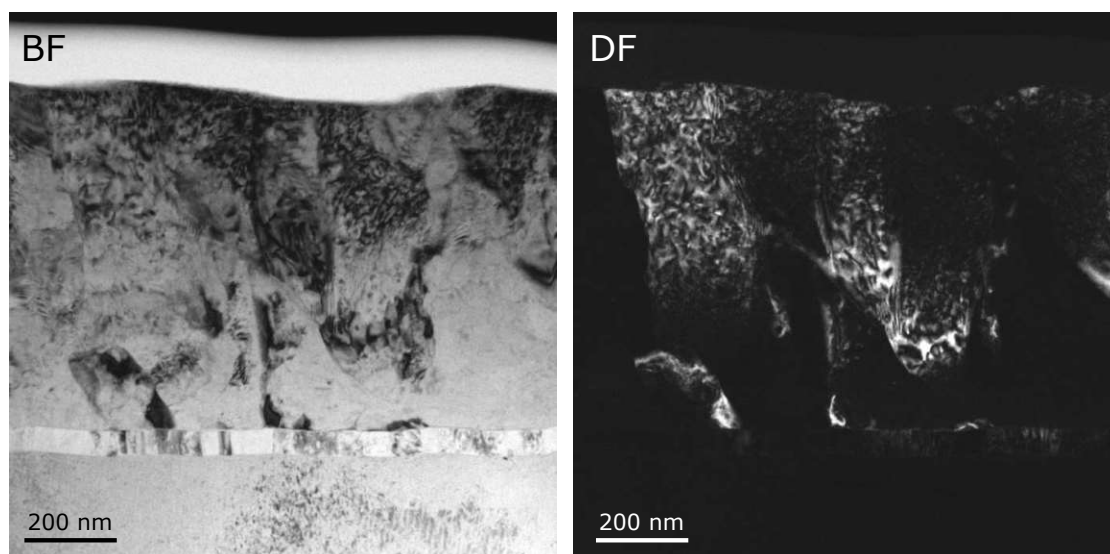


Figure 2.3.5: Bright field image (left panel) and dark field image (right panel) of the same sample area.

lens. An appropriate aperture is chosen in order to obtain the diffraction pattern of a specific area, see Figure 2.3.6. The diffraction pattern can be seen as a projection of the reciprocal crystal lattice, therefore much information can be obtained by analyzing its appearance. A regular point-like pattern indicates a crystalline area, while circles in the diffraction pattern point to a polycrystalline or amorphous area. If the sample is tilted in a specific direction, vertical lines of points can be observed (Figure 2.3.6 middle panel) which correspond to the ab -planes of the superconductor, as can be seen in the high-resolution image (right panel). This method can be used to identify the out-of-plane orientation of different grains in the substrate and superconducting layer. A diffraction pattern of a grain boundary region can also be used to identify diffraction points stemming from different grains, in order to place the aperture accordingly and obtain the respective DF images for visualization of the grain boundary.

In STEM mode, the current through the electromagnetic lenses is chosen in such a way, that the beam is focused into a narrow spot and each sample point is scanned, see Figure 2.3.4 right panel. For imaging, either the annular bright field (ABF) detector or the high-angle annular dark field (HAADF) detector is used. A comparison of the two imaging techniques can be seen in Figure 2.3.7. Similar to bright field imaging in TEM, the ABF detector collects the transmitted electrons. Although the resolution is not as good as with TEM bright field imaging, obtaining

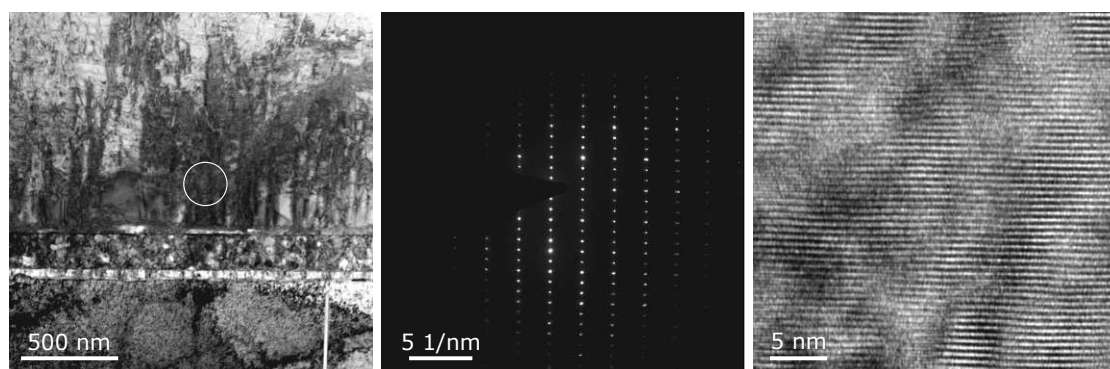


Figure 2.3.6: Diffraction pattern and high-resolution imaging in TEM mode. The white circle (left panel) indicates the aperture that was chosen, to obtain the regular point-like diffraction pattern (middle panel). The vertical lines of points correspond to the ab - planes, visualized in the high-resolution image (right panel).

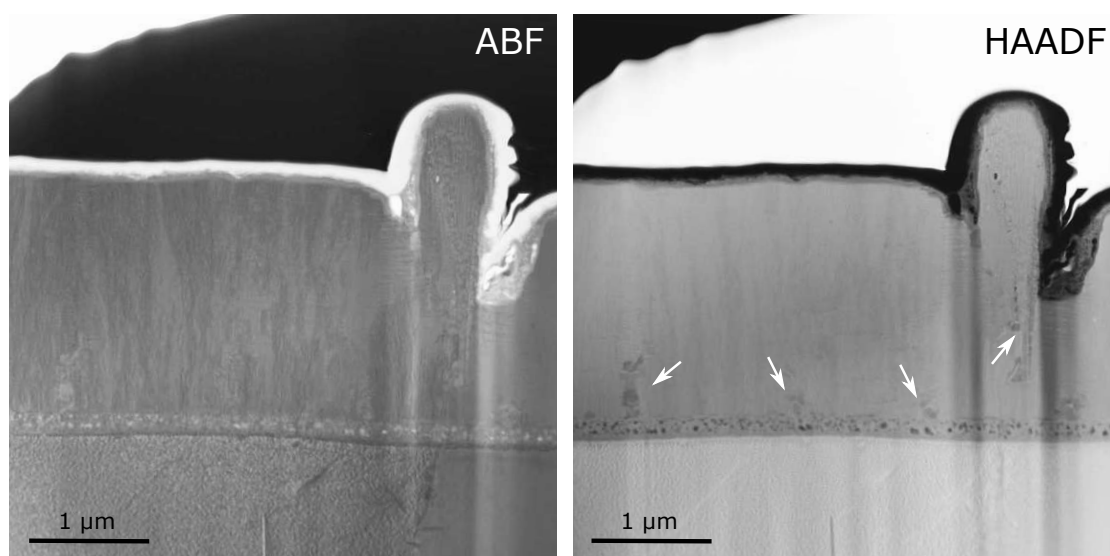


Figure 2.3.7: Annular bright field (left panel) and high-angle annular dark field imaging (right panel) in STEM mode. The contrast in the HAADF image gives information on the chemical composition of the sample, therefore secondary phases in the superconductor can be easily detected as indicated by the arrows.

STEM ABF images can be useful, as they can be directly compared to HAADF images. The HAADF detector collects electrons that are scattered to high angles only. The contrast in the image arises due to Rutherford scattering, which depends strongly on the atomic number Z of elements. This so-called Z -contrast gives qualitative information on the chemical composition of a sample, therefore secondary phases in the superconducting layer can be easily identified. For a quantitative analysis of the chemical composition, the detection of characteristic X-rays can be used in STEM mode, as described in the next section.

2.3.4 Analytical Electron Microscopy

The chemical composition of samples was determined by energy-dispersive X-ray spectroscopy (EDX) using either SEM or STEM. The method is based on the detection of characteristic X-rays and the principle is the same for both instruments. The emission of a characteristic X-ray occurs, when an inner shell electron from an atom in the sample is knocked out by an electron from the primary beam. An electron from an outer shell fills the vacancy and the energy difference between the two shells is released in the form of an X-ray. The energy difference between shells is characteristic for each element, therefore the detection of these X-rays can be used to determine which elements are present in the sample. The EDX spectrum exhibits peaks corresponding to the characteristic X-rays emitted by the atoms of the different elements present in the sample, as can be seen in Figure 2.3.8. By comparing the relative amount of each element in atomic percent, the superconducting phase can be determined.

Among various acquisition options the EDX spectrum can be collected at a certain point (point analysis), along multiple points in a line (line scan) and at every point in a rectangular area (elemental mapping). The last option was used to collect phase maps for each element in order to find areas that are rich with one element but lack another. That way, the presence of secondary phases in the superconducting layer can be visualized, see Figure 2.3.9. The spatial resolution of the obtained maps depends on the beam diameter and the chosen step width. It should be mentioned that the quantification of EDX spectra has limited accuracy due to various reasons including the overlap of peaks from different elements in the spectrum [74].

In order to determine the orientation of grains in a substrate and superconducting layer, trans-

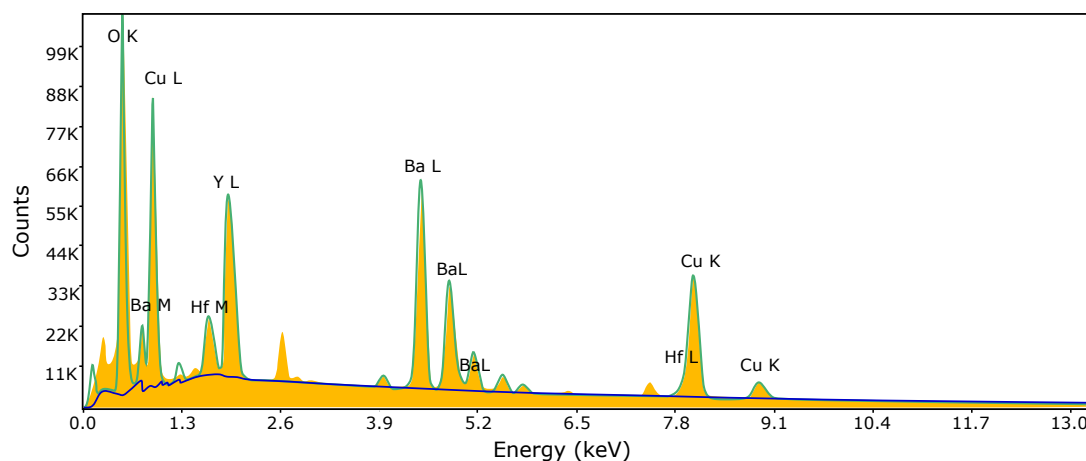


Figure 2.3.8: Typical EDX spectrum of a YBCO superconductor. The yellow area shows the X-rays that are collected by the detector, while the green line represents the fit that detects the energy edges of the various elements. The blue line shows the background that is subtracted to obtain the fit.

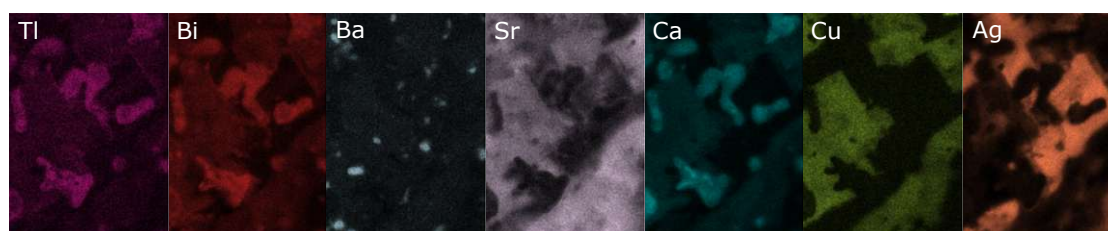


Figure 2.3.9: Example of EDX elemental mapping. The intensity of the color is directly related to the amount of the respective element present in an area.

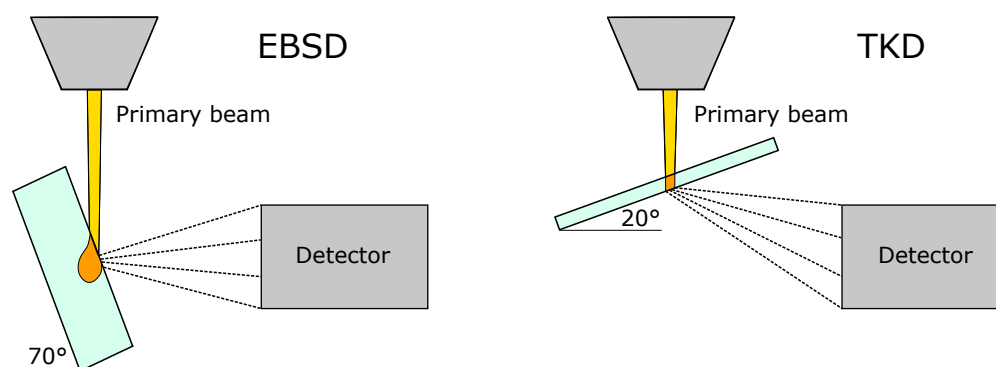


Figure 2.3.10: Experimental setup for EBSD (left panel) and TKD (right panel) in the SEM. For TKD, the sample only needs to be tilted 20° with respect to the detector which leads to a smaller interaction volume inside the sample and therefore to a higher spatial resolution.

mission Kikuchi diffraction (TKD), also known as transmission electron backscatter diffraction (t-EBSD), experiments were conducted using the SEM. For conventional EBSD experiments, the sample needs to be tilted by about 70° with respect to the EBSD camera, see Figure 2.3.10. The primary electron beam is diffracted on the surface of the sample, and the resulting diffraction patterns reflect the crystal structure of the sample. For TKD experiments, the sample needs to be electron transparent, therefore the same sample preparation as for TEM imaging is necessary. With a dedicated holder for TEM lamellae the sample is only tilted 20° with respect to the EBSD camera which leads to a smaller interaction volume in the sample and thus a higher spatial resolution. A more detailed description of the TKD technique and its advantages can be found in [75, 76].

Chapter 3

Results and Discussion

The superconducting and microstructural properties of three different high temperature superconducting materials are presented in this chapter. Thin films of YBCO, Fe(Se,Te) and Tl-1223 on technical templates and single crystalline substrates were investigated by means of magnetization measurements in order to understand the relationship between macroscopic and local current transport in these materials. A quantitative analysis of magnetic granularity was developed and investigations with electron microscopy were implemented in order to relate the local current carrying capability to microstructural features in each material.

3.1 YBCO

Superconducting thin films of $\text{YBa}_2\text{Cu}_3\text{O}_{7-\delta}$ (YBCO) and YBCO + 10 % BaHfO_3 (BHO) were prepared on RABiTS and IBAD-MgO based templates by pulsed laser deposition, as described in chapter 2.1. The following sections give an overview of the experimental results on the macroscopic superconducting properties, obtained by means of SQUID magnetometry, the local superconducting properties, obtained by means of SHPM, as well as a quantitative analysis of the magnetic granularity and a microstructural analysis, conducted with scanning and transmission electron microscopy. Finally, a discussion on the magnetic granularity and its implications for coated conductors based on this material is presented. The most important findings were published in [64].

3.1.1 Experimental Results

Four undoped and four BHO-doped YBCO samples on RABiTS templates with thicknesses 2 μm , 1 μm , 500 nm and 250 nm were investigated. For comparison, two YBCO films on IBAD-MgO based templates were analyzed, a 500 nm BHO-doped film and a 1 μm pure YBCO film. For better readability, the most important findings are presented in the following sections, while the rest of the experimental results can be found in appendices A–D.

3.1.1.1 Superconducting Properties: Macroscopic Magnetic Properties

The critical temperature, T_c , of the BHO-doped and pure YBCO films, obtained by measuring the magnetic susceptibility after zero-field cooling and applying a field of 0.5 mT along the c -axis of the sample, is presented in Figure 3.1.1. The measured BHO-doped samples (shown in (a)) exhibit a slight suppression of T_c of 1 K – 3 K as compared to the pure YBCO films on RABiTS, where T_c ranges from 91 K to 90 K (shown in (b)). For better comparison, Figure 3.1.1(c) shows a closeup of the transition region for all curves. While the pure film on IBAD-MgO exhibits a lower T_c compared to the respective films on RABiTS, both films on IBAD-MgO show a sharper transition into the superconducting phase, indicating a more homogeneous distribution of the superconducting properties. The T_c values and the global critical current density, J_c^G , in self-field at 5 K, 30 K and 77 K are summarized in Table 3.1.

The field dependence of J_c^G of the pure and BHO-doped samples is shown in Figure 3.1.2. At 5 K (a,b), the BHO-doped films on RABiTS exhibit a significantly higher J_c^G for all thicknesses and fields than the undoped films on RABiTS. Moreover, the field dependence of J_c^G is positively reduced for the BHO-doped films. In both cases, the 250 nm, 500 nm and 2 μm J_c^G curves show a similar trend, only at low fields the latter behave differently. This is the region, where the self-field of the superconductor has to be considered, which is most prominent for the highest thickness and therefore leads to an underestimation of J_c^G in low fields. While the 1 μm BHO-doped film exhibits the highest critical current density of all films on RABiTS, the respective 1 μm pure YBCO film has an underwhelming low J_c^G , even though it has the highest T_c of all samples. At 30 K (c,d), the advantage of BHO-doping can still be observed for the films on RABiTS, while at 77 K (e,f), the difference in J_c^G between the BHO-doped and pure YBCO

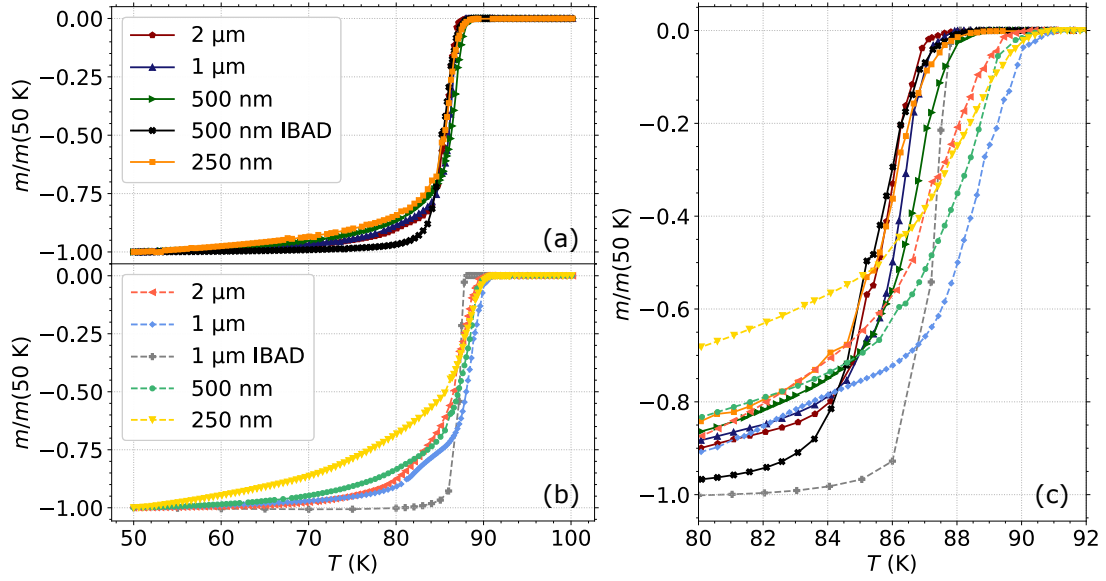


Figure 3.1.1: Temperature dependence of the normalized magnetization of the BHO-doped (a) and undoped (b) YBCO films on RABiTS and IBAD-MgO templates. A closeup of the transition region shows the slight suppression of T_c in the BHO-doped samples compared to the pure YBCO samples (c). *Measurement data provided by Ilya Shipulin.*

		T_c	$J_c^{G, sf}$ (5 K)	$J_c^{G, sf}$ (30 K)	$J_c^{G, sf}$ (77 K)
		(K)	(MA/cm ²)	(MA/cm ²)	(MA/cm ²)
BHO-doped	2 μm	87.6	-	6.1	0.55
	1 μm	87.8	19.0	10.7	1.10
	500 nm	88.8	16.5	9.7	1.30
	500 nm IBAD	88.4	21.9	11.0	1.08
	250 nm	88.6	14.5	8.2	1.07
pure	2 μm	90.0	6.7	4.3	0.34
	1 μm	91.0	5.4	2.8	0.38
	1 μm IBAD	87.8	19.1	11.5	0.91
	500 nm	90.4	8.2	4.6	0.66
	250 nm	90.6	8.0	4.2	0.75

Table 3.1: Critical temperature T_c and global critical current density J_c^G in self-field at 5 K, 30 K and 77 K of the BHO-doped and pure YBCO films.

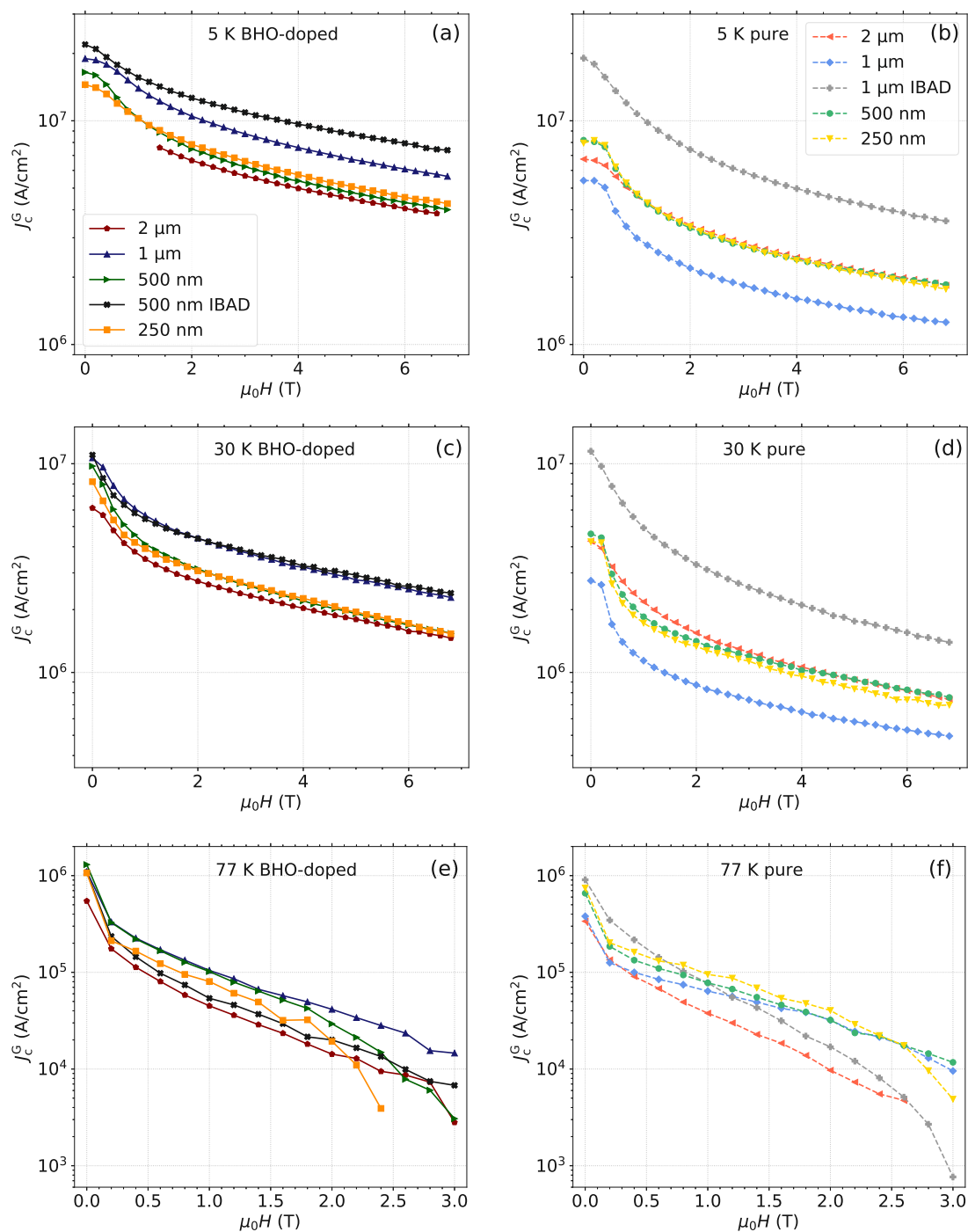


Figure 3.1.2: Field dependence of the global critical current density J_c^G of BHO-doped and pure YBCO samples at 5 K (a,b), 30 K (c,d) and 77 K (e,f).

films is not as prominent. Nevertheless, also at 77 K, the BHO-doped films still exhibit higher self-field J_c^G values. Globally, the BHO-doped film on the IBAD-MgO based template exhibits the best J_c^G performance of all samples at 5 K. The respective pure film on IBAD-MgO has a similar self-field J_c^G , however, the in-field performance is significantly weaker. At 30 K, the BHO-doped film on IBAD-MgO loses its advantage compared to the 1 μm film on RABiTS (cf. Figure 3.1.2(c)), and at 77 K both films on IBAD-MgO do not seem to have an advantage over the YBCO films on RABiTS. Except for the 2 μm samples, the films on RABiTS even outperform the films on IBAD-MgO at most fields. The field dependence of J_c^G at 65 K and a direct comparison of J_c^G of the BHO-doped and pure YBCO films for each thickness are shown in appendix A in Figures A.1 and A.2, respectively.

3.1.1.2 Superconducting Properties: Magnetic Granularity

The remnant field profiles at 77 K of all samples on RABiTS, which were recorded with the wide area Hall scanner and exhibit a spatial resolution of 50 μm , are presented in Figure 3.1.3. The BHO-doped films (a–d) exhibit generally homogeneous Bean profiles apart from some minor disturbances caused by scratches on the film surface. While the 2 μm pure YBCO film (e) shows a similar homogeneous remnant field profile, the thinner pure films (f–h) exhibit a higher magnetic granularity. Generally, the BHO-doped samples retain higher maximum trapped fields for all thicknesses than the respective pure films.

Figure 3.1.4 shows the local current density maps at 77 K of the BHO-doped (a–d) and pure (e–h) YBCO films. The displayed current density corresponds to the local critical current density, J_c^L , except at the discontinuity lines, which were described in chapter 2.2.2. In the BHO-doped samples a slight anisotropy in J_c^L can be observed, which is higher in the y -direction (vertical direction in all Hall maps). This is caused by the elongation of the underlying Ni-W grains in rolling direction (y -direction) and is indicated by an extended zero- J_c^L line in x -direction. The 1 μm , 500 nm and 250 nm pure YBCO films exhibit a significantly higher granularity, which is represented by the currents that meander around areas with lower J_c^L . The white circles in Figure 3.1.4 indicate the areas, where round spots for high-resolution Hall mapping were prepared. The numbers 1 and 2 inside the circles refer to the first and second spot that was prepared, respectively.

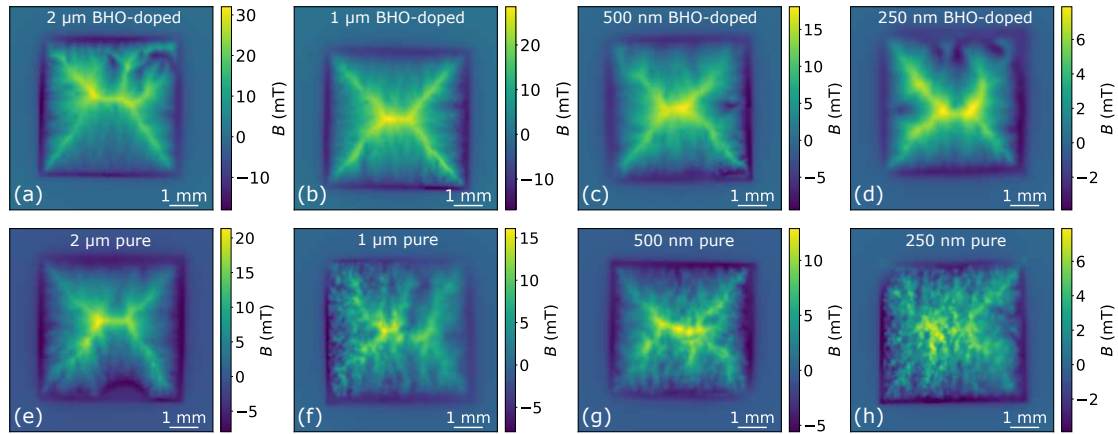


Figure 3.1.3: Remnant field profiles at 77 K with a spatial resolution of 50 μm of the BHO-doped (a–d) and pure (e–h) YBCO films.

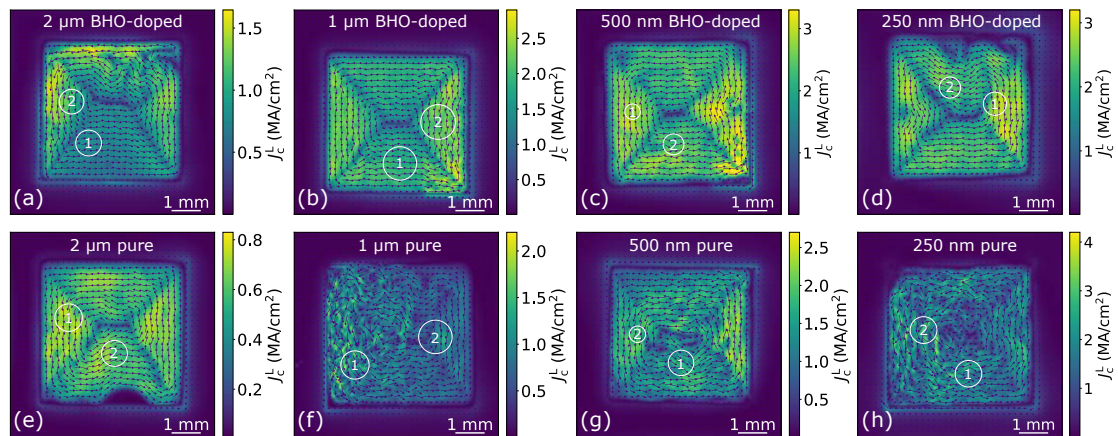


Figure 3.1.4: Local current density maps at 77 K with a spatial resolution of 50 μm of the BHO-doped (a–d) and pure (e–h) YBCO films. The white circles indicate the areas where spots were prepared for high-resolution SHPM.

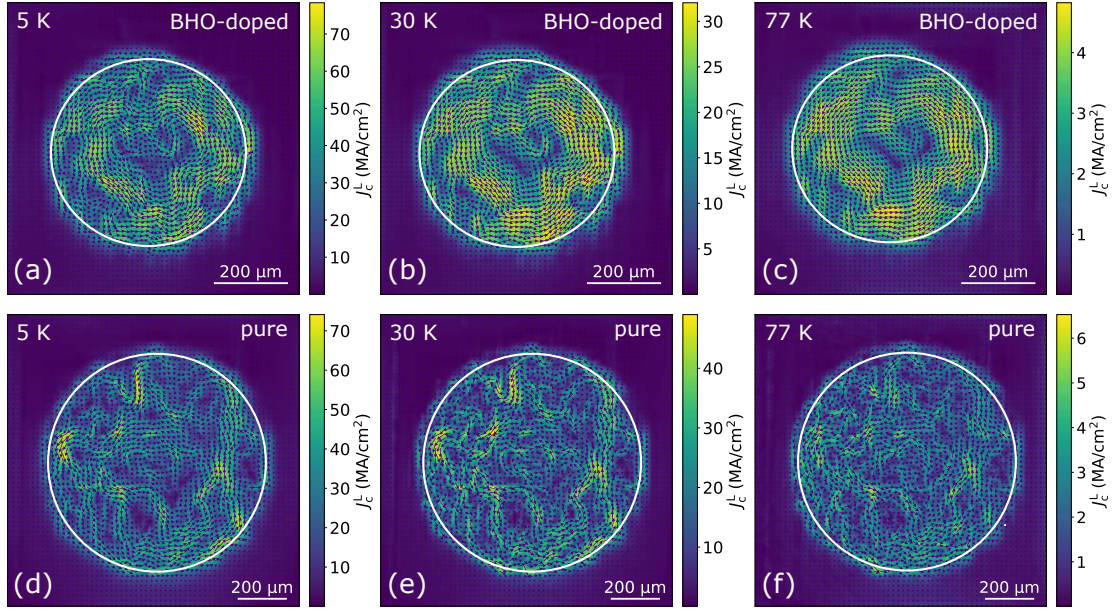


Figure 3.1.5: Local current density maps at 5 K, 30 K and 77 K of spot 1 of the 500 nm BHO-doped film (a–c) and spot 1 of the 500 nm pure YBCO film (d–f) with a spatial resolution of 7 μm . J_c^L values within the white circles were considered for the statistical analysis.

High-resolution SHPM was performed at 5 K, 30 K and 77 K with a spatial resolution of 7 μm for all spots, the remnant field profiles and local current density maps can be found in appendix B. Figure 3.1.5 shows the local current density maps at all three temperatures of spot 1 of the 500 nm BHO-doped film on RABiTS (a–c) and spot 1 of the 500 nm pure YBCO film on RABiTS (d–f) with a spatial resolution of 7 μm . A reduction of magnetic granularity with increasing temperature can be observed for the BHO-doped sample, as the local current map becomes more homogeneous. In the pure YBCO film, the reduction of granularity with increasing temperature is not obvious by sight of eye.

In order to quantify the magnetic granularity, a statistical analysis of the local critical current densities was employed, as described in chapter 2.2.4. For the calculation of the distributions only J_c^L values that are within the white circles in Figure 3.1.5 were considered. Figure 3.1.6 shows the J_c^L distributions of the 500 nm BHO-doped and pure spots at 5 K (a), 30 K (b) and 77 K (c). The mean J_c^L values, μ , of the BHO-doped spots at 5 K are around 46 MA/cm², while $\mu \sim 30$ MA/cm² was found for the respective pure spots. The average local critical current density is generally higher for the BHO-doped spots, also at higher temperatures. At 5 K, the

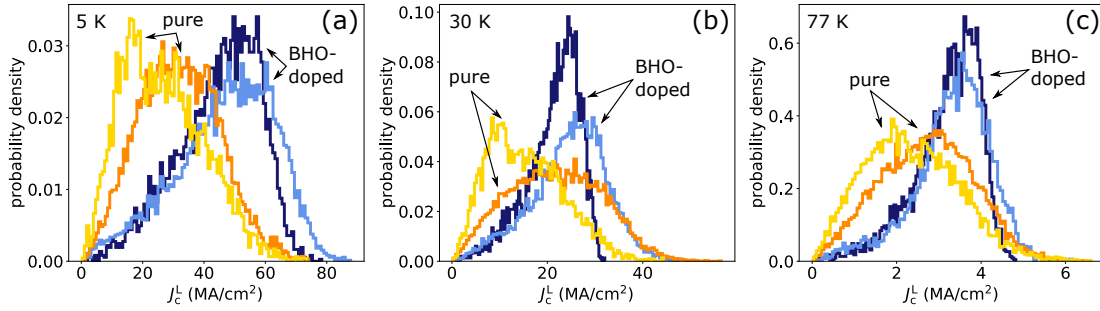


Figure 3.1.6: J_c^L distributions of the 500 nm BHO-doped and pure YBCO spots on RABiTS at 5 K (a), 30 K (b) and 77 K (c). The reduced granularity in the BHO-doped samples is represented by sharper peaks.

magnetic granularity, which is represented by the relative standard deviation, σ_n , is around 32 % for the BHO-doped spots, while $\sigma_n \sim 45$ % was observed for the respective pure spots. At 77 K, $\sigma_n \sim 26$ % was determined for the BHO-doped spots, which corresponds to a sharper peak in the J_c^L distribution, while again a higher $\sigma_n \sim 44$ % was found for the pure YBCO spots. The J_c^L distributions that show the difference between the BHO-doped and undoped samples for the other film thicknesses can be found in appendix C.

A comparison of the J_c^L distributions with respect to film thickness at 5 K is shown in Figure 3.1.7. The J_c^L distributions of all investigated BHO-doped spots on RABiTS are shown in the left panel. Two spots were prepared for each thickness, as indicated by the white circles in Figure 3.1.4. The 2 μm film showed an asymmetric Bean profile with a large low- J_c^L area and a small high- J_c^L area (cf. Figure 3.1.4(a)). One spot was prepared in each area, the high-resolution J_c^L maps at 5 K are shown in Figure 3.1.8. Spot 1, which was prepared from the low- J_c^L area, shows a homogeneous current density map except for some minor disturbances (a), while spot 2 exhibits indeed higher local currents with a less homogeneous overall local current density (b). Measurements of the critical temperature of both spots show that spot 2 exhibits a slightly higher T_c (cf. Figure 3.1.8(c)), however, spot 1 shows a sharper transition into the superconducting phase which corresponds well to the more homogeneous current map. In order to investigate if the difference in T_c stems from a difference in oxygen doping, both spots were annealed at 400 °C for 24 hours, but no change in T_c could be observed after annealing. The asymmetry in the Bean profile is therefore probably caused by a temperature gradient on the

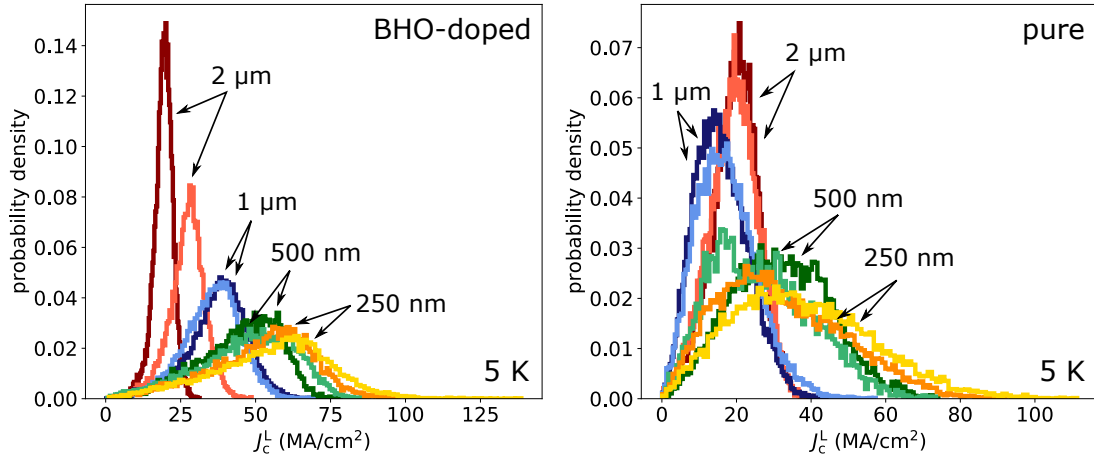


Figure 3.1.7: J_c^L distributions with respect to film thickness of the BHO-doped samples on RABiTS (left panel) and the pure YBCO samples on RABiTS (right panel) at 5 K. The magnetic granularity decreases with increasing film thickness.

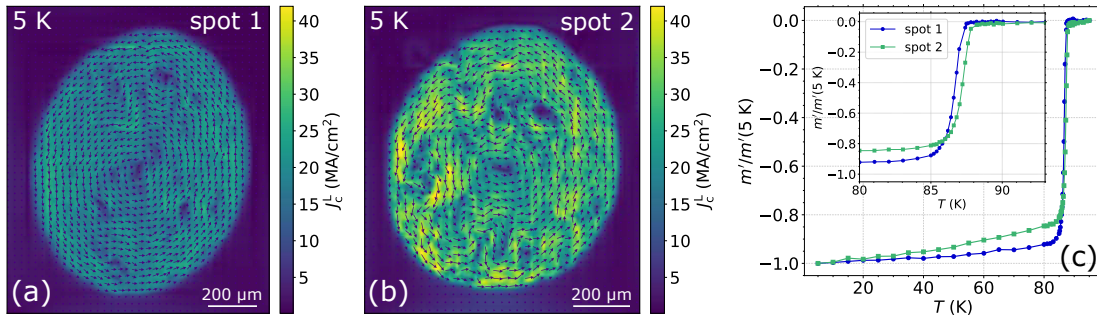


Figure 3.1.8: The two 2 μm BHO-doped spots exhibit different local current densities (a,b). Measurements of the critical temperature show, that spot 2 exhibits a slightly higher T_c (c).

sample surface during deposition, which leads to a slightly different surface morphology of both spots and therefore to a difference of J_c^L . This can also be observed in the J_c^L distributions in the left panel of Figure 3.1.7 in the form of two distinguishable peaks. For all other thicknesses, both spots exhibit similar J_c^L distributions.

The J_c^L distributions of the BHO-doped spots on RABiTS clearly show, that the mean J_c^L values and the magnetic granularity decrease with increasing film thickness. The thinner films exhibit a much higher granularity, which is represented by broad distributions, while the granularity is reduced with higher thickness, represented by sharper peaks in the histogram. A similar situation is found for the pure YBCO spots on RABiTS (Figure 3.1.7 right panel), except for

		5 K		30 K		77 K	
		μ (MA/cm ²)	σ_n (%)	μ (MA/cm ²)	σ_n (%)	μ (MA/cm ²)	σ_n (%)
BHO-doped	2 μm	19.2 / 27.0	17 / 23	11.9 / 14.2	17 / 19	1.11 / 1.80	16 / 21
	1 μm	37.3 / 35.5	27 / 27	19.8 / 21.3	21 / 21	2.22 / 2.50	21 / 18
	500 nm	44.8 / 47.1	29 / 34	21.3 / 24.6	26 / 32	3.21 / 3.33	24 / 27
	250 nm	52.2 / 55.5	32 / 35	32.2 / 30.2	30 / 29	3.51 / 3.31	24 / 26
pure	2 μm	19.7 / 19.2	31 / 34	12.7 / 13.8	26 / 33	1.02 / 0.96	27 / 28
	1 μm	16.0 / 17.4	44 / 47	8.66 / 8.72	45 / 48	1.25 / 1.19	35 / 37
	500 nm	31.9 / 26.7	41 / 50	21.8 / 15.5	44 / 50	2.72 / 2.35	40 / 47
	250 nm	32.0 / 37.8	52 / 49	18.7 / 15.8	52 / 48	2.93 / 2.85	52 / 46

Table 3.2: Mean J_c^L values, μ , and relative standard deviations, σ_n , of the BHO-doped and pure YBCO spots on RABiTS at 5 K, 30 K and 77 K. The first and second values correspond to the first and second investigated spots, respectively.

the 1 μm film, which also exhibits the lowest critical current density on a local scale. The mean J_c^L values, as well as the relative standard deviations of all spots on RABiTS at 5 K, 30 K and 77 K can be found in Table 3.2.

Figure 3.1.9 shows the local current density maps of the two samples on IBAD-MgO templates. The current maps with a spatial resolution of 50 μm at 77 K of the 500 nm BHO-doped sample (a) and the 1 μm pure YBCO sample (c) both exhibit asymmetric Bean profiles, similar to the 2 μm BHO-doped film on RABiTS. This is probably caused again by a temperature gradient on the sample surface during the deposition process. No granularity can be observed at this resolution, the white circles indicate the areas where spots were prepared for high-resolution SHPM. For both samples, one spot was prepared in the high- J_c^L area and one spot was prepared in the low- J_c^L area. Figures 3.1.9 (b) and (d) show the high-resolution maps at 5 K of the high- J_c^L spots for the BHO-doped and pure sample, respectively. The spatial resolution of these maps is 7 μm , however, due to the small grain size of the IBAD-MgO template (~ 50 nm), no granularity can be resolved and the results are homogeneous J_c^L maps.

The J_c^L distributions in Figure 3.1.10 show the difference in granularity for the two technical templates at 5 K, 30 K and 77 K. In the case of the 500 nm BHO-doped samples (a–c), the two spots on RABiTS exhibit a much broader distribution, while the granularity cannot be resolved for the spots on the IBAD-MgO template, which results in sharp peaks. The different positions

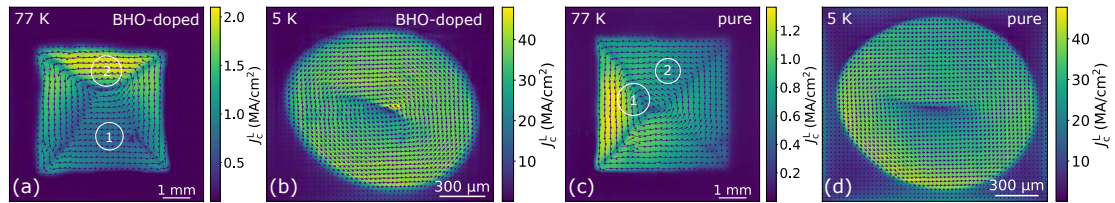


Figure 3.1.9: Local current density maps of the YBCO films on IBAD-MgO templates. No granularity can be observed in the J_c^L maps of the 500 nm BHO-doped film (a,b) and the 1 μm pure YBCO film (c,d).

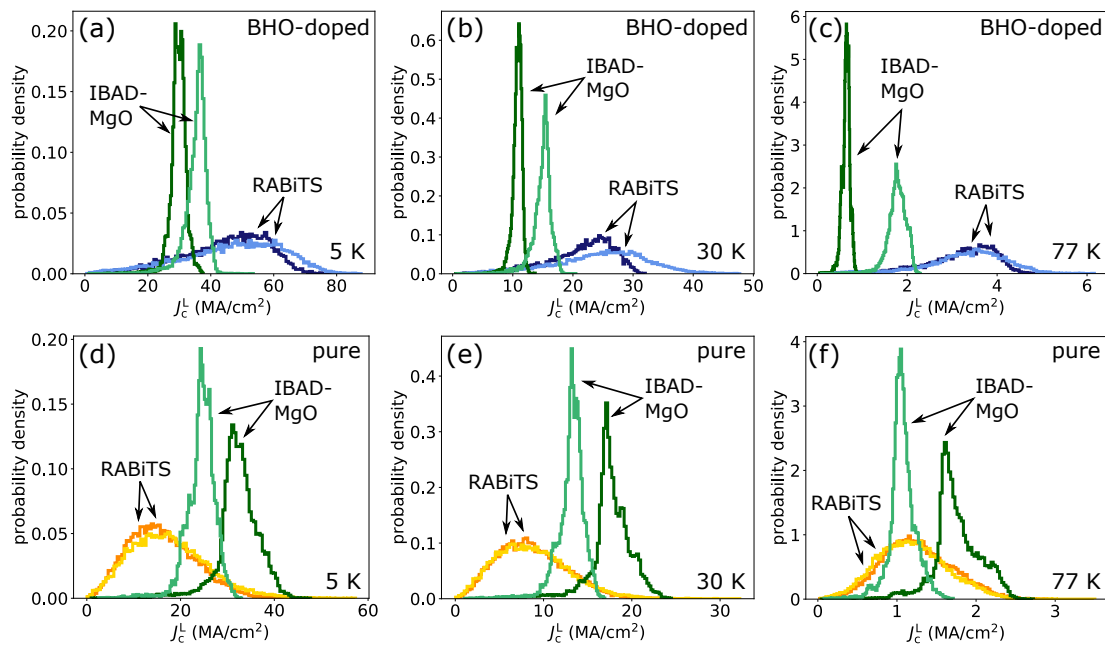


Figure 3.1.10: J_c^L distributions of the 500 nm BHO-doped samples on RABiTS and IBAD-MgO (a–c) and the 1 μm pure YBCO films on RABiTS and IBAD-MgO (d–f). The high granularity on RABiTS is represented by the broad distributions.

of the peaks represent the different mean J_c^L values of the two spots. Although the granularity is higher for the two spots on RABiTS, they also exhibit a higher average critical current density on a local scale. In the case of the 1 μm pure YBCO samples (e–f), the spots on IBAD-MgO also exhibit a higher mean local critical current density compared to the spots on RABiTS. However, the 1 μm pure YBCO film on RABiTS also exhibits an underwhelming low J_c^G (cf. Figure 3.1.2). In both cases, with increasing temperature, the two IBAD-MgO peaks are shifted to lower values compared to the RABiTS distributions.

3.1.1.3 Microstructure

The superconducting film surfaces of all BHO-doped and pure YBCO samples on RABiTS templates were investigated by means of scanning electron microscopy and for each film thickness an area was carefully chosen for the preparation of a TEM lamella. The TEM results of the 2 μm and 500 nm films are shown in this section, a summary of the results on the 1 μm and 250 nm films can be found in appendix D. Figure 3.1.11 shows a comparison of the BHO-doped (a,c,e,g) and pure (b,d,f,h) film surfaces with the same magnification for all thicknesses. The 2 μm , 1 μm and 500 nm BHO-doped samples exhibit a largely homogeneous film surface, some secondary phase precipitates and a -axis grains can be observed. The latter occur if there is a disturbance in the superconducting layer and a YBCO grain grows perpendicular instead of parallel to the substrate surface, i.e. the a -axis of the grain is perpendicular and the c -axis is parallel to the film surface. The a -axis grains become more prominent with higher thickness (bright elongated structures in (a)). In the thinner films, especially the 250 nm BHO-doped film, the underlying Ni-W grain structure of the substrate becomes visible through slight variations of the roughness and pore density in the superconducting layer. The variation of pore density in adjacent grains is much more prominent in the thin pure YBCO films and variations in the surface structure can also be observed in the 2 μm pure sample. The 1 μm pure sample, which exhibits an underwhelming low critical current density, shows a largely porous film surface with loosely connected YBCO islands (d).

A comparison of the two spots with low- and high- J_c^L that were prepared from the 2 μm BHO-doped sample is given in Figure 3.1.13. The film surface of both spots exhibits a large number of a -axis grains, however, they appear to be more prominent in spot 2, which has the

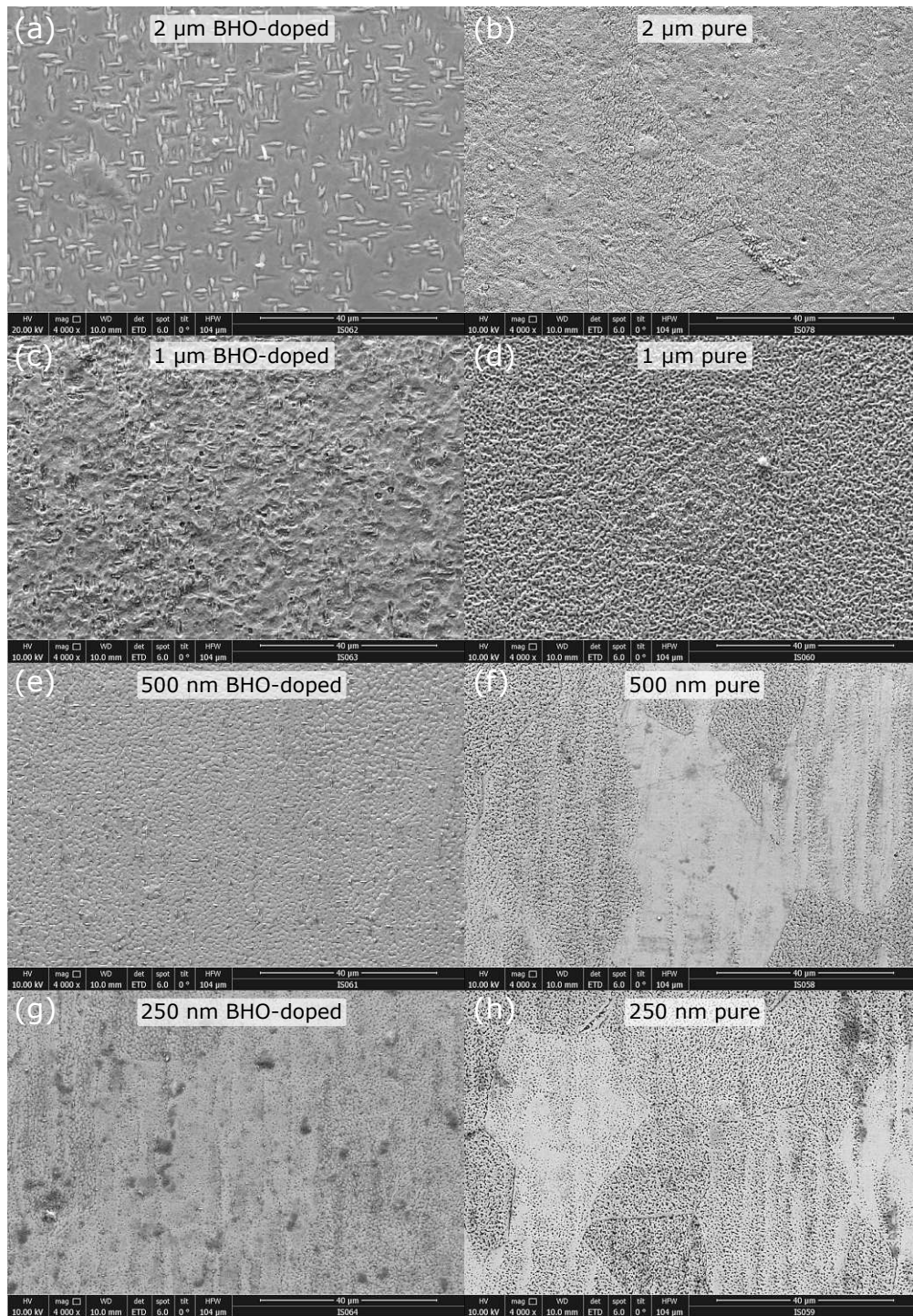


Figure 3.1.11: SEM images of the superconducting layer of the BHO-doped films (a,c,e,g) and the undoped YBCO films (b,d,f,h) of all thicknesses.

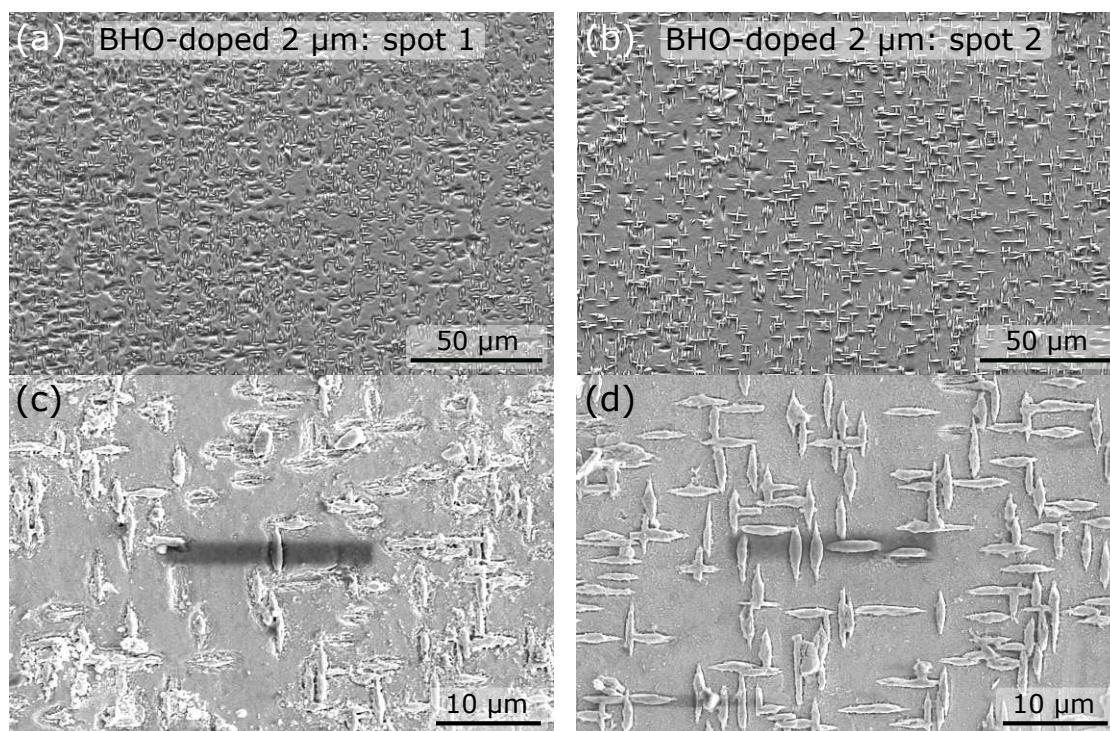


Figure 3.1.12: Comparison of the surface of the low- J_c^L spot 1 (a) and high- J_c^L spot 2 (b) of the 2 μm BHO-doped YBCO sample. The black bars in (c,d) indicate the areas where TEM lamellae were prepared for the respective spots.

higher J_c^L . Since the a -axis grains become more prominent with increasing film thickness, this could point to a variation of the film thickness in this sample. Therefore a TEM lamella was prepared for each spot, the black bars in Figures 3.1.12(c,d) indicate the areas on the sample surface from which the lamellae were taken.

Figure 3.1.13 shows TEM images of spot 1 (i) and spot 2 (ii). The HAADF images give an overview of both lamellae (i,ii)(a) and show that the film thickness is approximately the same for both spots. Both lamellae reveal a dense superconducting layer, the sharp contrast variations in the HAADF images point to secondary phases in the layer. It can also be observed that the a -axis grain rises indeed more prominently from the surface of the superconducting layer in spot 2 (ii,a). TEM BF images of the dense superconducting layer show that both spots exhibit the typical mixed defect structure of BHO-doped YBCO films (i,ii)(b), with BHO-nanorods that are roughly parallel to the c -axis and BHO nanoparticles and layers in the ab -planes [24, 61, 62, 77–80]. Diffraction patterns were recorded in four selected areas in the lamella of spot 1,

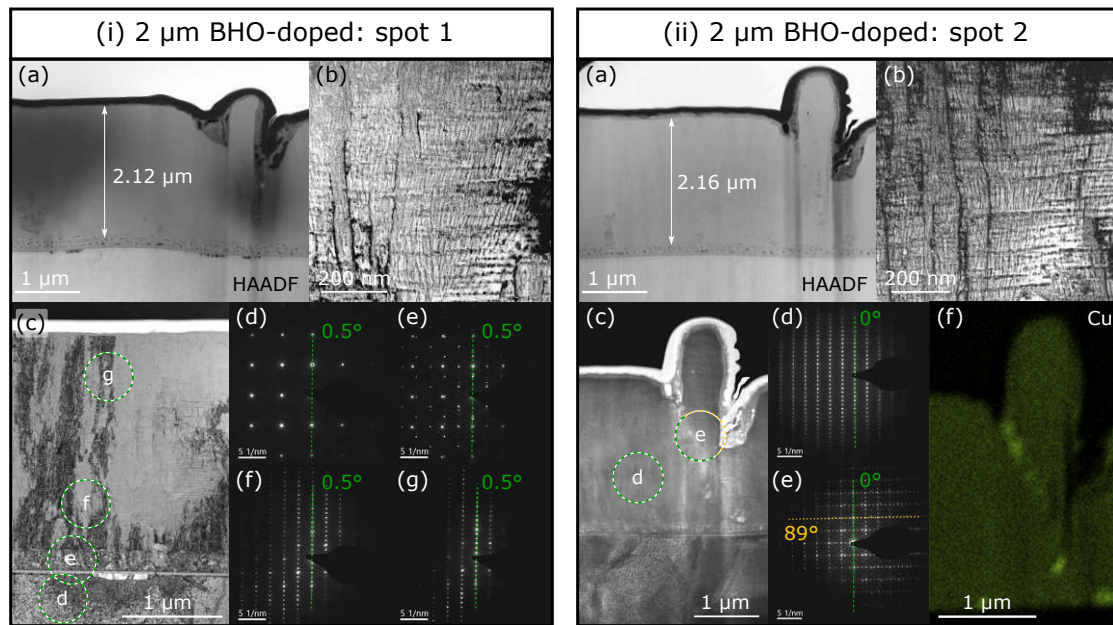


Figure 3.1.13: TEM images of the low- J_c^L spot 1 (i) and high- J_c^L spot 2 (ii) of the 2 μm BHO-doped YBCO film. Both spots exhibit the same thickness and a similar microstructure.

as indicated by the circles in (i,c). The vertical lines of points in the diffraction patterns that keep the same orientation (i,d–g) indicate the epitaxial growth of the superconducting layer and buffer layers on the Ni-W substrate. In the lamella of spot 2, two diffraction patterns were recorded from selected areas, as indicated by the circles in (ii,c). The vertical lines of diffraction points in (ii,d) (green dashed line) indicate again the epitaxial growth of the superconducting layer, while a set of horizontal points in (ii,e) (yellow dotted line) corresponds to the tilted c -axis by 89° of the a -axis grain. An elemental map showing the copper content of the a -axis grain and the surrounding area shows that these grains tend to originate at secondary phase precipitates, in this case at an area with high copper content (ii,f). Since both spots exhibit the same microstructural properties, it can be assumed, that the difference in J_c^L stems from a temperature gradient on the sample surface during deposition, which leads to a slightly higher T_c and therefore higher J_c^L in spot 2.

A comparison of the current maps and SEM images of the 2 μm BHO-doped and pure YBCO films can be found in Figure 3.1.14. The white rectangle in the current map of the BHO-doped sample (a) points to an area where the current flow is clearly disturbed. An investigation of the

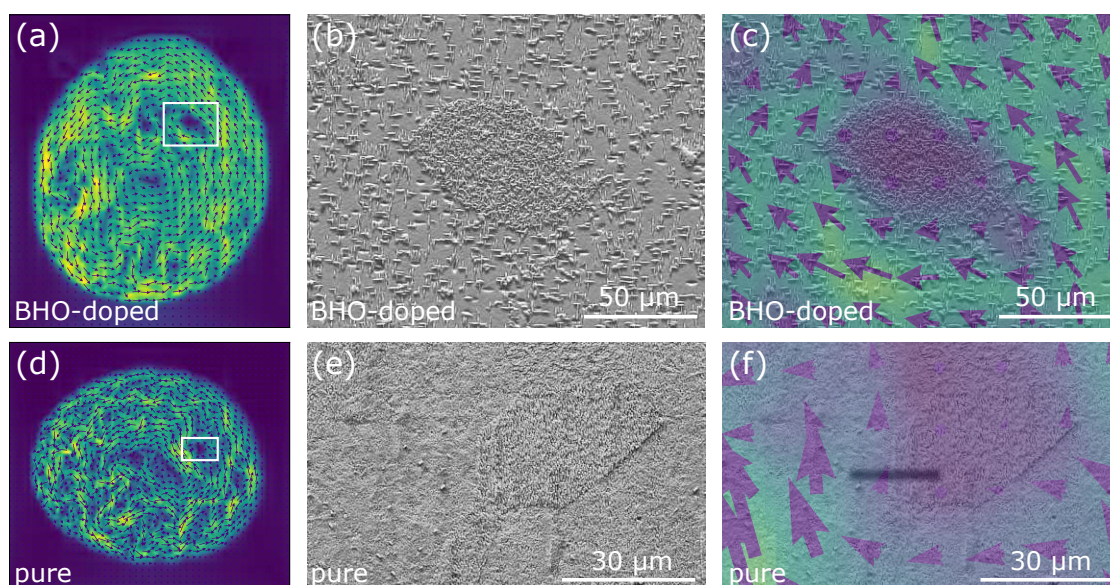


Figure 3.1.14: Comparison of the current maps and SEM images for the 2 μm BHO-doped sample (a–c) and for the 2 μm pure film (d–e). An overlay of the current map and SEM image shows how the currents flow around areas of disturbed film growth.

same area in the SEM shows that the film growth is severely disturbed in this area (b). This is usually caused by an underlying Ni-W grain with a high surface porosity or high out-of-plane tilt. An overlay of the SEM image and the current map clearly shows how the currents flow around the disturbed area (c). The white rectangle in the current map of the pure sample (d) points again to an area of inhomogeneous current flow. In this case, the SEM image of the same area reveals a change of the surface roughness between adjacent grains (e) and an overlay with the current map shows how the currents flow around the grain which exhibits a faceted surface (f). The black bar indicates the area where a TEM lamella was prepared across this grain boundary (GB).

The HAADF images in Figures 3.1.15(a,b) reveal the difference in the superconducting layer on both sides of the grain boundary. On the left side of the GB (a), the superconducting film is homogeneous, although the difference to the BHO-doped sample becomes immediately apparent. Instead of a dense superconducting layer, many small pores can be identified. On the right side of the grain boundary, that exhibits the grain with a faceted surface, large pores that go from the surface deep into the superconducting layer can be seen (b). The TEM BF image in (c) shows

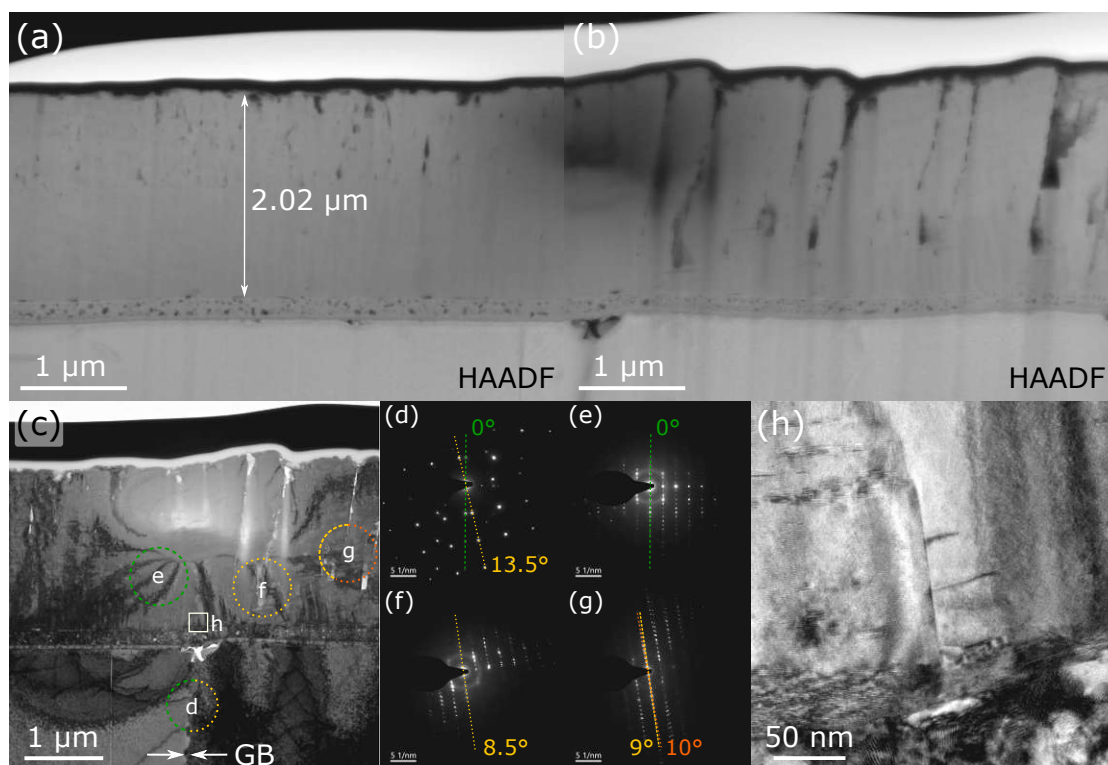


Figure 3.1.15: TEM images of the lamella taken from the 2 μm pure YBCO film. An out-of-plane tilt of 13.5° in the Ni-W grain leads to an inhomogeneous superconducting layer on the right side of the grain boundary.

the grain boundary region, the GB in the substrate is marked by horizontal white arrows. The circles indicate the selected areas that were chosen for the investigation of diffraction patterns. The diffraction pattern which corresponds to the GB in the substrate exhibits two sets of lines of diffraction points (d). One line is vertical (green dashed line) and corresponds to the grain on the left side of the GB, while the other line is tilted by 13.5° with respect to the vertical (yellow dotted line), which corresponds to the out-of-plane tilt of the grain on the right side of the GB. This behavior is transferred to the superconducting layer, as on the left side of the GB (with current flow), the diffraction pattern also shows vertical lines (e), while on the other side (without current flow), various out-of-plane tilts of the YBCO layer can be found (f,g). A high-resolution TEM image shows the GB in the transition region between the buffer layer and YBCO layer (h).

In the case of the 500 nm pure YBCO film, the underlying Ni-W grain structure is much more

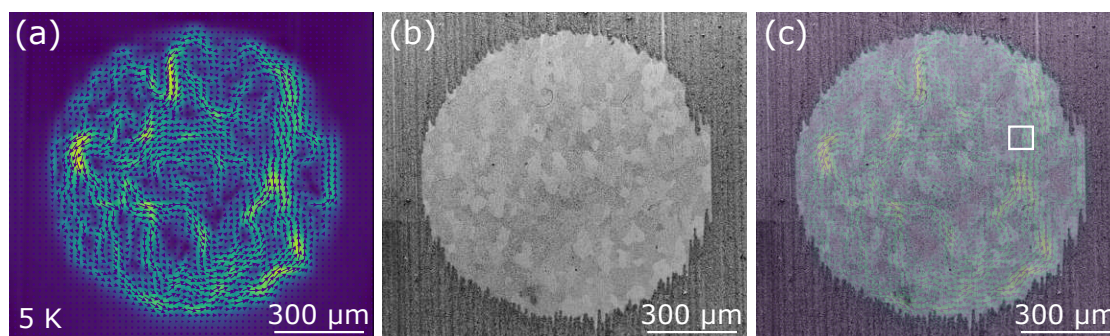


Figure 3.1.16: Current density map (a) and SEM image (b) of the 500 nm pure YBCO film. An overlay of both images shows that the currents meander in the brighter grains while avoiding the darker grains (c).

prominent and can be observed as changes in the roughness and pore density in the superconducting layer. Figure 3.1.16 shows a comparison of the current density map at 5 K and a SEM image of spot 1 of the 500 nm undoped YBCO film. The magnetic granularity can be observed in the current density map, visualized by the meandering currents (a). The SEM image of the same area shows, that grains with a denser surface appear bright, while more porous grains appear with a darker contrast (b). An overlay of both images clearly shows, that the currents meander in and through the brighter grains and mostly avoid the darker grains (c). The white rectangle marks the area that was chosen for the preparation of a TEM lamella.

The left panel in Figure 3.1.17 shows this area of the 500 nm pure YBCO film. The TEM lamella (indicated by the black bar) was prepared over a grain boundary between a dense grain with current flow (white arrows) and a porous grain without current flow (white dots). The right panel shows the area of the 500 nm BHO-doped film, where a TEM lamella was prepared across a GB between a smooth area and a clearly disturbed grain.

The TEM image in Figure 3.1.18(a) shows an overview of the grain boundary region of the 500 nm pure YBCO film (cf. Figure 3.1.17 left panel). The GB in the substrate is marked by horizontal white arrows. On the right side of the GB, a smooth transition from the Ni-W grain to the buffer layers (LZO/CeO₂) can be observed and the YBCO layer on top is homogeneous and dense and the supercurrents can flow unhindered. On the left side of the GB, the Ni-W grain exhibits a rough surface and transition to the buffer layers, pores and secondary phase precipitates become visible in the YBCO layer. The diffraction pattern in (b) shows the diffraction points from

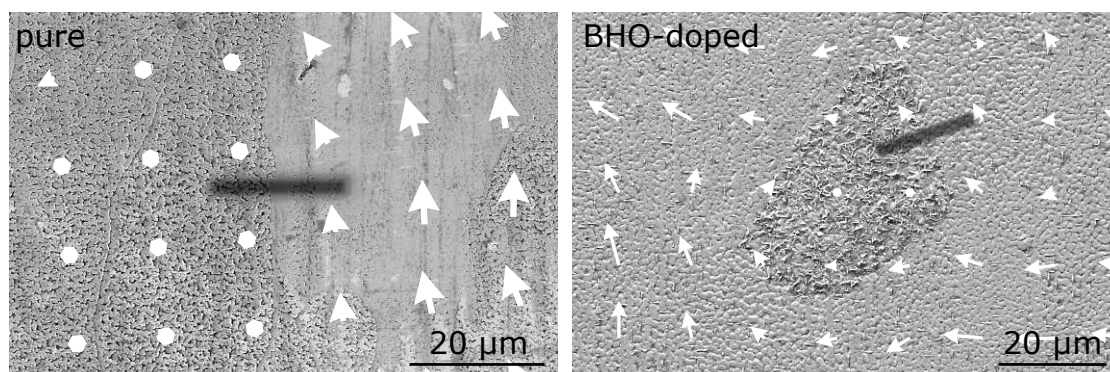


Figure 3.1.17: Areas that were chosen for the preparation of TEM lamellae in the 500 nm pure (left panel) and BHO-doped (right panel) YBCO films. In both films, TEM lamellae were prepared across grain boundaries between good current flow (white arrows) and no current flow (white dots).

the selected area in the substrate GB (indicated by the circle in (a)). A vertical line of diffraction points (green dashed line) can be observed, which corresponds to the Ni-W grain on the right, while another line of diffraction points is tilted by 8° with respect to the vertical (yellow dotted line) which corresponds to an 8° out-of-plane tilt of the Ni-W grain on the left. This shows, that the out-of-plane tilt of the substrate grain, as well as the rough surface structure of the Ni-W grain, leads to an imperfect growth of the superconducting layer on top. EDX analysis reveals, that the pores in the YBCO layer on the left side of the GB originate at secondary phase precipitates, as indicated by the elemental maps of Y, Ba and Cu, see Figure 3.1.18(c–e). The elemental maps show an increase in the Y signal in certain areas that lack other elements, which indicates the formation of Y_2O_3 platelets in the YBCO layer [77, 81].

Figure 3.1.19 gives an overview of the lamella that was prepared across a grain boundary in the 500 nm BHO-doped film (cf. Figure 3.1.17 right panel). The TEM image in (a) shows the GB region in the substrate, buffer layers and YBCO layer. The grain boundary in the substrate is marked by white horizontal arrows. On the right side of the GB, both buffer layers (LZO/CeO₂) appear smooth and transfer the biaxial texture of the metal tape to the superconducting layer. The YBCO layer is homogeneous and dense, with some secondary phase precipitates present and the supercurrents can flow unhindered. On the left side of the GB however, a stack of randomly oriented grains can be observed. The disturbance can also be noticed in the buffer layers, which copy the rough surface of the underlying Ni-W grain. The small white rectangle indicates the

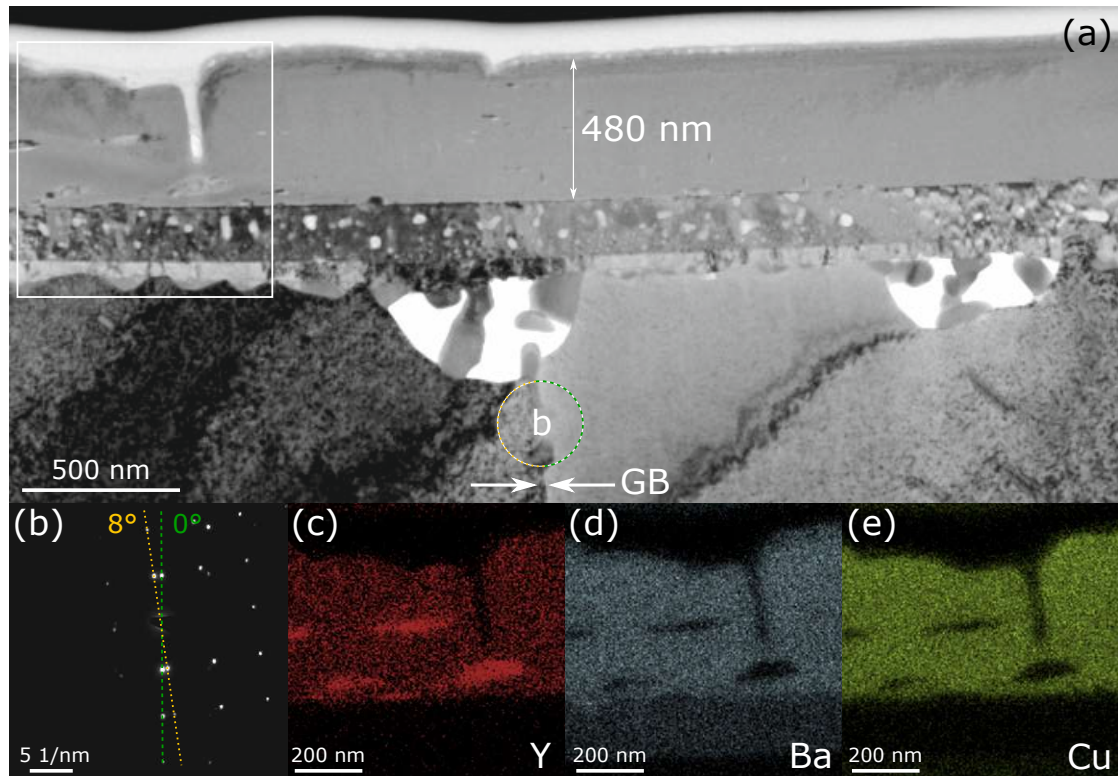


Figure 3.1.18: TEM images of the 500 nm pure YBCO film on RABiTS. Overview of the grain boundary region (a). The diffraction pattern of the substrate GB shows two different out-of-plane tilts on both sides of the GB (b). The rectangle in (a) indicates the area for EDX analysis: elemental map of Y (c), Ba (d) and Cu (e).

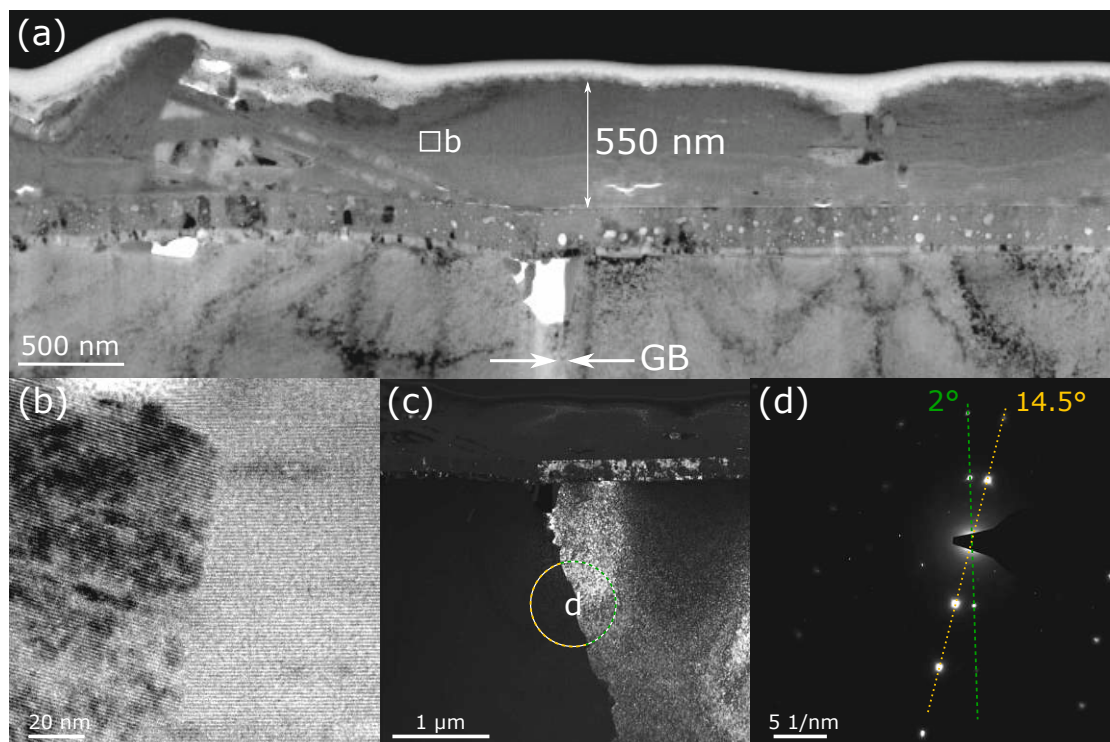


Figure 3.1.19: TEM images of the 500 nm BHO-doped film on RABiTS. Overview of the grain boundary region (a). A high-resolution TEM image shows the GB in the superconducting layer (b). A TEM dark field image visualizes the GB in the substrate and buffer layers (c). The diffraction pattern of the selected area in the substrate GB shows different lines of diffraction points that correspond to the out-of-plane tilt on both sides of the GB (d).

grain boundary region in the superconducting layer, which is shown in a high-resolution TEM image (b). Horizontal ab -planes can be found on the right side, while the lattice planes are tilted on the left side of the GB. The grain boundary in the substrate can be visualized beautifully with a TEM dark field image (c). The substrate and buffer layers on the right side of the GB appear bright, while the left side appears dark, indicating different orientations of the adjacent Ni-W grains. The diffraction pattern of the selected area in the substrate GB (indicated by the circle in (c)) shows two lines of diffraction points which can be associated with the out-of-plane tilt. One line is tilted by 2° with respect to the vertical (green dashed line) which corresponds to the ab -planes on the right side of the GB. The other line of diffraction points is tilted by 14.5° with respect to the vertical to the other direction (yellow dotted line) which corresponds to the tilted lattice planes on the left side of the GB. The grain boundary exhibits an out-of-plane GB angle of 16.5° and the large tilt of the Ni-W grain on the left side leads to a severe disturbance in the growth of the YBCO layer on top.

Figure 3.1.20 shows EBSD maps of the 500 nm BHO-doped (a,c) and 500 nm pure (b,d) YBCO films on RABiTS. The absolute misorientation (MO) is quite similar in both films, while the out-of-plane MO tends to be lower in the pure film, which is represented by a higher number of blue grains in (d). In both cases, the majority of grains are highly textured with an absolute MO of less than 8° from the ideal (001)[100] cube orientation. The colored lines between grains refer to the GB angle between adjacent grains, only GB angles with a value above 1° are indicated. The GB angles were calculated from the Euler angles of both grains and refer to the unique rotation necessary to align the crystallographic axes of both grains. The majority of GB angles are below 6° in both films (indicated by the yellow and red lines). The statistical distributions of the out-of-plane MO are shown in (e,f), generally the out-of-plane tilt is below 5° for both samples. However, the data represent only a small part of the sample area, and higher out-of-plane tilts were found in both films, as shown in Figures 3.1.18 and 3.1.19. The results from EBSD mapping show, that BHO-doping has no significant effect on the texture of the YBCO film on RABiTS.

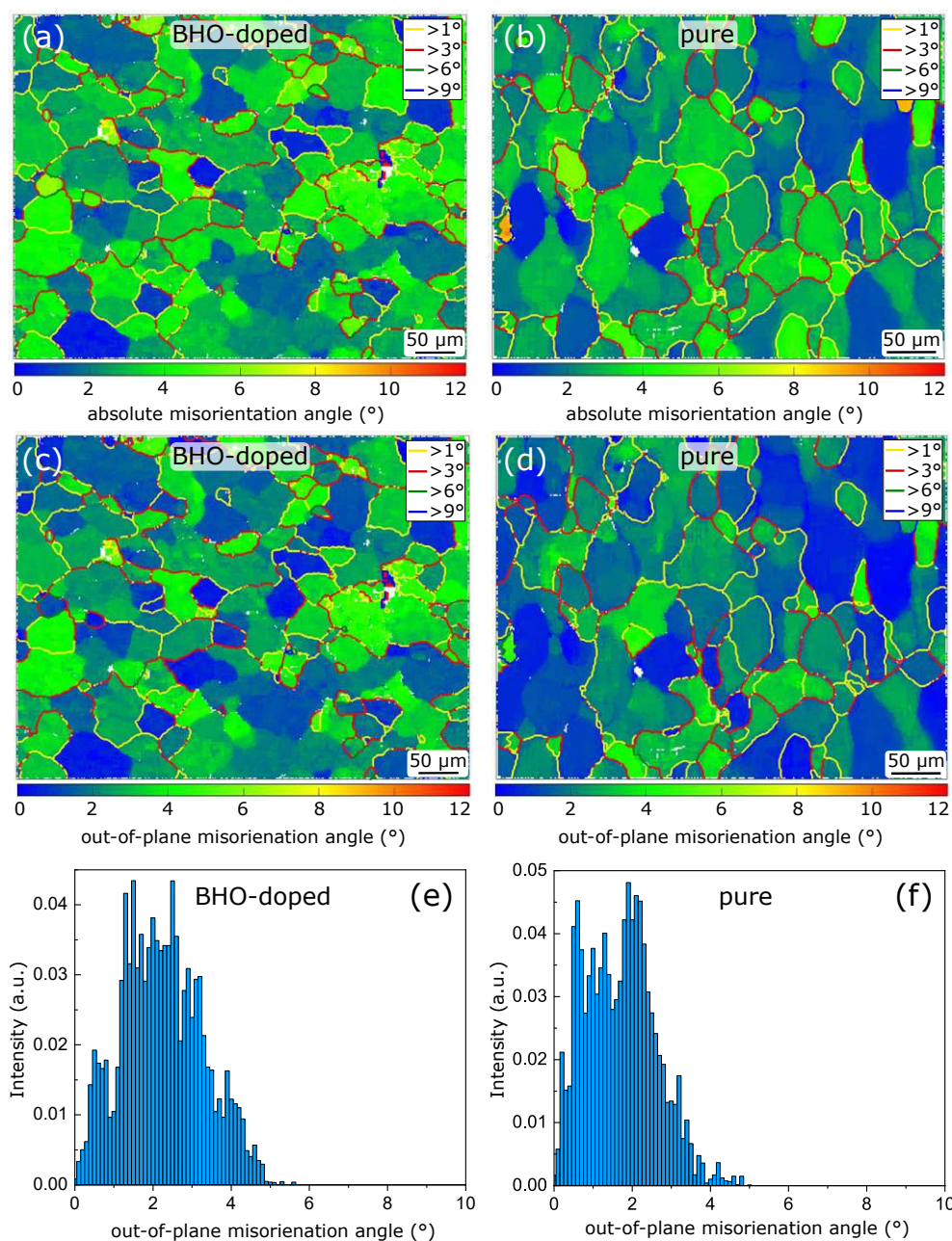


Figure 3.1.20: EBSD maps of the absolute and out-of-plane misorientation of grains in the 500 nm BHO-doped and pure YBCO films on RABiTS (a–d). The lines between grains refer to the GB angle between adjacent grains. The statistical distributions of the out-of-plane MO angles yield similar results for both films (e,f). *Credits: Ilya Shipulin.*

3.1.2 Discussion

BHO-doping in YBCO films on single crystalline substrates is known to increase the critical current density with a reduced magnetic field dependence [33, 34, 79]. This is a direct consequence of the introduction of pinning centers. While the increase in critical current density has also been observed for BHO-doped YBCO films on RABiTS [61], the results presented in this thesis give clear evidence that BHO-doping also affects the film growth and reduces magnetic granularity in RABiTS based films. For the quantitative evaluation of the magnetic granularity, the relative standard deviation σ_n was introduced.

Three main reasons can be identified that lead to the reduction of granularity in the studied samples. All three effects are visualized in Figure 3.1.21 which shows the dependence of the mean relative standard deviation, $\overline{\sigma_n}$, calculated from the two spots of each sample, on the sample thickness at 5 K and 77 K. First, σ_n is reduced with increasing film thickness, while the average local critical current density, μ , decreases as well. The dependence of the critical current density on the film thickness was shown e.g. by Foltyn et al. for YBCO films on IBAD-MgO templates and single crystalline substrates [82, 83]. They concluded, that the film morphology becomes much rougher with increasing thickness and related the drop in J_c with a change in the microstructure. This behavior can also be observed for the investigated YBCO films on RABiTS, by looking at the high- J_c^L end of the distributions in Figure 3.1.7. The high- J_c^L end, which is closest to the high values of the critical current densities in films on single crystals, shifts continuously to lower values in thicker films. At the same time, the corresponding statistical weight of the distribution is transferred to values below the peak position of the thinner film, which results in a sharper peak at lower J_c^L and therefore to a reduction of magnetic granularity. Unfortunately, this reduction is not necessarily beneficial, as it is driven by the elimination of high-current areas and globally, the thinner films exhibit a higher critical current density than the 2 μm films, which show the lowest magnetic granularity (cf. Figure 3.1.2).

Second, σ_n is reduced by BHO-doping, while the average local critical current density is increased compared to the pure YBCO films. This effect is purely beneficial, as the peak of the J_c^L distribution is near its high end for the BHO-doped samples, see Figure 3.1.6. For the pure YBCO films, however, much of the statistical weight is transferred to lower J_c^L values, which

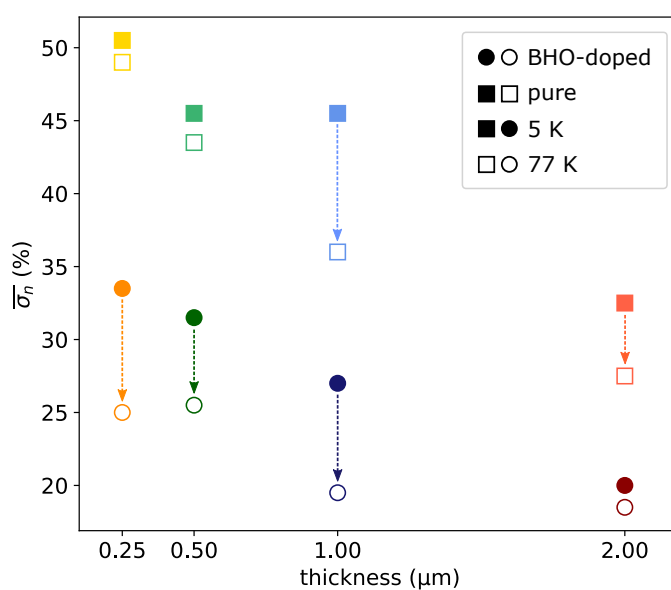


Figure 3.1.21: Dependence of the mean relative standard deviation on doping, sample thickness and temperature. A reduction of $\bar{\sigma}_n$ can be observed (i) for increasing film thickness, (ii) for the BHO-doped samples (circles) compared to the pure films (squares) and (iii) from 5 K (solid symbols) to 77 K (open symbols).

leads to a broader peak with an almost symmetric shape (cf. Figure 3.1.6(c)). This indicates an enhanced film growth in the BHO-doped YBCO samples. It was shown that BHO-doping reduces the formation of secondary phase precipitates in the superconducting layer [61]. Large precipitates, which cannot be easily overgrown by the superconducting layer, lead to the porous morphology of the undoped YBCO films (cf. Figures 3.1.15 and 3.1.18). The BHO-doped films, however, exhibit a denser YBCO layer with a mixed pinning landscape, as can be seen in Figure 3.1.13. The enhanced pinning certainly contributes to the higher global and local critical current density in the BHO-doped samples, nevertheless, the presented results show, that the reduction of granularity also plays an important role. Figure 3.1.6 shows, that the main mechanism that leads to the reduction of magnetic granularity in the BHO-doped samples is the suppression of low- J_c^L values. While the undoped YBCO film exhibits many low- J_c^L values that lead to the almost symmetric shape of the two distributions, the BHO-doped sample exhibits few low- J_c^L values, which leads to sharper peaks and maxima that are shifted towards higher values. It can be assumed, that BHO-doping leads to an enhanced film growth, where grains, that exhibit low or no current flow are suppressed. This is also reflected in the apparent smoother sample surface of the BHO-doped films (cf. Figure 3.1.11). The EBSD measurements on the 500 nm films clearly show, that the average misorientation of grains is approximately the same for the pure and BHO-doped films (cf. Figure 3.1.20). The reduction of granularity can therefore not be attributed to a better texture, but rather to an enhanced microstructure, fueled by the reduction of porosity and the refinement of secondary phases in the superconducting film.

Last, σ_n is reduced with higher temperatures. A decrease of $\overline{\sigma_n}$ can be observed from 5 K to 77 K for all samples, as can be seen in Figure 3.1.21. In the 2 μm BHO-doped film, the decrease of granularity with increasing temperature is small, however, this sample exhibits the lowest magnetic granularity already at 5 K and the current flow seems to be impeded only at a few extremely bad grains (cf. Figure 3.1.14 upper panels). The 500 nm and 250 nm pure films also exhibit a negligible reduction of granularity from 5 K to 77 K, however, these two films exhibit the highest overall magnetic granularity. Here, the change in porosity from grain to grain seems to be the main limiting factor for current transport (cf. Figure 3.1.16). The influence of the pores is expected to be temperature independent, hence the granularity in these films is nearly temperature independent. In the other films, the suppression of currents seems to be dominated

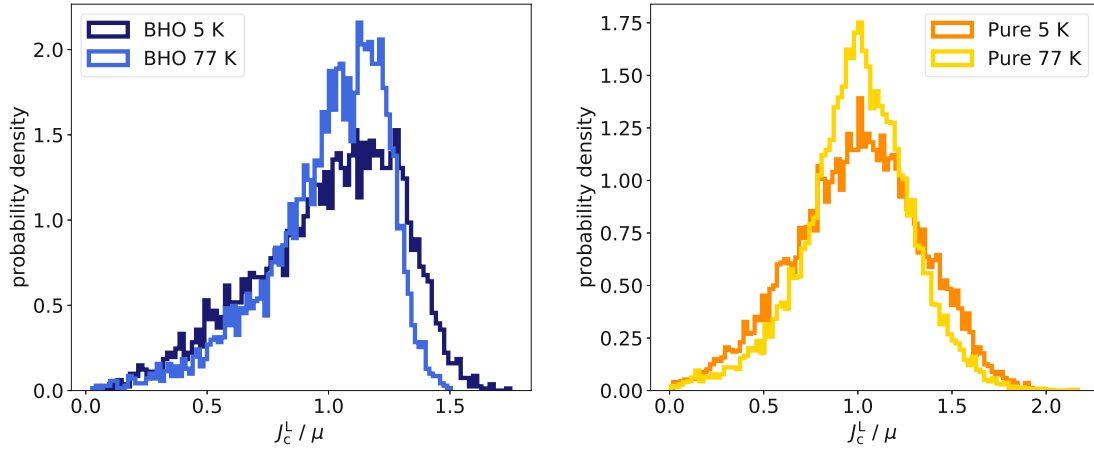


Figure 3.1.22: Comparison of the J_c^L distributions at 5 K and 77 K for one 500 nm BHO-doped spot (left panel) and one 2 μ m pure spot (right panel).

by weak-links, which can potentially depend on the temperature. The coherence length becomes larger with increasing temperature which leads to better coupling. At the same time, pinning weakens with increasing temperature due to the enhanced thermal activation of vortices which leads to a relatively smaller J_c^L in well-connected areas. In the case of the pure films, the J_c^L distributions remain nearly symmetric but become narrower at 77 K, as is exemplarily shown for one 2 μ m pure spot in the right panel of Figure 3.1.22. In the BHO-doped samples the peak shifts closer to the high- J_c^L end of the distribution and the asymmetry increases, i.e. the distribution approaches the ideal one, which is a narrow peak at high- J_c^L values, as shown in the left panel of Figure 3.1.22.

Another aspect for the influence of granularity and its change with temperature can be observed when comparing the films on RABiTS and IBAD-MgO based templates. At 5 K, the BHO-doped film on IBAD-MgO slightly outperforms the films on RABiTS and the difference in performance is even higher for the pure YBCO films (cf. Figure 3.1.2). At 77 K however, where the granularity of the RABiTS based films is reduced, the films on IBAD-MgO have lost all advantage and are outperformed by most films on RABiTS. While it is not possible to resolve the granularity for the films on IBAD-MgO, the distributions in Figure 3.1.10 clearly show, how the average local critical current density decreases faster at higher temperatures for the IBAD-MgO based films. At 77 K, the peaks of the films on IBAD-MgO are shifted to lower values for both

the BHO-doped and pure YBCO films as compared to those of the respective films on RABiTS.

A comparison of the global and local critical currents shows, that the absolute J_c^G values given in Table 3.1 are significantly lower than the corresponding mean J_c^L values given in Table 3.2. On the one hand, the SHPM samples exhibit a much smaller self-field which certainly contributes to this difference and it is expected from percolation theory, that the macroscopic critical current density is far below the average local critical current density [84, 85]. On the other hand, the magnetic signal of the Ni-9at.%W substrate could potentially influence both the SHPM and SQUID data. The absolute values therefore have to be considered with care, although the highest J_c^L in the 77 K distributions (cf. Figure 3.1.6(c)) agree well with experiments on single crystalline substrates [83]. This shows the potential for further optimization of RABiTS based conductors, even more so, since J_c^L in the IBAD-MgO based films do not reach such high values (cf. Figure 3.1.10). A potential explanation could be, that the resolution of the micro Hall scanner finds more or less macroscopic values of J_c because the granularity is on a much smaller length scale in the IBAD-MgO based templates. However, such tapes often exhibit a small tilt of the ab -planes [86] which may lead to imperfect growth and therefore smaller local current densities.

3.2 Fe(Se,Te)

Superconducting Fe(Se,Te) (FST) films were prepared on different metallic templates and single crystalline substrates by pulsed laser deposition, as described in chapter 2.1. The following sections give an overview of the experimental results, obtained through magnetization measurements and electron microscopy, as well as a discussion on the prospects of FST films on technical templates. The majority of these results were published in [65, 87].

3.2.1 Experimental Results

The superconducting properties and microstructure of four samples on technical templates and two samples on single crystalline substrates are presented in this section. The thicknesses, different buffer layers and substrate architectures of the FST films are summarized in Table 3.3. Sample #1 is a 320 nm FST film on a commercial Ni-5at.%W tape with a buffer layer of

sample	thickness	buffer layers	substrate
#1	320 nm	CeO ₂ /La ₂ Zr ₂ O ₇	RABiTS - Ni-5at.%W
#2	280 nm	Y ₂ O ₃	RABiTS - Ni-9at.%W
#3	580 nm	Y ₂ O ₃	RABiTS - Ni-9at.%W
#4	520 nm	Gd:CeO ₂ /LMO/MgO/Al ₂ O ₃	IBAD-MgO - Hastelloy
#5	200 nm	-	CaF ₂
#6	250 nm	-	MgO

Table 3.3: Thickness, buffer layers and respective substrate architectures of the investigated Fe(Se,Te) films.

CeO₂/La₂Zr₂O₇ (LZO) (provided by Deutsche Nanoschicht GmbH). Samples #2 and #3 are FST films deposited on a Ni-9at.%W tape with a single buffer layer of Y₂O₃ with superconducting film thicknesses of 280 nm and 580 nm, respectively. Sample #4 is a 520 nm FST film on Hastelloy with an IBAD-MgO based buffer architecture (provided by S-Innovations). Samples #5 and #6 are 200 nm and 250 nm films deposited on single crystalline substrates, namely CaF₂ and MgO, respectively.

3.2.1.1 Superconducting Properties

The critical temperature, T_c , of the four FST films on technical templates and the two FST films on single crystalline substrates, obtained by AC susceptibility measurements with a frequency of 30 Hz and an amplitude of 0.1 μ T, is presented in Figure 3.2.1. The T_c curves of the 280 nm thick film with a single Y₂O₃ buffer layer (sample #2) and the respective film with the thicker double buffer architecture (sample #1) show a similar trend, but also exhibit the lowest T_c of 14 K – 15 K of all samples. A slightly higher $T_c \sim 16$ K can be observed for the two films on RABiTS (sample #3) and IBAD-MgO (sample #4) with thicknesses 580 nm and 520 nm, respectively. For comparison, the two films on single crystalline substrates exhibit an even higher T_c , with a maximum $T_c = 19$ K, reached by the film on CaF₂. While the films on RABiTS templates all show a similar broad transition regardless of their buffer layers and thickness, the FST film which was deposited on an IBAD-MgO based substrate exhibits a sharp transition into the superconducting phase, indicating a more homogeneous distribution of the superconducting properties.

Figure 3.2.2 shows the field dependence of the global critical current density J_c^G of all samples

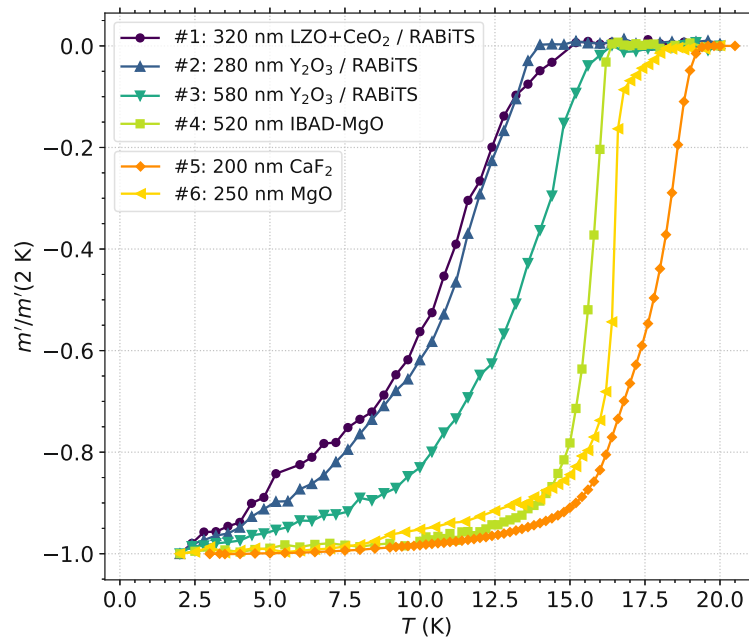


Figure 3.2.1: Temperature dependence of the normalized real part of the AC susceptibility of FST films on technical templates such as RABiTS (#1 – #3) and IBAD-MgO (#4) as well as single crystalline substrates (#5 – #6).

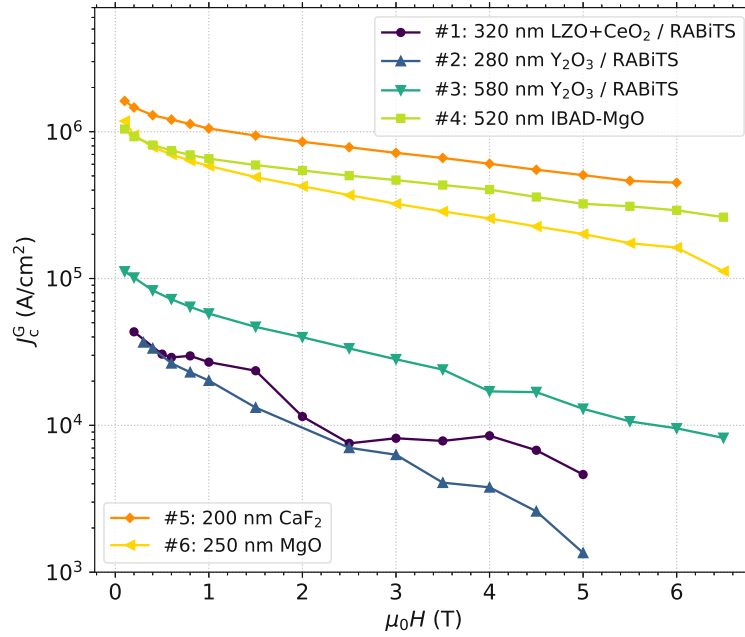


Figure 3.2.2: Field dependence of the global critical current density J_c^G at 5 K. On RABiTS, J_c^G is similar for samples with one or two buffer layers, while it is one order of magnitude higher for films on IBAD-MgO and single crystalline substrates.

at 5 K. Sample #1 and #2 exhibit a similar trend with the lowest J_c^G . The variation in the measured values stem from a low signal-to-noise ratio of the magnetization loop. Sample #3, which has a higher film thickness, performs better at all measured fields. When considering J_c^G , the films on IBAD-MgO and on single crystalline substrates show a similar trend but with self-field values above 1 MA/cm², which is an order of magnitude higher than the best performing film on RABiTS. The temperature dependence of J_c^G of samples #3 – #6 is shown in more detail in Figure 3.2.3. While the films on IBAD-MgO and CaF₂ show a similar field dependence for all temperatures between 2 K and 10 K, sample #6 on the MgO substrate exhibits similarly high self-field values, however, J_c^G decreases faster with increasing field. The same field dependence, but with an order of magnitude lower values, can be observed for the 580 nm film on RABiTS.

Round spots where chemically etched on samples #1 – #5, their remnant field profiles at 5 K with a spatial resolution of 7 μm are shown in Figure 3.2.4. The FST films on RABiTS (samples #1 – #3) appear granular, while the films on IBAD-MgO (#4) and CaF₂ (#5) exhibit more homogeneous Bean profiles, the latter however with two extended disturbances. Sample

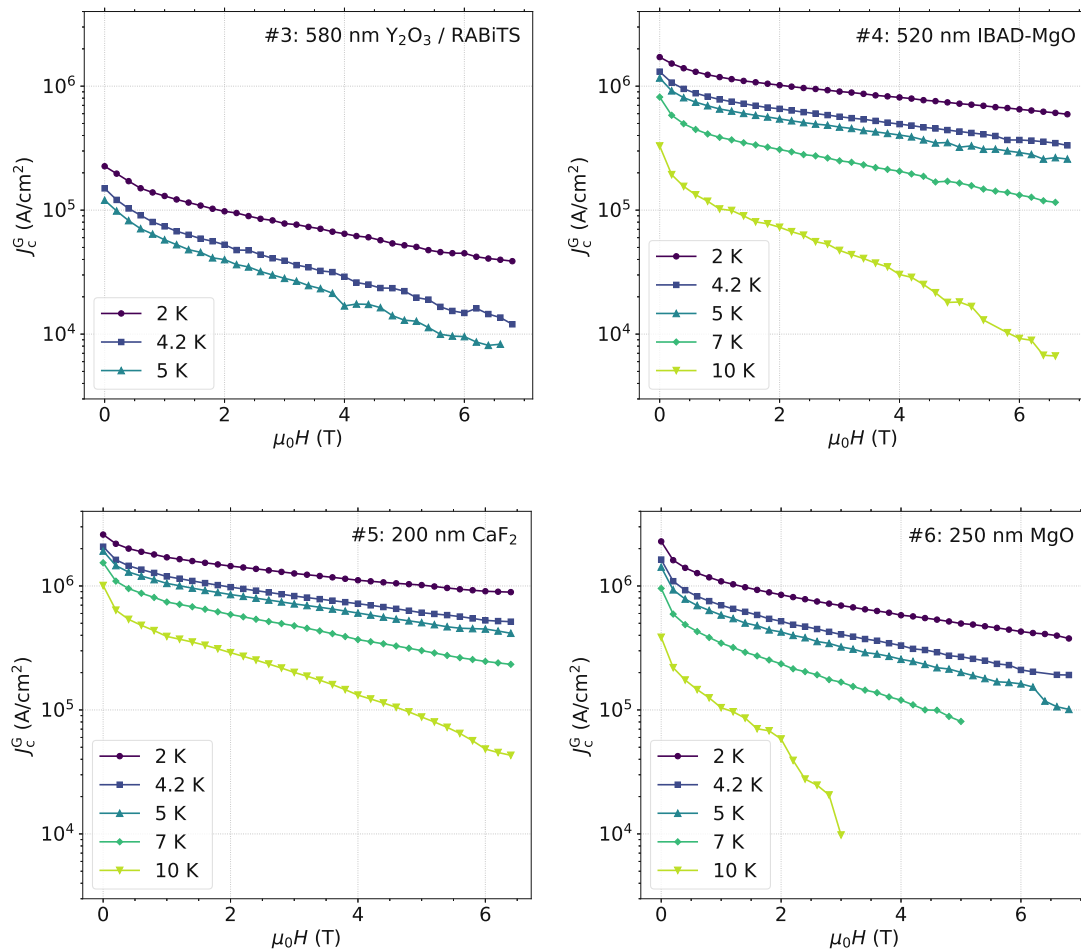


Figure 3.2.3: Field dependence of J_c^G of FST films on RABiTS, IBAD-MgO, CaF₂ and MgO substrates at various temperatures.

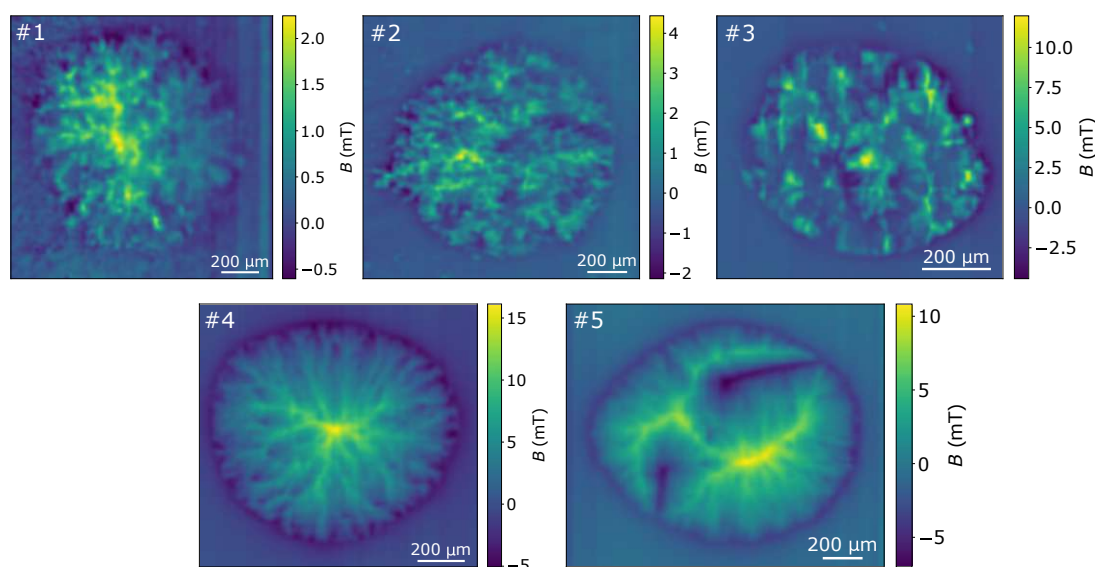


Figure 3.2.4: Remnant field profiles at 5 K with a spatial resolution of 7 μm . The field profiles of the films on RABiTS appear granular (#1 – #3), regardless of their thickness or buffer layer architecture. The films on IBAD-MgO (#4) and CaF_2 (#5) exhibit more homogeneous Bean profiles.

#1 has a small signal in the Hall scan with a maximum remnant field of only 2 mT. The signal-to-noise ratio is not good enough to clearly resolve the borders of the round spot. The respective FST film with a single Y_2O_3 buffer layer (#2) exhibits grain clusters with remnant fields up to 4 mT. With this sample, the borders of the etched spot can clearly be distinguished from the background of the RABiTS substrate. This shows, that on a local scale, the sample with only one buffer layer retains a higher trapped field in some grain clusters than the sample with comparable thickness and double buffer architecture. Sample #3 exhibits grain clusters with a maximum remnant field of 12 mT. However, large areas which appear to have the same shape as the underlying Ni-W grains exhibit no superconducting signal.

The remnant field profiles of samples #4 and #5 are more homogeneous. Some minor disturbances in the Bean profile of the sample on IBAD-MgO can be attributed to small holes in the superconducting film, which can be seen in a digital light microscope image (see left panel in Figure 3.2.5). These were most likely caused by small particles covering the substrate during the deposition process. Two clearly distinguishable micro cracks are responsible for the disturbance in the otherwise homogeneous Bean profile of sample #5 (see right panel in Figure 3.2.5).



Figure 3.2.5: Digital light microscope images of the FST films on IBAD-MgO and CaF₂. Small holes can be found in the superconducting film on IBAD-MgO, indicated by white arrows (left panel). Micro cracks can be detected in the FST film on CaF₂ (right panel).

The local critical current density J_c^L maps of sample #3 on RABiTS and sample #4 on IBAD-MgO, which were calculated from their trapped field profiles, are presented in Figure 3.2.6. The J_c^L map of sample #4 is mostly homogeneous with an estimated average local critical current density of 2 MA/cm². The minor disturbances in the current flow are caused by the small holes in the superconducting film (shown in the right panel of Figure 3.2.5). Sample #3 shows similar, or in some places even higher J_c^L values, however, some other areas lack current flow. Due to the granular nature of the underlying Ni-W grains, the supercurrents flow in and across some grains but avoid other grain clusters completely.

For the quantification of granularity, the statistical analysis described in Section 2.2.4 was employed for sample #3 and #4. Figure 3.2.7 shows the J_c^L distributions for both samples in a histogram plot. The film on RABiTS exhibits a much broader distribution, with many values close to zero, which represent the grain clusters with little current flow. The reduced granularity in the film on IBAD-MgO is indicated by a sharper peak in the J_c^L distribution. The FST film on IBAD-MgO exhibits a mean J_c^L value of $\mu = 1.54$ MA/cm² with a relative standard deviation $\sigma_n = \sigma/\mu = 20$ %, while $\mu = 0.75$ MA/cm² and $\sigma_n = 74$ % for the film on RABiTS. The largest observed local current densities are similar in both films.

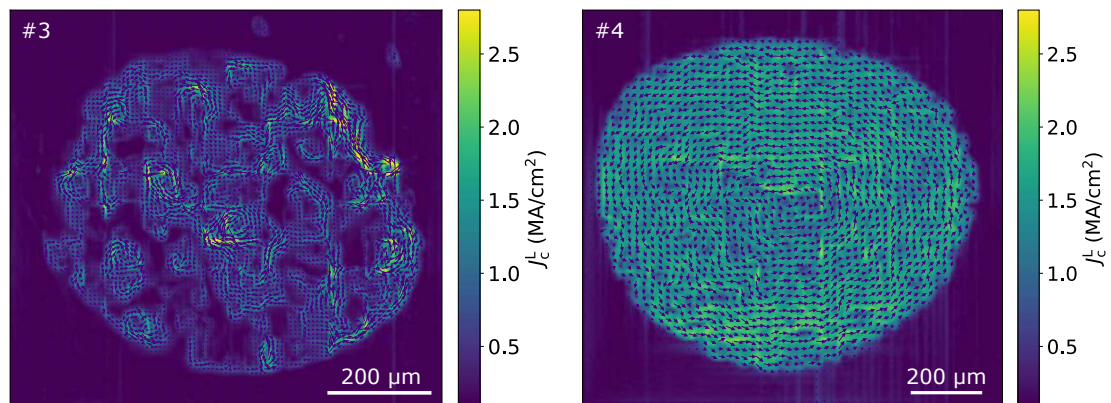


Figure 3.2.6: Local critical current density J_c^L of sample #3 on RABiTS (left panel) and sample #4 on IBAD-MgO (right panel). The granular nature of the RABiTS template can clearly be resolved.

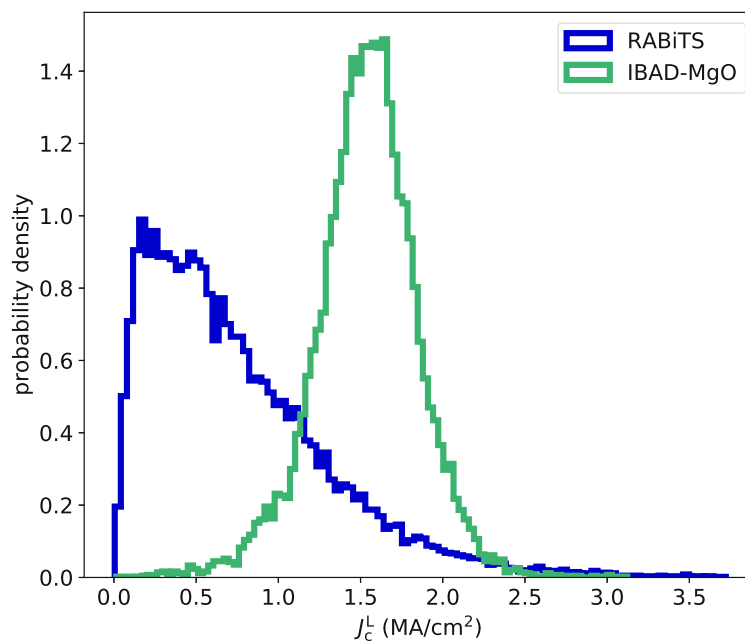


Figure 3.2.7: J_c^L distributions of the FST films on RABiTS (sample #3) and IBAD-MgO (sample #4). The reduced granularity for sample #4 is represented by a sharper peak.

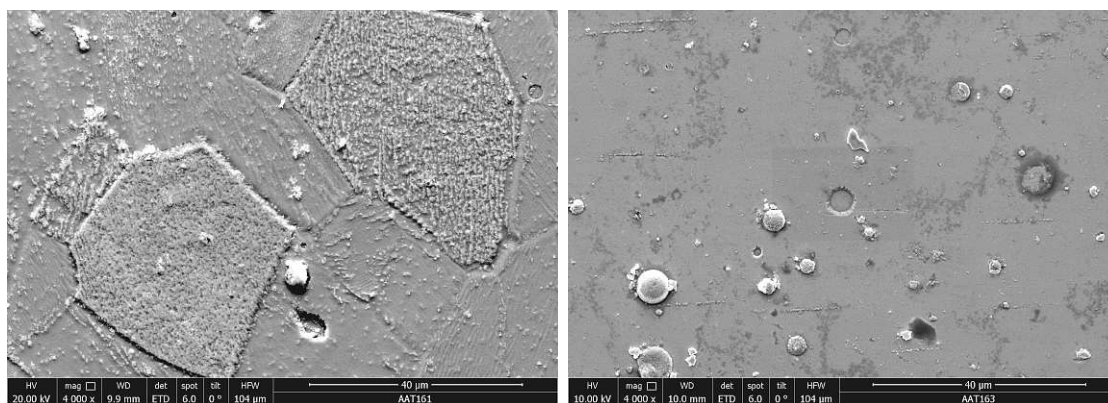


Figure 3.2.8: SEM images of the surface morphology of sample #3 on RABiTS (left panel) and sample #4 on IBAD-MgO (right panel). The granular structure of the underlying Ni-W grains is clearly visible for the FST film on RABiTS.

3.2.1.2 Microstructure

The difference in microstructure between sample #3 on RABiTS and sample #4 on IBAD-MgO becomes immediately apparent when studying the surface morphology on both samples. The left panel in Figure 3.2.8 shows a SEM image of the superconducting layer on RABiTS, the underlying Ni-W grain structure with grain sizes of 20 μm – 50 μm is clearly visible. It can be seen, that the surface morphology of the superconductor varies from grain to grain. While some grains exhibit a smooth surface, others show a tilted terrace structure. The film on IBAD-MgO, however, exhibits a mostly homogeneous surface with only some secondary phase precipitates visible on the surface, as can be seen in the right panel of Figure 3.2.8.

The grain structure of the underlying Ni-W grains of sample #3 on RABiTS can also be observed with a digital light microscope. When looking at the superconducting film on top, some grains appear darker than others, see Figure 3.2.9(a). By using a polarization filter, the different surface morphology of these grains becomes apparent, as they appear with higher contrast than the rest, as can be seen in (b). An overlay of the J_c^L map with the light microscope image shows, that the supercurrents do not flow in these darker grains but meander through the brighter grains, see Figure 3.2.9(c). The black rectangle indicates the area that was chosen for the preparation of a TEM lamella.

The SEM image in Figure 3.2.10 shows the area where a TEM lamella was prepared across a grain boundary, indicated by the black bar. The white arrows on top show the current flow in

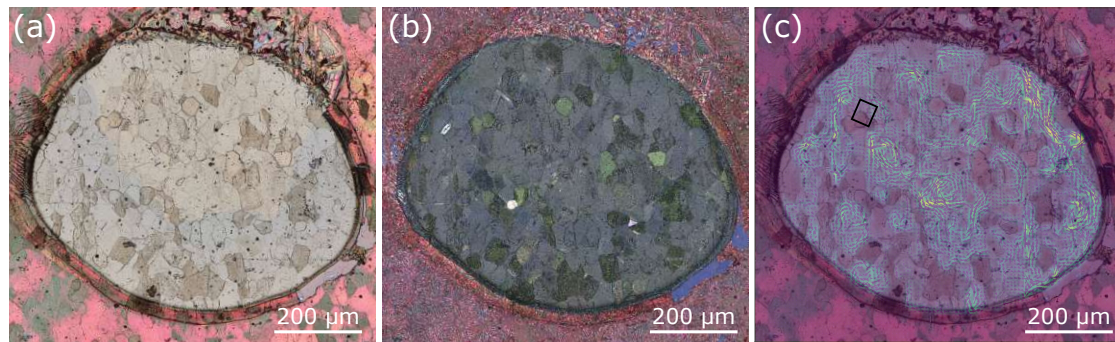


Figure 3.2.9: Digital light microscope image of the round spot of sample #3 on RABiTS. Some grains appear darker than others (a). These grains appear with higher contrast when using a polarization filter (b). An overlay with the J_c^L map shows, that no current flows in the darker grains (c). The small black rectangle indicates the area that was chosen for the preparation of a TEM lamella.

this area. The right side of the lamella exhibits a grain with smooth surface and good current flow. The left side of the lamella exhibits a dark grain with a rough surface structure and no current flow (indicated by white dots instead of arrows).

A TEM bright field image gives an overview of the superconducting layer, buffer layer and substrate in the grain boundary region, as can be seen in Figure 3.2.11(a). The GB in the substrate is marked by white horizontal arrows. On the left side of the GB, the FST layer exhibits regions of different contrast which can be associated with many grains. This behavior starts about $1 \mu\text{m}$ right of the GB, while further to the right, the superconducting layer appears smooth with a thickness of 580 nm . The different appearance of the superconducting layer on both sides of the GB can be better visualized by means of TEM dark field (DF) imaging. Two different DF images can be produced from an area on the left side of the GB (indicated by the left rectangle in Figure 3.2.11(a)), as can be seen in Figures 3.2.11(b) and (c). The images are produced by selecting individual diffraction points in the diffraction pattern, that stem from different areas in the superconducting layer. Since different grains appear bright in (b) and (c) it can be assumed that the FST layer exhibits many grains with varying grain orientations. On the right side of the GB, the DF image yields the same result for all diffraction points, which indicates a homogeneous FST layer, as can be seen in Figure 3.2.11(d).

The diffraction pattern from a selected area in the substrate GB shows two tilted lines of diffraction points that indicate the out-of-plane orientation of the substrate on both sides of the

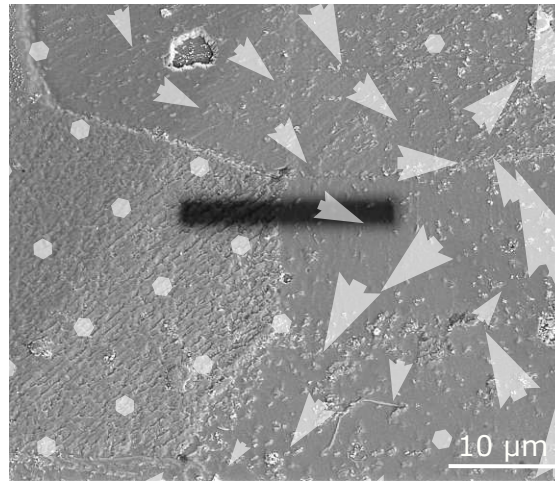


Figure 3.2.10: SEM image of a grain boundary between a grain with good current flow (white arrows) and a grain with no current flow (white dots). The black bar indicates the area where a TEM lamella was prepared across the GB.

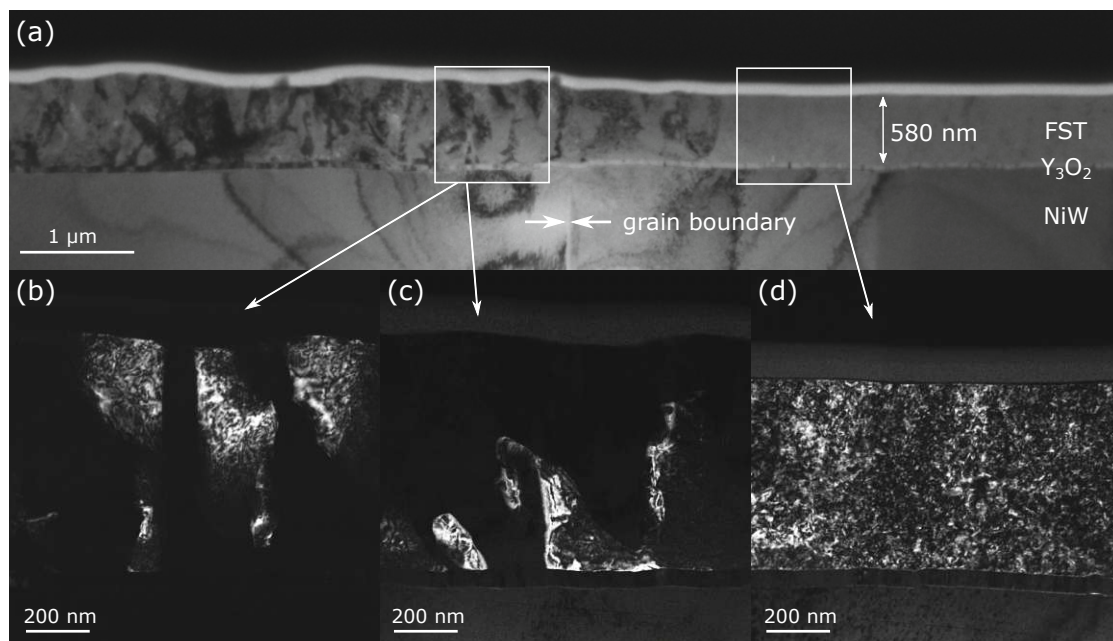


Figure 3.2.11: TEM images of the FST layer, Y_2O_3 buffer layer and Ni-W substrate in the GB region. Overview of the lamella with a film thickness if 580 nm in the smooth area on the right side of the GB (a). Dark field images indicate different grain orientations on the left side of the GB (b) and (c), and a homogeneous layer on the right side of the GB (d).

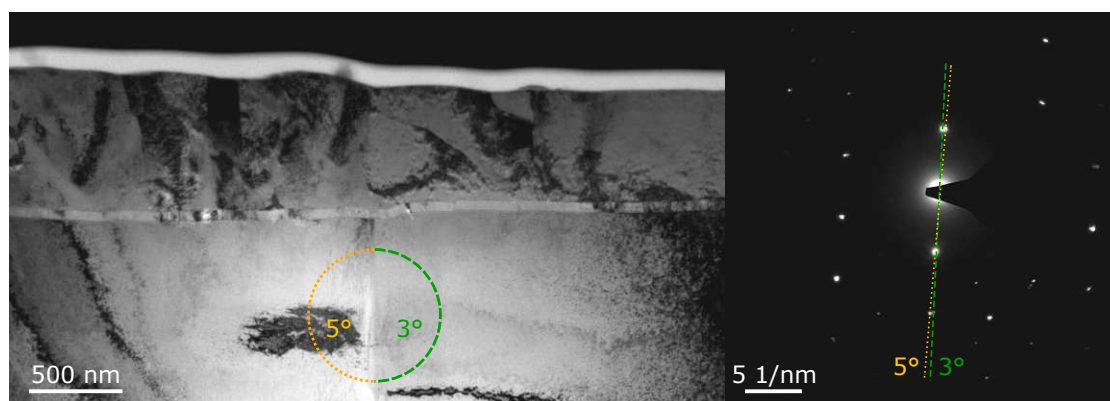


Figure 3.2.12: Diffraction pattern of the substrate grain boundary. Two lines of diffraction points are tilted by 3° (green dashed line) and 5° (yellow dotted line) with respect to the vertical, which corresponds to the out-of-plane tilt on the right and left side of the GB, respectively.

GB, see Figure 3.2.12. One line of diffraction points is tilted by 3° with respect to the vertical (green dashed line) which corresponds to the out-of-plane tilt on the right side of the GB. The other line of diffraction points exhibits a tilt of 5° with respect to the vertical (yellow dotted line) which corresponds to the out-of-plane tilt on the left side of the GB. The two Ni-W grains in the substrate therefore have a grain boundary with an overall GB out-of-plane tilt of 2° .

In order to further investigate grain orientations in the FST layer, transmission Kikuchi diffraction (TKD) patterns of the same lamella were recorded. The upper panel in Figure 3.2.13 shows the TKD map colored according to the inverse pole figure (IPF) 100, which indicates the crystal orientations in z -direction, i.e. normal to the film surface. The angles indicate the deviation of the c -axis of the FST film and substrate from the surface normal, i.e. the out-of-plane tilt of grains. On the right side of the GB (indicated by black horizontal arrows), the substrate exhibits an out-of-plane tilt of $2^\circ - 3^\circ$, which is transferred to the superconducting layer that exhibits a similar tilt (everything is red in the TKD map for IPF 100). On the left side of the GB, however, the substrate has an out-of-plane tilt of $4^\circ - 5^\circ$ which seems to cause a severe disturbance in the FST layer, where individual grains can be observed, some with an out-of-plane tilt of 55° and more (yellow grains). The lower panel in Figure 3.2.13 shows the TKD map colored according to the IPF 001, which gives the crystal orientations in the ab -plane. The angles indicate the deviation of the a -axis with respect to the surface horizontal, i.e. the in-plane orientation of grains. While on the right side of the GB, the FST layer appears homogeneous

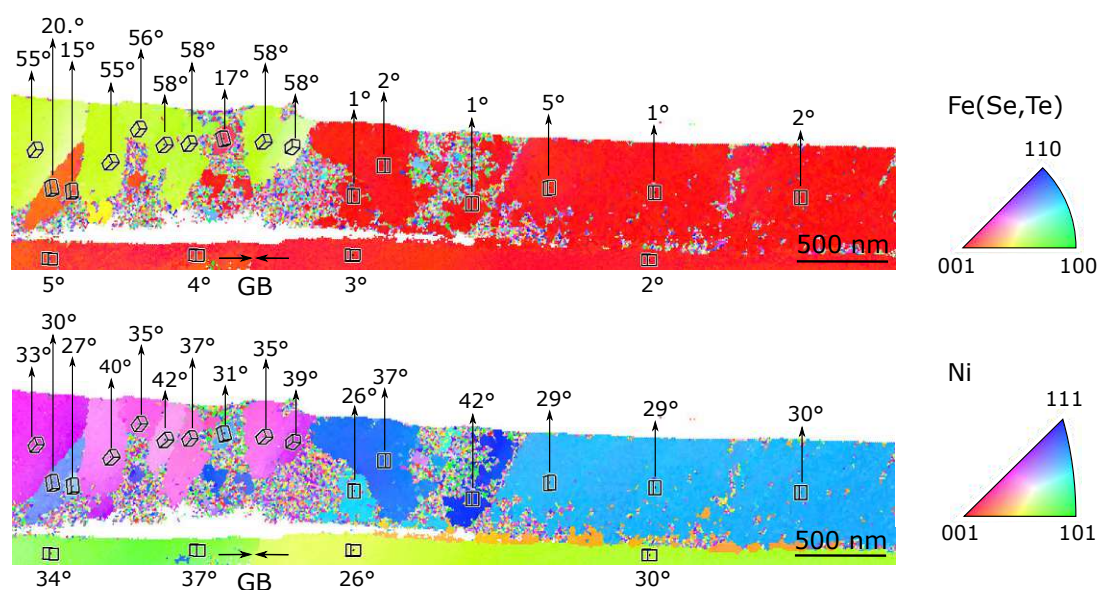


Figure 3.2.13: TKD maps of the TEM lamella of sample #3 on RABiTS. In the TKD map for IPF 100 (upper panel), the given angles refer to the deviation of the c -axis with respect to the surface normal (out-of-plane orientation). In the TKD map for IPF 001 (lower panel), the angles refer to the deviation of the a -axis with respect to the surface horizontal (in-plane orientation).

(colored in blue), the left side shows how individual grains in the FST layer exhibit various in-plane rotations in addition to their out-of-plane-tilt.

3.2.2 Discussion

For the development of cheap coated conductors, iron-based superconductors (IBS) are a subject of great interest. Compared to the cuprates, the texture requirement seems relaxed because iron based superconductors allow for higher misorientation angles between neighboring grains before the critical current across a GB is heavily suppressed [44, 47, 48]. The use of RABiTS templates with simple buffer layer architectures is comparably cheap but the resulting superconducting properties are usually not as good as in films deposited on single crystalline substrates or IBAD-MgO based templates [60, 63, 88]. The relaxed texture requirement of IBS could therefore enable the use of simple RABiTS templates.

In this study, Y_2O_3 was chosen as a single buffer layer on RABiTS to act as a diffusion barrier that prevents nickel poisoning of the superconductor. The lattice misfit is small, as Y_2O_3 has

a lattice parameter of 10.6 Å, with 1/4 of the diagonal being 3.75 Å, which matches well with the a -axis lattice parameter of FST of 3.76 Å. Other studies used CeO₂ as a single buffer layer, which yielded similar results [57].

The global magnetization measurements in Figures 3.2.1 and 3.2.2 show, that the superconducting properties are more or less the same when comparing the FST film with a single Y₂O₃ buffer layer and the respective sample with the double buffer architecture. Both T_c and J_c^G increase with higher film thickness, nevertheless, the films on RABiTS still cannot compete with the films on IBAD-MgO and single crystalline substrates. Figure 3.2.6 shows, that the film on RABiTS forms magnetic grain clusters consisting of well aligned physical grains that exceed local current densities of 2 MA/cm². A similar behavior was found for PLD-grown YBCO films on RABiTS templates, where the microstructure of the superconducting film is severely influenced by the alignment of the underlying Ni-W grains [60, 63]. In order to understand what causes the formation of magnetic grain clusters in the FST film on RABiTS, the Y₂O₃ buffer layer needs to be studied more closely. Since it was not possible to highlight the role of the buffer layer in the TKD maps, Figure 3.2.14 shows a SEM image of the Y₂O₃ layer on the Ni-W substrate (upper panel) and a TEM image of the buffer layer in the GB region (lower panel) with good current flow on the right side of the GB and no current flow on the left side of the GB. The thin Y₂O₃ layer exactly replicates the underlying Ni-W grain structure with surface facets according to the out-of-plane tilt of the metal tape. On Ni-W grains with small out-of-plane tilts the Y₂O₃ layer exhibits large terraces with a (001) oriented surface (green solid lines) and small steps (yellow dotted lines) in between. This situation can be found on the right side of the GB in the TEM image (lower panel in Figure 3.2.14). Slightly larger out-of-of plane tilts in the substrate lead to short terraces with large steps in between that do not exhibit a (001) orientation, which can be found on the left side of the GB. The nucleation of the FST layer is severely influenced by the faceted surface of each substrate grain, causing some grains to appear darker in a digital light microscope, as can be seen in Figure 3.2.9(a). The SEM image in Figure 3.2.10 shows, that these darker grains that have no current flow exhibit a rough film surface. The TEM images and TKD study revealed that an out-of-plane tilt of only 4° – 5° of the underlying Ni-W grain causes a severe disturbance in the FST layer consisting of many misoriented grains. So far, it is not clear, whether optimized deposition conditions could reduce the formation of misoriented

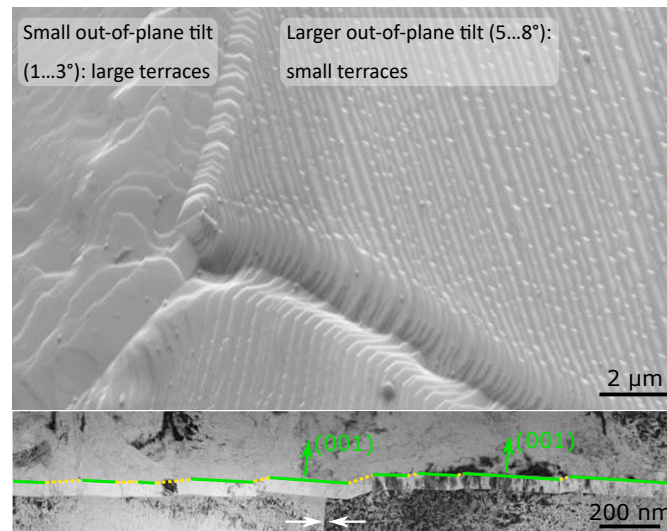


Figure 3.2.14: SEM image of the Y_2O_3 buffer layer (upper panel, *credits: Ilya Shipulin*). On grains with small out-of-plane tilts the Y_2O_3 layer exhibits large terraces, while on grains with slightly larger out-of-plane tilts the layer exhibits short terraces. TEM image of the GB region (lower panel). On the right side of the GB, large terraces with (001) orientation (green solid lines) can be observed. On the left side of the GB, shorter terraces with (001) orientation can be found with larger steps in between that exhibit a different orientation (yellow dotted lines).

superconducting grains on tilted Ni-W grains.

In order to directly compare the magnetic granularity of FST films and YBCO films, Figure 3.2.15 shows the J_c^L distributions at 5 K of both materials. The J_c^L values are normalized to their mean value, since the current densities of the FST films are more than one order of magnitude lower. The J_c^L distributions of the FST films are calculated from the 580 nm film on RABiTS (sample #3) and the 520 nm film on IBAD-MgO (sample #4) (cf. Figure 3.2.7), while the J_c^L distributions of the YBCO films are calculated from the 500 nm BHO-doped and pure films on RABiTS and IBAD-MgO. The FST film on RABiTS shows an extremely broad distribution, indicating an even higher granularity than in the YBCO films. In the case of the IBAD-MgO based template, the FST film also shows a broader distribution compared to the YBCO film. Since the grains in this type of template cannot be resolved by the micro Hall scanner, the broader peak can only indicate a less homogeneous distribution of the superconducting properties.

Even though the FST film on RABiTS exhibits some grain clusters with high current densities, the PLD-growth still requires a high degree of substrate grain alignment, especially when it comes

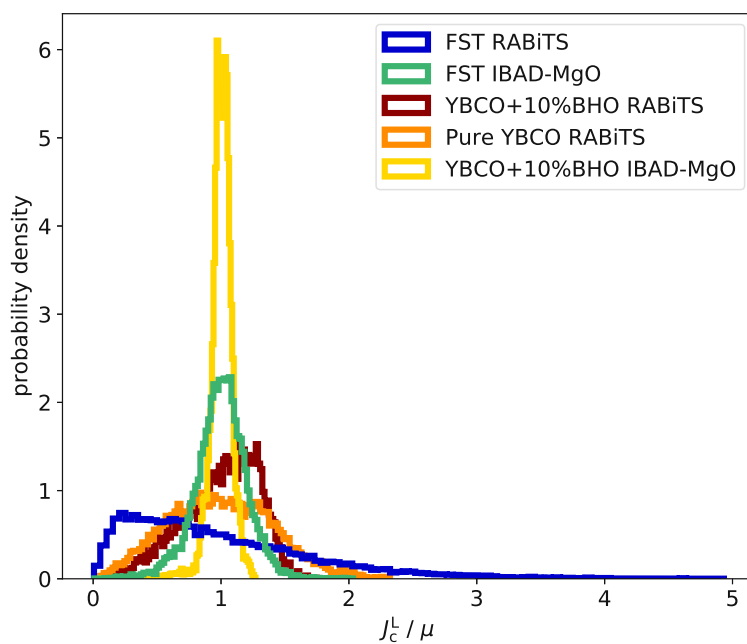


Figure 3.2.15: J_c^L distributions of the FST films on RABiTS (sample #3) and IBAD-MgO (sample #4) compared to the J_c distributions of the 500 nm BHO-doped and pure YBCO films on RABiTS and IBAD-MgO at 5 K. For better comparison, the J_c^L values are normalized to their mean values μ .

to the out-of-plane orientation. It seems that, if the individual Ni-W grains exhibit out-of-plane misalignments of more than 3° , the superconducting properties cannot benefit from the relaxed requirements for the GB misorientation angles of IBS.

3.3 Tl-1223

Superconducting $\text{Tl}(\text{Bi,Pb})\text{Sr}(\text{Ba})_2\text{Ca}_2\text{Cu}_3\text{O}_{9+x}$ (Tl-1223) films were prepared on textured Ag ribbons and single crystalline substrates by electrochemical deposition, as described in chapter 2.1. The following sections give an overview of the experimental results, many of which were published in [40].

3.3.1 Experimental Results

During the research for this thesis many thallium-based films on single crystalline and silver substrates were investigated, the results of the two most promising samples are presented here. One sample is a Tl-1223 film deposited on a textured Ag ribbon [72], while the other film was deposited on a SrTiO_3 (STO) single crystalline substrate. Both superconducting films were deposited as round spots with 1 cm diameter and a nominal thickness of about 2 μm .

3.3.1.1 Superconducting Properties

A 4 mm \times 4 mm sample was cut from the thallium-based sample on Ag substrate in order to measure the superconducting transition temperature by means of AC susceptibility in the SQUID magnetometer. A frequency of 1 Hz and an amplitude of 30 μT was chosen, the measured curve is presented in Figure 3.3.1. Two transitions into the superconducting phase can be identified. The first, with an onset temperature of $T_c = 107$ K corresponds to the Tl-1223 phase, while the second transition with $T_c = 75$ K can be attributed to the Tl-1212 phase.

The superconducting film was chemically etched off the Ag substrate with hydrochloric acid such that a round spot of unharmed film remained. The corresponding remnant field profile at 5 K with a spatial resolution of 11 μm is shown in Figure 3.3.2(a). The area scan shows many individual grains and grain clusters with trapped fields up to 30 mT. In order to further

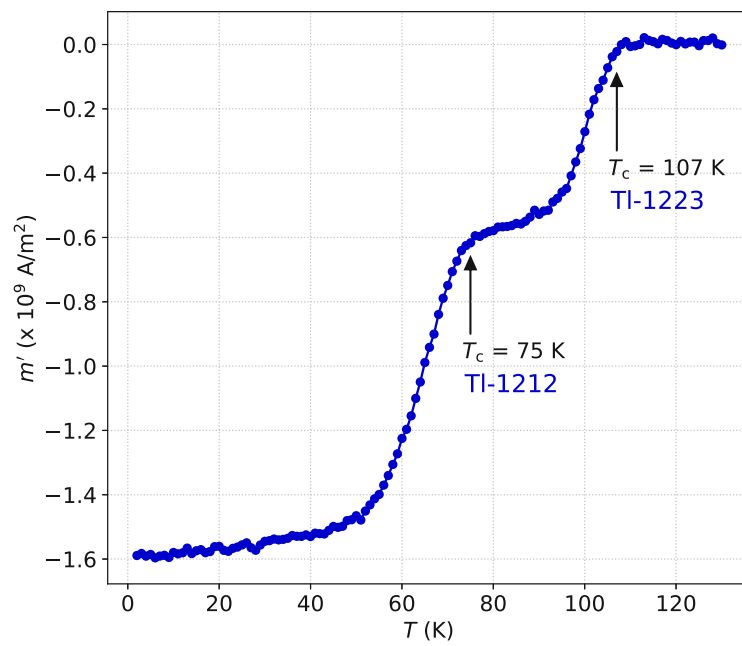


Figure 3.3.1: AC susceptibility of a thallium-based film on Ag substrate. Two transitions into the superconducting phase are identified at approximately 107 K and 75 K, which correspond to the Tl-1223 and Tl-1212 phase, respectively.

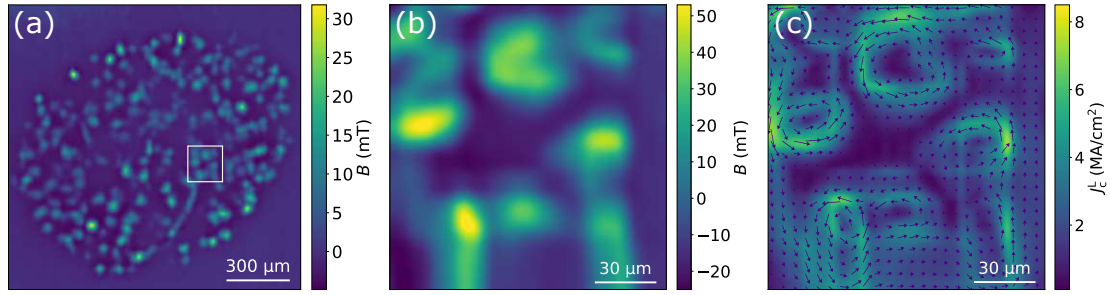


Figure 3.3.2: Hall scans of the TI-based sample on Ag substrate at 5 K. (a) Remnant field profile of the entire etched spot. (b) High-resolution scan of a few grains and grain clusters. (c) J_c^L map of the same grain clusters.

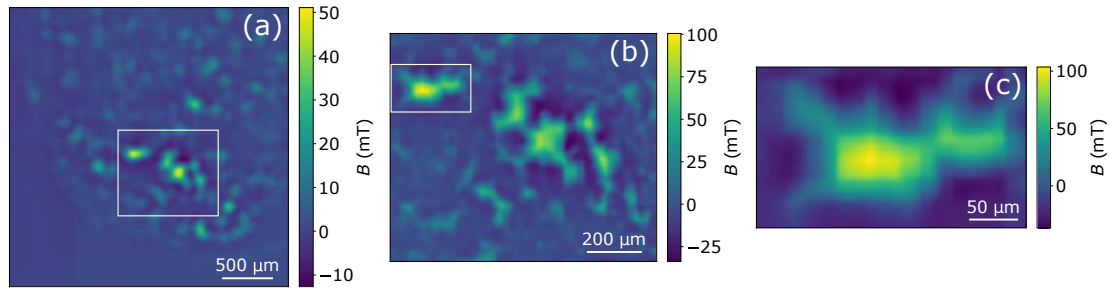


Figure 3.3.3: Hall scans of the TI-based sample on STO substrate at 5 K with spatial resolutions of 28 μm (a), 6 μm (b) and 3 μm (c).

investigate the currents in grains and across grain boundaries, a small area was chosen for a high-resolution scan (indicated by the white rectangle). Figure 3.3.2(b) shows the area of a few grains with a spatial resolution of 3 μm , where trapped fields of about 50 mT can be found. The J_c^L map of this area, shown in (c), reveals that the currents can pass from individual grains to other grains and shows that the local current density in these grain clusters amounts to $J_c^L = 8 \text{ MA/cm}^2$ at 5 K.

The remnant field profiles of the TI-based film on STO substrate at 5 K are presented in Figure 3.3.3. In this case, the film was not etched, but a quarter of the 1 cm circular spot was scanned in the micro Hall scanner with a spatial resolution of 28 μm (as can be seen in (a)). The remnant field profile appears granular with grain clusters that exhibit trapped fields up to 50 mT. The white rectangle indicates an area that was chosen for a more precise scan with 6 μm resolution, shown in (b). Here it can be seen, that some grain clusters cover an area of 200 μm and more, with trapped fields of up to 100 mT. Figure 3.3.3(c) shows the remnant field map of

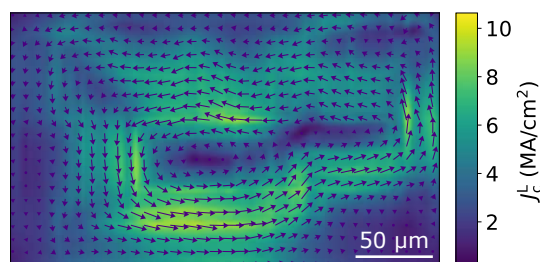


Figure 3.3.4: J_c^L map of a Tl-1223 grain cluster on STO substrate. Local current densities of up to 10 MA/cm^2 are found.

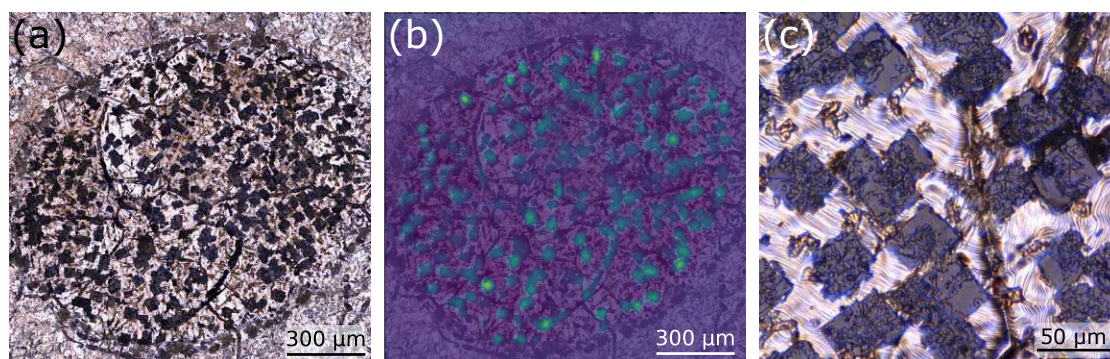


Figure 3.3.5: (a) Digital light microscope image of the Tl-1223 film on Ag substrate. (b) An overlay with the remnant field map shows perfect agreement of the magnetic and physical grains. (c) A high-resolution image reveals large plate-like superconducting grains.

the most prominent grain cluster with a spatial resolution of $3 \mu\text{m}$. The J_c^L map of this grain cluster reveals local current densities of up to 10 MA/cm^2 , as can be seen in Figure 3.3.4.

3.3.1.2 Microstructure

A digital light microscope image of the Tl-1223 film on the textured Ag ribbon shows many individual plate-like grains, as can be seen in Figure 3.3.5(a). The dark spots indicate the superconducting areas. An overlay with the remnant field map shows a perfect agreement between the dark spots in the optical image and the bright spots with high trapped field, shown in (b). A higher resolution image reveals large plate-like superconducting grains with a grain size of $30 \mu\text{m} - 40 \mu\text{m}$, seen in (c).

EDX analysis of this sample shows, that most large plate-like grains indeed exhibit the Tl-1223 phase and a contribution from the Tl-1212 phase is also detected, as can be seen in the elemental map in Figure 3.3.6. The platelets in green and blue represent the Tl-1223 and Tl-1212 phase,

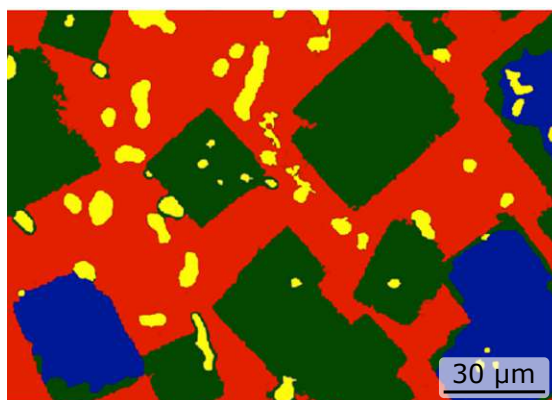


Figure 3.3.6: EDX phase map of the Tl-based film on Ag substrate. The plate-like grains exhibit the Tl-1223 phase (green) and the Tl-1212 phase (blue). Small secondary Ca,Pb-O phases (yellow) and the Ag substrate (red) are also identified. *Credits: Alice Moros, adapted from [40].*

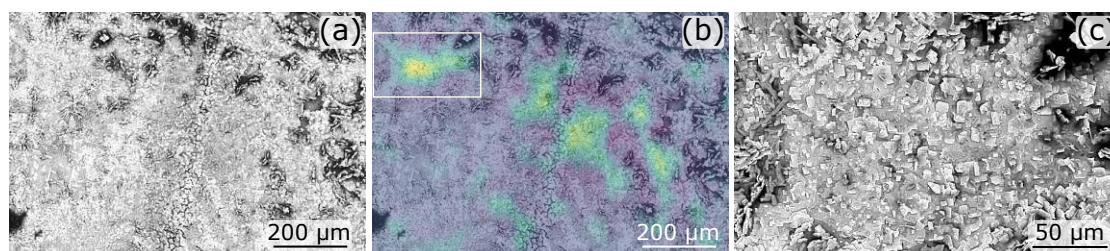


Figure 3.3.7: (a) SEM image of the Tl-based film on STO substrate. (b) Overlay with the corresponding remnant field map. (c) The area that exhibits the highest trapped field has well-aligned and well-connected grains.

respectively, while secondary Ca,Pb-O phases are colored in yellow. The large red area, which represents the Ag-substrate, shows that the superconducting grains are only loosely connected and the coverage of superconducting film is not high enough to form large grain clusters.

Figure 3.3.7(a) shows a SEM image of the Tl-based film on STO substrate. Although the superconducting film covers most of the substrate, it still appears quite inhomogeneous. An overlay with the respective remnant field map, shows that only some areas exhibit a magnetic signal, as can be seen in (b). The white rectangle indicates the area with the highest trapped field, the corresponding SEM image is shown in (c). This area exhibits a 150 μm wide area of well-aligned and well-connected grains. An overlay with the corresponding remnant field map can be found in Figure 3.3.8(a).

Two TEM lamellae were prepared, one from an area with high trapped field and one from an

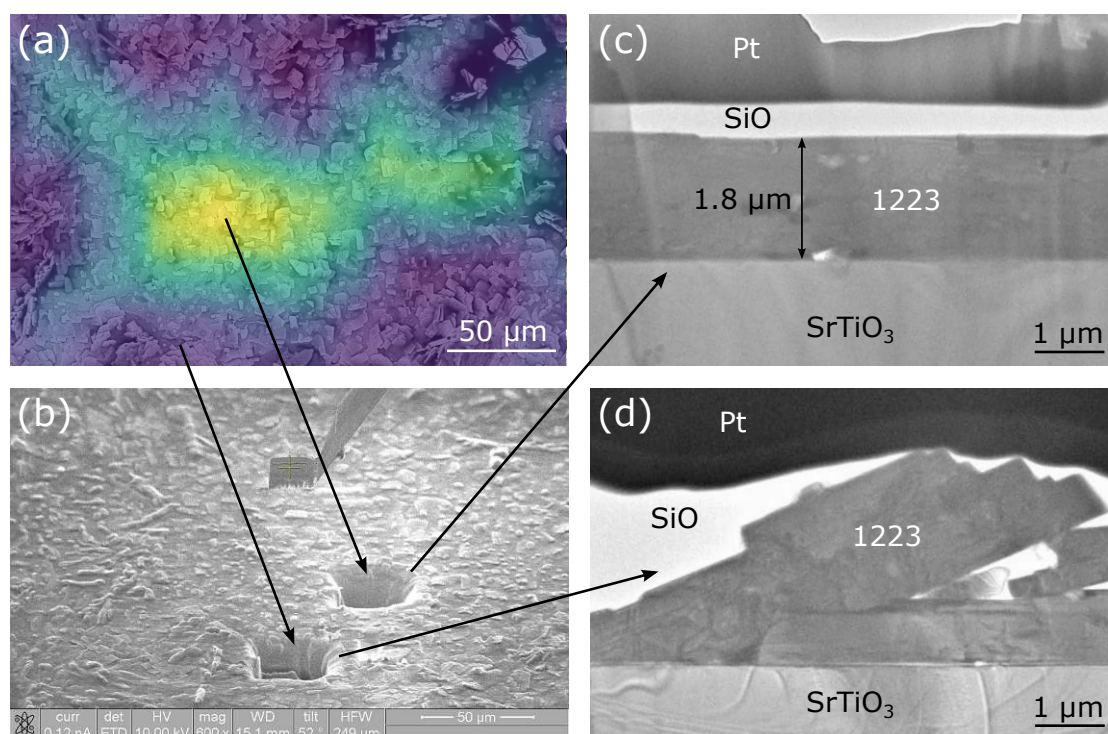


Figure 3.3.8: (a) Overlay of the remnant field map and the corresponding SEM image. (b) Two TEM lamellae were prepared: one from an area with high trapped field and one from an area with no trapped field. (c) TEM image of the lamella taken from an area with high trapped field. The superconducting layer exhibits one 1.8 μm thick Tl-1223 grain flat on the STO substrate. (d) TEM image of the lamella taken from an area with no trapped field. Multiple randomly oriented Tl-1223 grains can be identified.

area with no trapped field, as indicated by the arrows leading from Figure 3.3.8(a) to (b). The TEM image of the high trapped field area shows one large grain with a thickness of 1.8 μm flat on the substrate surface, seen in (c). With EDX analysis, the different areas of the lamella can be identified as the Pt protective layer on top, a thin SiO layer which stems from contamination in the fabrication process and a thick Tl-1223 grain on top of the STO substrate. The other lamella, which was taken from an area with no trapped field, exhibits the same compositions, however, multiple Tl-1223 grains can be found which are randomly oriented on the substrate surface, as can be seen in (d).

3.3.2 Discussion

The thallium-based cuprates, especially the Tl-1223 phase, could be an interesting alternative to other HTS compounds for various applications. They exhibit one of the highest known transition temperatures at ambient pressure and high upper critical fields, are still technologically unexploited and conductors have certainly not reached their full potential. However, due to the high volatility of thallium in the production process, the preparation of samples has proven to be more difficult than expected. While the detected high T_c of the Tl-1223 phase is promising, a better phase purity needs to be realized e.g. with further optimization of the heat treatment. In principle, high local current densities were detected on both Ag and STO substrates, however, this is limited to small areas of a few hundred micrometers. The comparison of the TEM lamellae from areas with high trapped field and no trapped field (cf. Figure 3.3.8) underlines the necessity for grain orientation also in this material class. Both SHPM measurements and SEM investigations on the microstructure show, that the films are far too inhomogeneous to be a viable option for any application at this stage.

Chapter 4

Conclusion and Outlook

The local and global current transport capabilities of three different high temperature superconducting materials were investigated by means of magnetization measurements with a SQUID magnetometer and two different high-resolution Hall scanners. Scanning and transmission electron microscopy analysis was performed on YBCO, Fe(Se,Te) and Tl-1223 thin films on technical templates in order to relate current flow in superconducting grains and across grain boundaries with microstructural features. Using local current maps, obtained by high-resolution scanning Hall probe microscopy, a quantitative statistical analysis of the magnetic granularity was developed.

Magnetization measurements of undoped and BHO-doped YBCO films of various thicknesses showed that the introduction of artificial pinning centers such as BHO into the YBCO layer leads to an enhancement of the global critical current density with a reduced field dependence. This can be attributed to an enhanced pinning landscape with c -axis oriented BHO-nanorods and platelets in the ab -planes of the YBCO layer. Electron microscopy imaging showed that BHO-doping also leads to an enhanced film growth with the reduction of porosity and a refinement of secondary phases in the superconducting layer. Furthermore, electron backscatter diffraction revealed that BHO-doping has no significant influence on the texture of the YBCO film, as

the in-plane and out-of-plane misorientation of grains is the same for both undoped and doped samples. It was found that the increased critical current density in the BHO-doped films can be attributed not only to enhanced pinning but also to a reduction in granularity. The statistical analysis of the magnetic granularity revealed a reduction of granularity by BHO-doping and film thickness which can both be correlated to a more homogeneous YBCO layer and the reduction of pores in the superconducting layer. The reduced magnetic granularity at higher temperatures was attributed to the temperature dependence of weak-links.

SHPM measurements of Fe(Se,Te) thin films on simple RABiTS templates showed that these films also exhibit magnetic granularity. It was found that, similar to the behavior of YBCO films on RABiTS, the Fe(Se,Te) film closely follows the structure of the underlying Ni-W grains and the film growth is severely influenced by the out-of-plane orientation of individual substrate grains. Transmission Kikuchi diffraction analysis showed that the current flow is not necessarily impeded by grain boundaries but by entire grains and grain clusters that are misoriented by a few degrees only.

Microstructural analysis and high-resolution Hall mapping of early-stage Tl-1223 thin films was performed in order to investigate the feasibility of using this material as a coating in the FCC beam screen. The films showed promising high critical temperatures and high local critical current densities, however, this is limited to small areas in the sample. Areas with high and low trapped field were examined with TEM which showed that grain orientation will also be a crucial factor for high-performance conductors based on this material. For that, the deposition conditions and heat treatment need to be optimized in order to achieve a better phase purity and film coverage on the substrate.

The high local current densities that were detected for YBCO and Fe(Se,Te) films on RABiTS show the potential for further optimization of coated conductors based on this template type, especially since films on IBAD-MgO based templates do not exhibit such high current densities. It was found that the currents are not necessarily impeded by grain boundaries but rather by the disturbed film growth on entire substrate grains. BHO-doping is certainly a promising route for the optimization of the YBCO film growth on RABiTS since the porosity in the superconducting

film is largely suppressed, which leads to a more homogeneous and dense YBCO layer. In the case of iron-based coated conductors, it needs to be clarified if optimized growth conditions could lead to a reduction of magnetic granularity in Fe(Se,Te) films. The next step will be to investigate also other iron-based compounds like the BaFe_2As_2 family on their magnetic granularity. Furthermore, it will be interesting to conduct SHPM with sub-micron resolution in order to detect possible magnetic granularity in conductors based on IBAD-MgO templates to understand the current limitations of superconductors based on this template type.

Bibliography

- [1] J. G. Bednorz and K. A. Müller. „Possible high T_c superconductivity in the Ba-La-Cu-O system“. In: *Zeitschrift für Physik B Condensed Matter* 64.2 (1986), pp. 189–193. DOI: 10.1007/bf01303701.
- [2] H. W. Weijers et al. „Progress in the Development of a Superconducting 32 T Magnet With REBCO High Field Coils“. In: *IEEE Transactions on Applied Superconductivity* 24.3 (2014), pp. 1–5. DOI: 10.1109/tasc.2013.2288919.
- [3] S. Yoon et al. „26 T 35 mm all-GdBa₂Cu₃O_{7-x} multi-width no-insulation superconducting magnet“. In: *Superconductor Science and Technology* 29.4 (2016), 04LT04. DOI: 10.1088/0953-2048/29/4/041t04.
- [4] J. van Nugteren et al. „Toward REBCO 20 T+ Dipoles for Accelerators“. In: *IEEE Transactions on Applied Superconductivity* 28.4 (2018), pp. 1–9. DOI: 10.1109/tasc.2018.2820177.
- [5] D. X. Fischer et al. „The effect of fast neutron irradiation on the superconducting properties of REBCO coated conductors with and without artificial pinning centers“. In: *Superconductor Science and Technology* 31.4 (2018), p. 044006. DOI: 10.1088/1361-6668/aaadf2.
- [6] D. Uglietti. „A review of commercial high temperature superconducting materials for large magnets: from wires and tapes to cables and conductors“. In: *Superconductor Science and Technology* 32.5 (2019), p. 053001. DOI: 10.1088/1361-6668/ab06a2.
- [7] N. Mitchell et al. „Superconductors for fusion: a roadmap“. In: *Superconductor Science and Technology* 34.10 (2021), p. 103001. DOI: 10.1088/1361-6668/ac0992.

- [8] S. Awaji et al. „Robust REBCO Insert Coil for Upgrade of 25 T Cryogen-Free Superconducting Magnet“. In: *IEEE Transactions on Applied Superconductivity* 31.5 (2021), pp. 1–5. DOI: 10.1109/tasc.2021.3061896.
- [9] R. Unterrainer et al. „Recovering the performance of irradiated high-temperature superconductors for use in fusion magnets“. In: *Superconductor Science and Technology* 35.4 (2022), 04LT01. DOI: 10.1088/1361-6668/ac4636.
- [10] D. Larbalestier et al. „High- T_c superconducting materials for electric power applications“. In: *Nature* 414.6861 (2001), pp. 368–377. DOI: 10.1038/35104654.
- [11] X. Obradors and T. Puig. „Coated conductors for power applications: materials challenges“. In: *Superconductor Science and Technology* 27.4 (2014), p. 044003. DOI: 10.1088/0953-2048/27/4/044003.
- [12] S. R. Foltyn et al. „Materials science challenges for high-temperature superconducting wire“. In: *Nature Materials* 6.9 (2007), pp. 631–642. DOI: 10.1038/nmat1989.
- [13] K. Heine, J. Tenbrink, and M. Thöner. „High-field critical current densities in $\text{Bi}_2\text{Sr}_2\text{Ca}_1\text{Cu}_2\text{O}_{8+x}/\text{Ag}$ wires“. In: *Applied Physics Letters* 55.23 (1989), pp. 2441–2443. DOI: 10.1063/1.102295.
- [14] D. C. Larbalestier et al. „Isotropic round-wire multifilament cuprate superconductor for generation of magnetic fields above 30 T“. In: *Nature Materials* 13.4 (2014), pp. 375–381. DOI: 10.1038/nmat3887.
- [15] Y. Iijima et al. „In-plane aligned $\text{YBa}_2\text{Cu}_3\text{O}_{7-x}$ thin films deposited on polycrystalline metallic substrates“. In: *Applied Physics Letters* 60.6 (1992), pp. 769–771. DOI: 10.1063/1.106514.
- [16] R. P. Reade et al. „Laser deposition of biaxially textured yttria-stabilized zirconia buffer layers on polycrystalline metallic alloys for high critical current Y-Ba-Cu-O thin films“. In: *Applied Physics Letters* 61.18 (1992), pp. 2231–2233. DOI: 10.1063/1.108277.
- [17] A. Goyal et al. „High critical current density superconducting tapes by epitaxial deposition of $\text{YBa}_2\text{Cu}_3\text{O}_x$ thick films on biaxially textured metals“. In: *Applied Physics Letters* 69.12 (1996), pp. 1795–1797. DOI: 10.1063/1.117489.

- [18] A. Goyal, M. P. Paranthaman, and U. Schoop. „The RABiTS Approach: Using Rolling-Assisted Biaxially Textured Substrates for High-Performance YBCO Superconductors“. In: *MRS Bulletin* 29.8 (2004), pp. 552–561. DOI: 10.1557/mrs2004.161.
- [19] A. Usoskin et al. „Processing of Long-Length YBCO Coated Conductors Based on Stainless Steel Tapes“. In: *IEEE Transactions on Applied Superconductivity* 17.2 (2007), pp. 3235–3238. DOI: 10.1109/tasc.2007.900041.
- [20] J. L. MacManus-Driscoll et al. „Strongly enhanced current densities in superconducting coated conductors of $\text{YBa}_2\text{Cu}_3\text{O}_{7-x} + \text{BaZrO}_3$ “. In: *Nature Materials* 3.7 (2004), pp. 439–443. DOI: 10.1038/nmat1156.
- [21] V. Selvamanickam et al. „Enhanced critical currents in $(\text{Gd},\text{Y})\text{Ba}_2\text{Cu}_3\text{O}_x$ superconducting tapes with high levels of Zr addition“. In: *Superconductor Science and Technology* 26.3 (2013), p. 035006. DOI: 10.1088/0953-2048/26/3/035006.
- [22] J. Hänisch et al. „Formation of nanosized BaIrO_3 precipitates and their contribution to flux pinning in Ir-doped $\text{YBa}_2\text{Cu}_3\text{O}_{7-\delta}$ quasi-multilayers“. In: *Applied Physics Letters* 86.12 (2005), p. 122508. DOI: 10.1063/1.1894599.
- [23] M. Erbe et al. „ BaHfO_3 artificial pinning centres in TFA-MOD-derived YBCO and GdBCO thin films“. In: *Superconductor Science and Technology* 28.11 (2015), p. 114002. DOI: 10.1088/0953-2048/28/11/114002.
- [24] P. Pahlke et al. „Influence of artificial pinning centers on structural and superconducting properties of thick YBCO films on ABAD-YSZ templates“. In: *Superconductor Science and Technology* 31.4 (2018), p. 044007. DOI: 10.1088/1361-6668/aaafbe.
- [25] K. Matsumoto et al. „Irreversibility Fields and Critical Current Densities in Strongly Pinned $\text{YBa}_2\text{Cu}_3\text{O}_{7-x}$ Films With Artificial Pinning Centers“. In: *IEEE Transactions on Applied Superconductivity* 25.3 (2015), pp. 1–6. DOI: 10.1109/tasc.2015.2396358.
- [26] F. Rizzo et al. „Pushing the limits of applicability of REBCO coated conductor films through fine chemical tuning and nanoengineering of inclusions“. In: *Nanoscale* 10.17 (2018), pp. 8187–8195. DOI: 10.1039/c7nr09428k.

- [27] G. Ercolano et al. „State-of-the-art flux pinning in $\text{YBa}_2\text{Cu}_3\text{O}_{7-\delta}$ by the creation of highly linear, segmented nanorods of $\text{Ba}_2(\text{Y/Gd})(\text{Nb/Ta})\text{O}_6$ together with nanoparticles of $(\text{Y/Gd})_2\text{O}_3$ and $(\text{Y/Gd})\text{Ba}_2\text{Cu}_4\text{O}_8$ “. In: *Superconductor Science and Technology* 24.9 (2011), p. 095012. DOI: 10.1088/0953-2048/24/9/095012.
- [28] P. Mele, A. Crisan, and M. I. Adam. „Pinning-Engineered $\text{YBa}_2\text{Cu}_3\text{O}_x$ Thin Films“. In: *Vortices and Nanostructured Superconductors*. Springer International Publishing, 2017, pp. 15–63. DOI: 10.1007/978-3-319-59355-5_2.
- [29] D. M. Feldmann et al. „Improved flux pinning in $\text{YBa}_2\text{Cu}_3\text{O}_7$ with nanorods of the double perovskite Ba_2YNbO_6 “. In: *Superconductor Science and Technology* 23.9 (2010), p. 095004. DOI: 10.1088/0953-2048/23/9/095004.
- [30] S. H. Wee et al. „Enhanced flux pinning and critical current density via incorporation of self-assembled rare-earth barium tantalate nanocolumns within $\text{YBa}_2\text{Cu}_3\text{O}_{7-\delta}$ films“. In: *Physical Review B* 81.14 (2010), p. 140503. DOI: 10.1103/physrevb.81.140503.
- [31] M. Coll et al. „Size-controlled spontaneously segregated Ba_2YTaO_6 nanoparticles in $\text{YBa}_2\text{Cu}_3\text{O}_7$ nanocomposites obtained by chemical solution deposition“. In: *Superconductor Science and Technology* 27.4 (2014), p. 044008. DOI: 10.1088/0953-2048/27/4/044008.
- [32] V. Ogunjimi et al. „Enhancing magnetic pinning by BaZrO_3 nanorods forming coherent interface by strain-directed Ca-doping in $\text{YBa}_2\text{Cu}_3\text{O}_{7-x}$ nanocomposite films“. In: *Superconductor Science and Technology* 34.10 (2021), p. 104002. DOI: 10.1088/1361-6668/ac1fd3.
- [33] H. Tobita et al. „Fabrication of BaHfO_3 doped $\text{Gd}_1\text{Ba}_2\text{Cu}_3\text{O}_{7-\delta}$ coated conductors with the high I_c of 85 A/cm-w under 3 T at liquid nitrogen temperature (77 K)“. In: *Superconductor Science and Technology* 25.6 (2012), p. 062002. DOI: 10.1088/0953-2048/25/6/062002.
- [34] A. Tsuruta et al. „The influence of the geometric characteristics of nanorods on the flux pinning in high-performance BaMO_3 -doped $\text{SmBa}_2\text{Cu}_3\text{O}_y$ films ($M = \text{Hf}, \text{Sn}$)“. In: *Superconductor Science and Technology* 27.6 (2014), p. 065001. DOI: 10.1088/0953-2048/27/6/065001.
- [35] H. Hilgenkamp and J. Mannhart. „Grain boundaries in high- T_c superconductors“. In: *Reviews of Modern Physics* 74.2 (2002), pp. 485–549. DOI: 10.1103/revmodphys.74.485.

- [36] J. H. Durrell and N. A. Rutter. „Importance of low-angle grain boundaries in $\text{YBa}_2\text{Cu}_3\text{O}_{7-\delta}$ coated conductors“. In: *Superconductor Science and Technology* 22.1 (2008), p. 013001. DOI: 10.1088/0953-2048/22/1/013001.
- [37] A. Abada et al. „FCC-hh: The Hadron Collider“. In: *The European Physical Journal Special Topics* 228.4 (2019), pp. 755–1107. DOI: 10.1140/epjst/e2019-900087-0.
- [38] T. Puig et al. „Coated conductor technology for the beamscreen chamber of future high energy circular colliders“. In: *Superconductor Science and Technology* 32.9 (2019), p. 094006. DOI: 10.1088/1361-6668/ab2e66.
- [39] S. Calatroni et al. „Thallium-based high-temperature superconductors for beam impedance mitigation in the Future Circular Collider“. In: *Superconductor Science and Technology* 30.7 (2017), p. 075002. DOI: 10.1088/1361-6668/aa6bd0.
- [40] A. Leveratto et al. „Future Circular Collider beam screen: progress on Tl-1223 HTS coating“. In: *Superconductor Science and Technology* 33.5 (2020), p. 054004. DOI: 10.1088/1361-6668/ab7fbd.
- [41] E. Bellingeri et al. „Preparation of highly textured Tl(1223)/Ag superconducting tapes“. In: *IEEE Transactions on Applied Superconductivity* 9.2 (1999), pp. 1783–1786. DOI: 10.1109/77.784801.
- [42] W. Woch et al. „Critical currents of $(\text{Tl}_{0.5}\text{Pb}_{0.5})(\text{Sr}_{0.85}\text{Ba}_{0.15})_2\text{Ca}_2\text{Cu}_3\text{O}_z$ films on untextured silver substrates“. In: *Journal of Alloys and Compounds* 442.1-2 (2007), pp. 209–212. DOI: 10.1016/j.jallcom.2006.10.172.
- [43] Y. Kamihara et al. „Iron-Based Layered Superconductor $\text{La}[\text{O}_{1-x}\text{F}_x]\text{FeAs}$ ($x = 0.05\text{--}0.12$) with $T_c = 26\text{ K}$ “. In: *Journal of the American Chemical Society* 130.11 (2008), pp. 3296–3297. DOI: 10.1021/ja800073m.
- [44] K. Iida, J. Hänisch, and C. Tarantini. „Fe-based superconducting thin films on metallic substrates: Growth, characteristics, and relevant properties“. In: *Applied Physics Reviews* 5.3 (2018), p. 031304. DOI: 10.1063/1.5032258.
- [45] I. Pallecchi et al. „Application potential of Fe-based superconductors“. In: *Superconductor Science and Technology* 28.11 (2015), p. 114005. DOI: 10.1088/0953-2048/28/11/114005.

- [46] H. Hosono et al. „Recent advances in iron-based superconductors toward applications“. In: *Materials Today* 21.3 (2018), pp. 278–302. DOI: 10.1016/j.mattod.2017.09.006.
- [47] K. Iida, J. Hänisch, and A. Yamamoto. „Grain boundary characteristics of Fe-based superconductors“. In: *Superconductor Science and Technology* 33.4 (2020), p. 043001. DOI: 10.1088/1361-6668/ab73ef.
- [48] T. Katase et al. „Advantageous grain boundaries in iron pnictide superconductors“. In: *Nature Communications* 2.1 (2011). DOI: 10.1038/ncomms1419.
- [49] J. D. Weiss et al. „High intergrain critical current density in fine-grain $(\text{Ba}_{0.6}\text{K}_{0.4})\text{Fe}_2\text{As}_2$ wires and bulks“. In: *Nature Materials* 11.8 (2012), pp. 682–685. DOI: 10.1038/nmat3333.
- [50] T. Tamegai et al. „Developments of $(\text{Ba},\text{Na})\text{Fe}_2\text{As}_2$ and $\text{CaKFe}_4\text{As}_4$ HIP round wires“. In: *Superconductor Science and Technology* 33.10 (2020), p. 104001. DOI: 10.1088/1361-6668/abaa38.
- [51] W. Guo et al. „Enhancement of transport J_c in $(\text{Ba}, \text{K})\text{Fe}_2\text{As}_2$ HIP processed round wires“. In: *Superconductor Science and Technology* 34.9 (2021), p. 094001. DOI: 10.1088/1361-6668/ac1952.
- [52] K. Iida et al. „Epitaxial Growth of Superconducting $\text{Ba}(\text{Fe}_{1-x}\text{Co}_x)_2\text{As}_2$ Thin Films on Technical Ion Beam Assisted Deposition MgO Substrates“. In: *Applied Physics Express* 4.1 (2010), p. 013103. DOI: 10.1143/apex.4.013103.
- [53] T. Katase et al. „Biaxially textured cobalt-doped BaFe_2As_2 films with high critical current density over $1 \text{ MA}/\text{cm}^2$ on MgO-buffered metal-tape flexible substrates“. In: *Applied Physics Letters* 98.24 (2011), p. 242510. DOI: 10.1063/1.3599844.
- [54] S. Trommler et al. „Architecture, microstructure and J_c anisotropy of highly oriented biaxially textured Co-doped BaFe_2As_2 on Fe/IBAD-MgO-buffered metal tapes“. In: *Superconductor Science and Technology* 25.8 (2012), p. 084019. DOI: 10.1088/0953-2048/25/8/084019.
- [55] W. Si et al. „High current superconductivity in $\text{FeSe}_{0.5}\text{Te}_{0.5}$ -coated conductors at 30 tesla“. In: *Nature Communications* 4.1 (2013). DOI: 10.1038/ncomms2337.

- [56] H. Sato et al. „Enhanced critical-current in P-doped BaFe₂As₂ thin films on metal substrates arising from poorly aligned grain boundaries“. In: *Scientific Reports* 6.1 (2016). DOI: 10.1038/srep36828.
- [57] G. Sylva et al. „Fe(Se,Te) coated conductors deposited on simple rolling-assisted biaxially textured substrate templates“. In: *Superconductor Science and Technology* 32.8 (2019), p. 084006. DOI: 10.1088/1361-6668/ab0e98.
- [58] G. Sylva et al. „Analysis of Fe(Se,Te) Films Deposited On Unbuffered Invar 36“. In: *IEEE Transactions on Applied Superconductivity* 29.5 (2019), pp. 1–5. DOI: 10.1109/tasc.2019.2893585.
- [59] A. Zampa et al. „Influence of local inhomogeneities in the REBCO layer on the mechanism of quench onset in 2G HTS tapes“. In: *IEEE Transactions on Applied Superconductivity* (2022), pp. 1–1. DOI: 10.1109/tasc.2022.3151950.
- [60] M. Lao et al. „Magnetic granularity in pulsed laser deposited YBCO films on technical templates at 5 K“. In: *Superconductor Science and Technology* 30.10 (2017), p. 104003. DOI: 10.1088/1361-6668/aa7f68.
- [61] M. Sieger et al. „BaHfO₃-Doped Thick YBa₂Cu₃O_{7- δ} Films on Highly Alloyed Textured Ni-W Tapes“. In: *IEEE Transactions on Applied Superconductivity* 25.3 (2015), pp. 1–4. DOI: 10.1109/tasc.2014.2372903.
- [62] M. Sieger et al. „Thick Secondary Phase Pinning-Enhanced YBCO Films on Technical Templates“. In: *IEEE Transactions on Applied Superconductivity* 28.4 (2018), pp. 1–5. DOI: 10.1109/tasc.2018.2799419.
- [63] P. Pahlke et al. „Local Orientation Variations in YBCO Films on Technical Substrates - A Combined SEM and EBSD Study“. In: *IEEE Transactions on Applied Superconductivity* 26.3 (2016), pp. 1–5. DOI: 10.1109/tasc.2016.2535138.
- [64] S. Holleis et al. „Reduced granularity in BHO-doped YBCO films on RABiTS templates“. In: *Superconductor Science and Technology* (2022). DOI: 10.1088/1361-6668/ac883c.

- [65] S. Holleis et al. „Magnetic granularity in PLD-grown Fe(Se,Te) films on simple RABiTS templates“. In: *Superconductor Science and Technology* 35.7 (2022), p. 074001. DOI: 10.1088/1361-6668/ac6cab.
- [66] M. Tinkham. *Introduction to Superconductivity*. Dover Publications, Inc., 1996.
- [67] C. P. Bean. „Magnetization of Hard Superconductors“. In: *Physical Review Letters* 8.6 (1962), pp. 250–253. DOI: 10.1103/physrevlett.8.250.
- [68] F. Hengstberger et al. „Assessing the spatial and field dependence of the critical current density in YBCO bulk superconductors by scanning Hall probes“. In: *Superconductor Science and Technology* 22.2 (2009), p. 025011. DOI: 10.1088/0953-2048/22/2/025011.
- [69] J. H. Durrell et al. „The behavior of grain boundaries in the Fe-based superconductors“. In: *Reports on Progress in Physics* 74.12 (2011), p. 124511. DOI: 10.1088/0034-4885/74/12/124511.
- [70] L. S. Yu et al. „Alignment of thin films by glancing angle ion bombardment during deposition“. In: *Applied Physics Letters* 47.9 (1985), pp. 932–933. DOI: 10.1063/1.95931.
- [71] M. Bauer, R. Semerad, and H. Kinder. „YBCO films on metal substrates with biaxially aligned MgO buffer layers“. In: *IEEE Transactions on Applied Superconductivity* 9.2 (1999), pp. 1502–1505. DOI: 10.1109/77.784678.
- [72] J.-Y. Genoud et al. „Preparation of {110} textured Ag ribbons for biaxially aligned superconducting tapes“. In: *IEEE Transactions on Applied Superconductivity* 11.1 (2001), pp. 3371–3374. DOI: 10.1109/77.919785.
- [73] J. Clarke and A. I. Braginski. *The SQUID Handbook*. Wiley, 2004. DOI: 10.1002/3527603646.
- [74] D. B. Williams and C. B. Carter. *Transmission Electron Microscopy: A Textbook for Materials Science*. Springer, 1996. DOI: 10.1007/978-1-4757-2519-3.
- [75] G. C. Sneddon, P. W. Trimby, and J. M. Cairney. „Transmission Kikuchi diffraction in a scanning electron microscope: A review“. In: *Materials Science and Engineering: R: Reports* 110 (2016), pp. 1–12. DOI: 10.1016/j.mser.2016.10.001.

- [76] P. W. Trimby. „Orientation mapping of nanostructured materials using transmission Kikuchi diffraction in the scanning electron microscope“. In: *Ultramicroscopy* 120 (2012), pp. 16–24. DOI: 10.1016/j.ultramicro.2012.06.004.
- [77] M. Sieger et al. „Tailoring Microstructure and Superconducting Properties in Thick BaHfO₃ and Ba₂Y(Nb/Ta)O₆ Doped YBCO Films on Technical Templates“. In: *IEEE Transactions on Applied Superconductivity* 27.4 (2017), pp. 1–7. DOI: 10.1109/tasc.2016.2644858.
- [78] J. Wu and J. Shi. „Interactive modeling-synthesis-characterization approach towards controllable in situ self-assembly of artificial pinning centers in RE-123 films“. In: *Superconductor Science and Technology* 30.10 (2017), p. 103002. DOI: 10.1088/1361-6668/aa8288.
- [79] B. Gautam et al. „Microscopic adaptation of BaHfO₃ and Y₂O₃ artificial pinning centers for strong and isotropic pinning landscape in YBa₂Cu₃O_{7-x} thin films“. In: *Superconductor Science and Technology* 31.2 (2018), p. 025008. DOI: 10.1088/1361-6668/aaa105.
- [80] S. Miura et al. „Improvement in J_c performance below liquid nitrogen temperature for SmBa₂Cu₃O_y superconducting films with BaHfO₃ nano-rods controlled by low-temperature growth“. In: *APL Materials* 4.1 (2016), p. 016102. DOI: 10.1063/1.4939182.
- [81] P. Pahlke et al. „Thick High J_c YBCO Films on ABAD-YSZ Templates“. In: *IEEE Transactions on Applied Superconductivity* 25.3 (2015), pp. 1–4. DOI: 10.1109/tasc.2014.2378533.
- [82] S. R. Foltyn et al. „Relationship between film thickness and the critical current of YBa₂Cu₃O_{7-δ}-coated conductors“. In: *Applied Physics Letters* 75.23 (1999), pp. 3692–3694. DOI: 10.1063/1.125431.
- [83] S. R. Foltyn et al. „Strongly coupled critical current density values achieved in Y₁Ba₂Cu₃O_{7-δ} coated conductors with near-single-crystal texture“. In: *Applied Physics Letters* 82.25 (2003), pp. 4519–4521. DOI: 10.1063/1.1584783.
- [84] D. Stauffer and A. Aharony. *Introduction To Percolation Theory*. Taylor & Francis, 2018. DOI: 10.1201/9781315274386.
- [85] M. Eisterer. „Predicting critical currents in grain-boundary limited superconductors“. In: *Physical Review B* 99.9 (2019), p. 094501. DOI: 10.1103/physrevb.99.094501.

- [86] Z. Chen et al. „A high critical current density MOCVD coated conductor with strong vortex pinning centers suitable for very high field use“. In: *Superconductor Science and Technology* 22.5 (2009), p. 055013. DOI: 10.1088/0953-2048/22/5/055013.
- [87] A. A. Thomas et al. „Comparative study of Fe(Se,Te) thin films on flexible coated conductor templates and single-crystal substrates“. In: *Superconductor Science and Technology* 34.11 (2021), p. 115013. DOI: 10.1088/1361-6668/ac2557.
- [88] R. A. Hawsey and D. K. Christen. „Progress in research, development, and pre-commercial deployment of second generation HTS wires in the USA“. In: *Physica C: Superconductivity and its Applications* 445-448 (2006), pp. 488–495. DOI: 10.1016/j.physc.2006.04.062.

Appendix

A YBCO - Macroscopic Magnetic Properties

The following figures show complementary results on the BHO-doped and pure YBCO films obtained with magnetization measurements in the SQUID magnetometer.

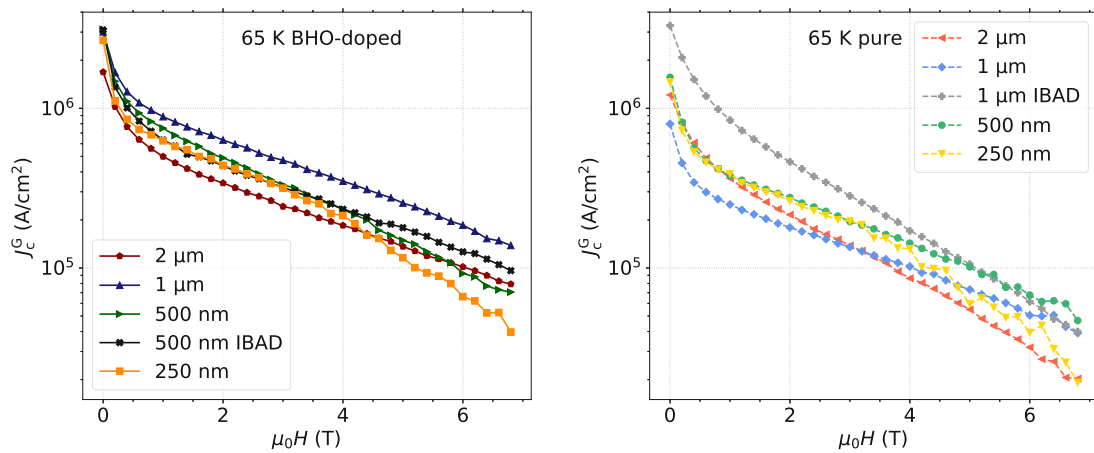


Figure A.1: Field dependence of the global critical current density J_c^G of BHO-doped and pure YBCO samples at 65 K.

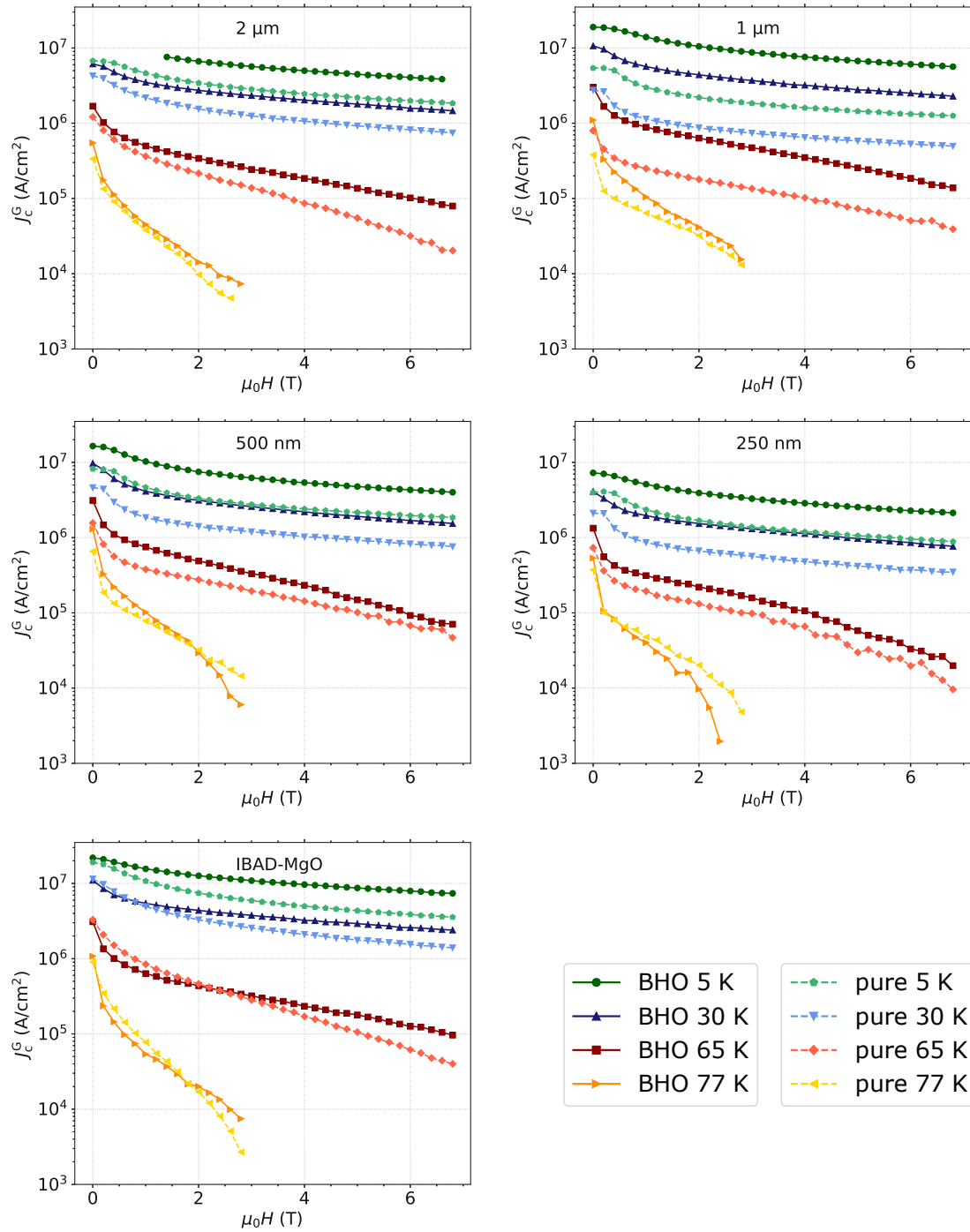


Figure A.2: Field dependence of the global critical current density J_c^G of BHO-doped and pure YBCO samples on RABiTS and IBAD-MgO templates at various thicknesses and temperatures.

B YBCO - High-resolution SHPM

Figures B.1 and B.2 show the remnant field maps and local current density maps of all BHO-doped and pure YBCO samples at 77 K with a spatial resolution of 50 μm . Two spots from each sample were prepared for high-resolution SHPM. The remnant field maps and local current density maps of all spots at 5 K, 30 K and 77 K with a spatial resolution of 7 μm can be found in Figures B.3–B.12.

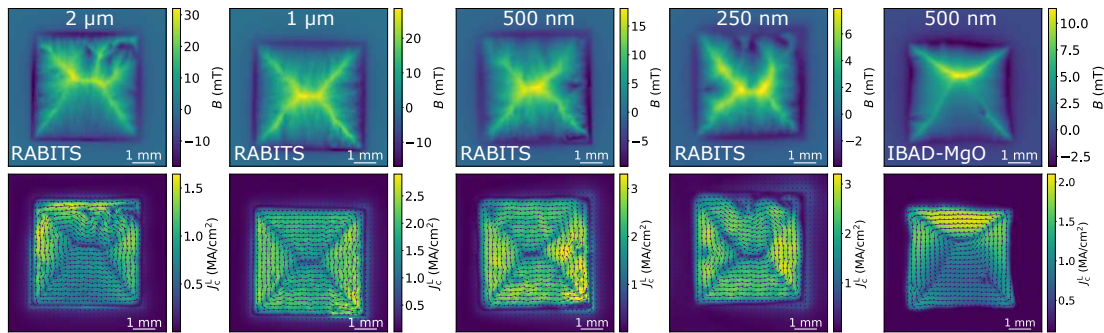


Figure B.1: Remnant field maps (upper panels) and local current density maps (lower panels) of the BHO-doped samples at 77 K with a spatial resolution of 50 μm .

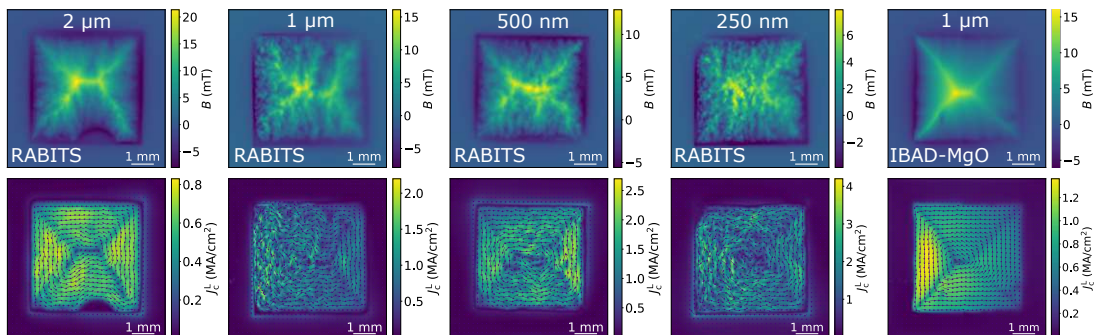


Figure B.2: Remnant field maps (upper panels) and local current density maps (lower panels) of the pure YBCO samples at 77 K with a spatial resolution of 50 μm .

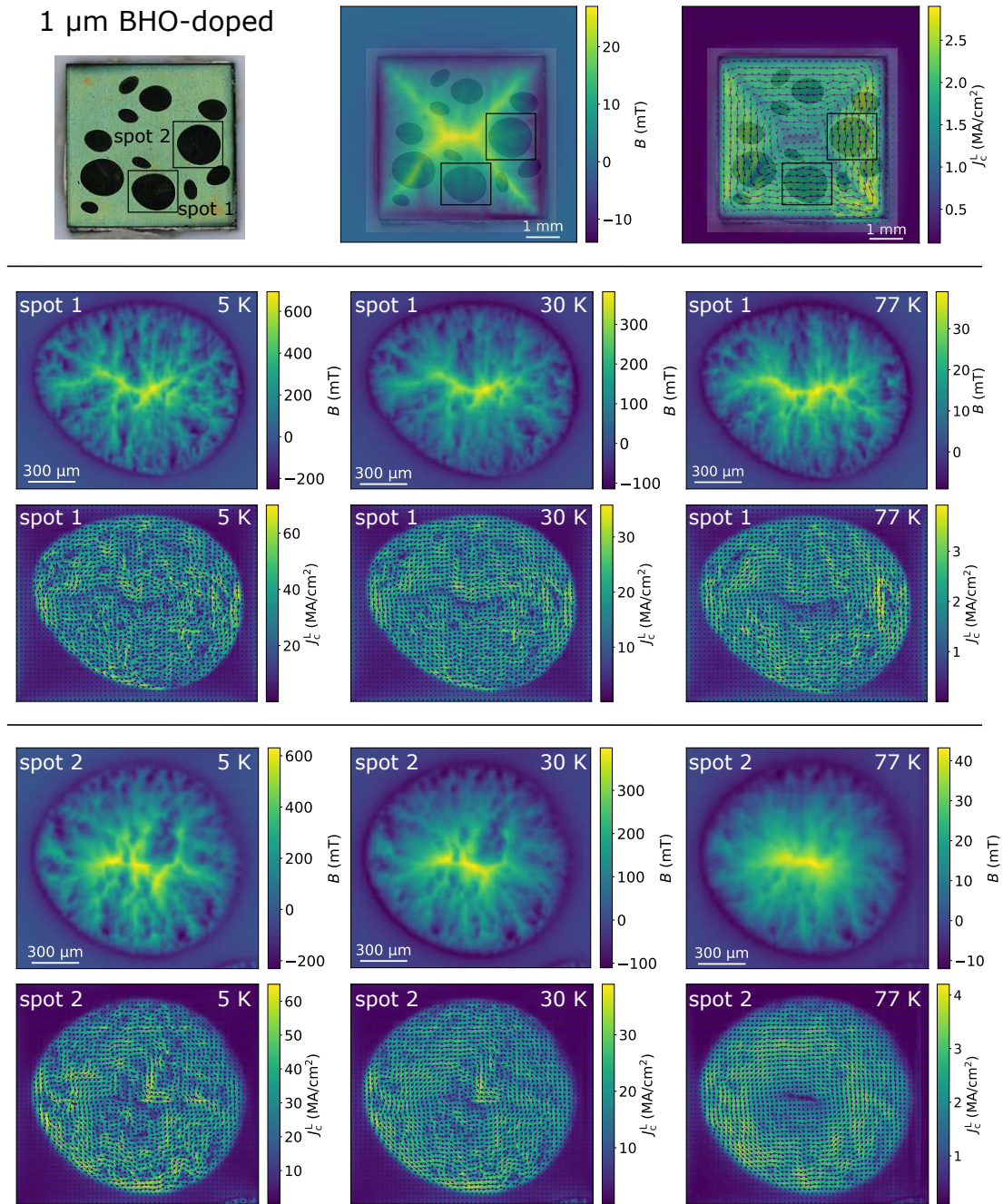


Figure B.4: Remnant field maps and local current density maps of the two spots prepared from the 1 μm BHO-doped film on RABiTS at 5 K, 30 K and 77 K. The spatial resolution is 7 μm for all maps.

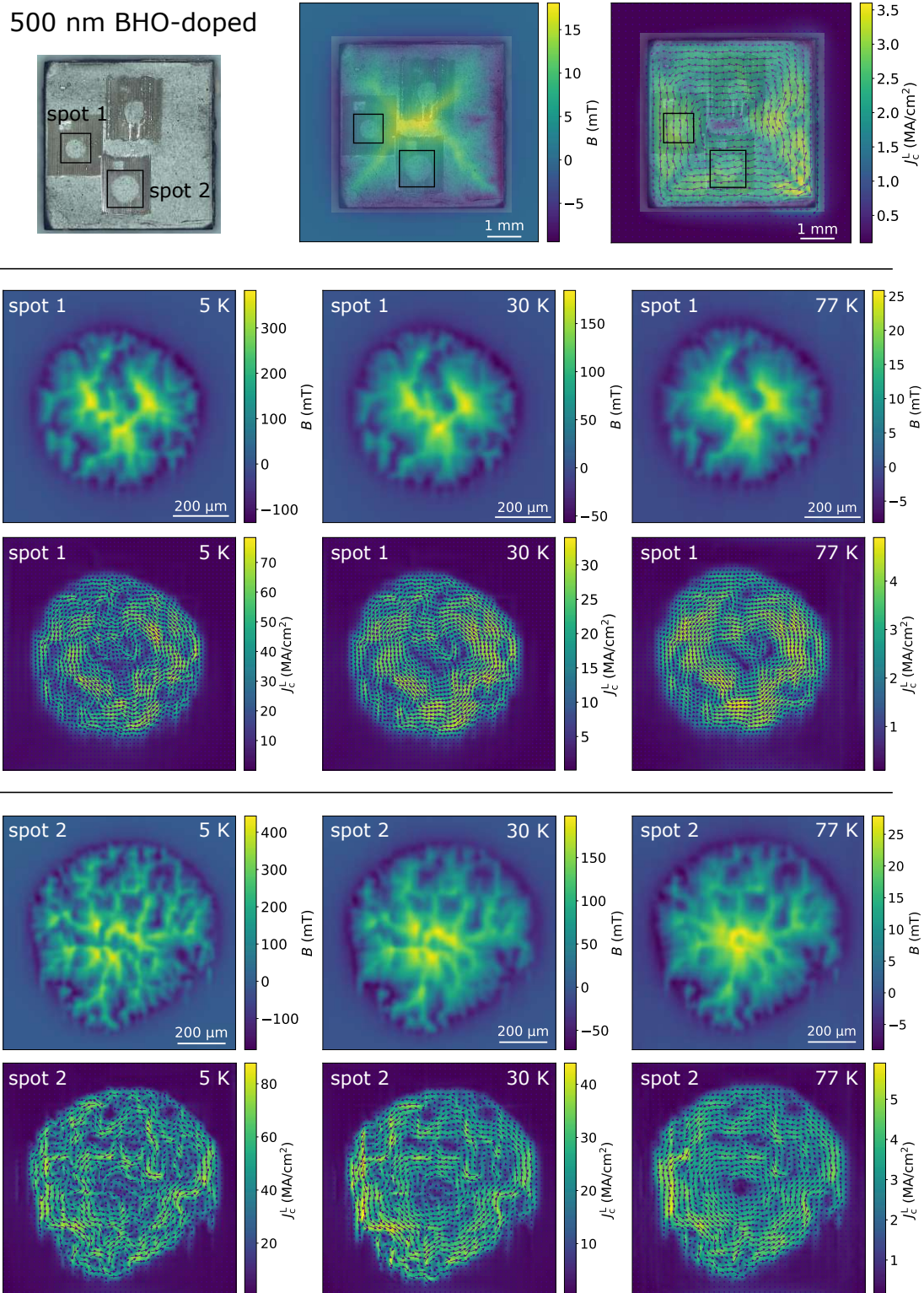


Figure B.5: Remnant field maps and local current density maps of the two spots prepared from the 500 nm BHO-doped film on RABiTS at 5 K, 30 K and 77 K. The spatial resolution is 7 µm for all maps.

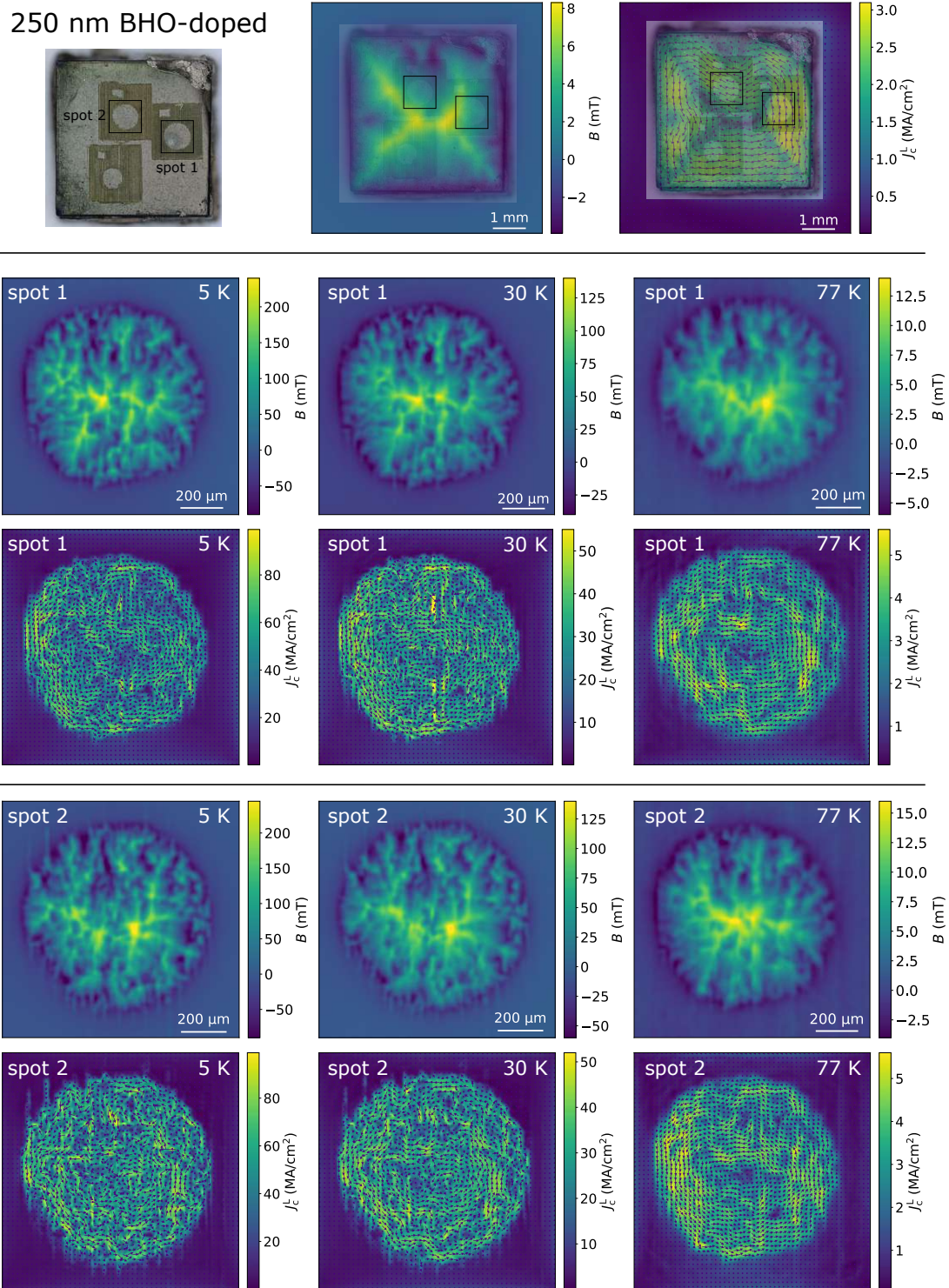


Figure B.6: Remnant field maps and local current density maps of the two spots prepared from the 250 nm BHO-doped film on RABiTS at 5 K, 30 K and 77 K. The spatial resolution is 7 μ m for all maps.

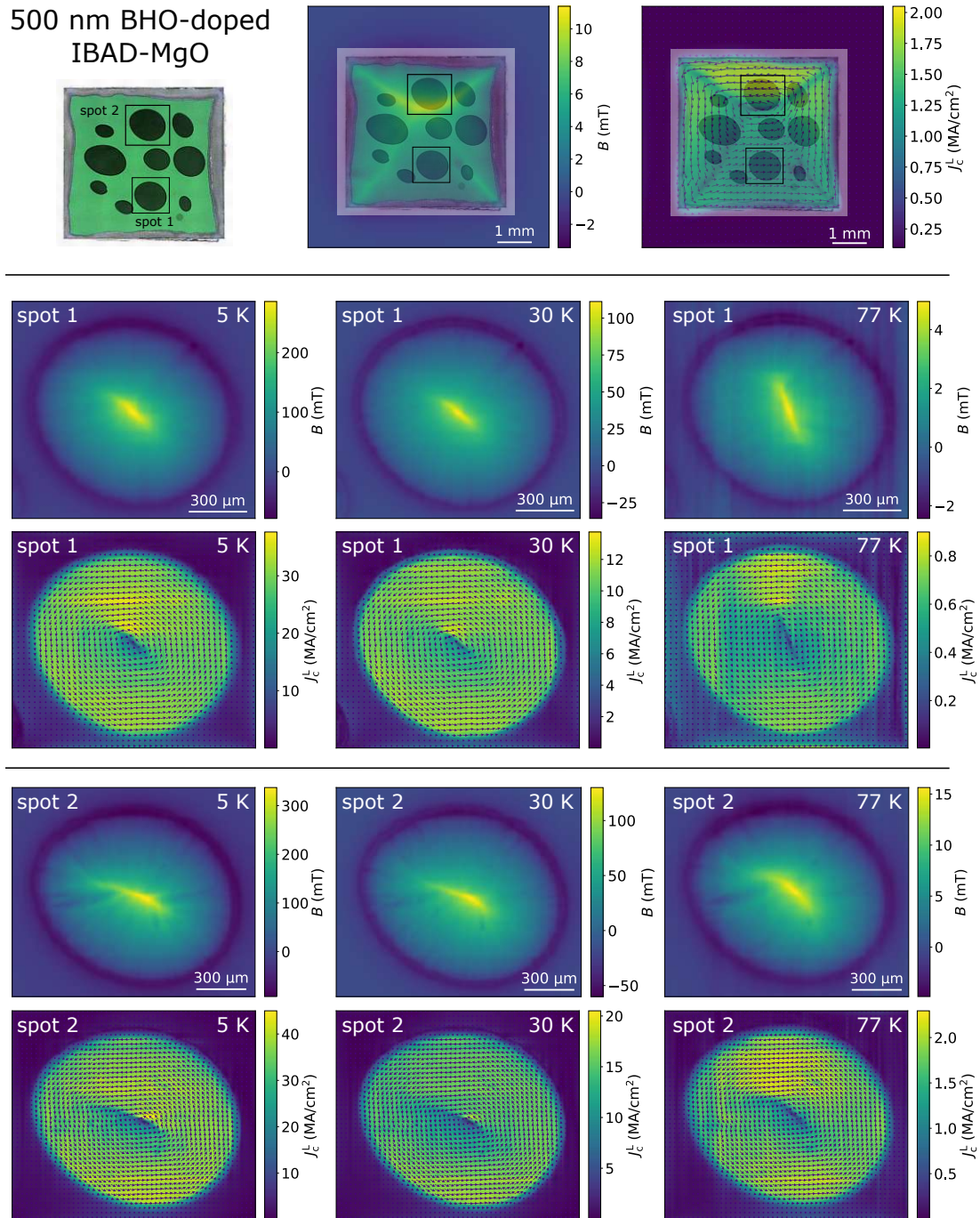
500 nm BHO-doped
IBAD-MgO

Figure B.7: Remnant field maps and local current density maps of the two spots prepared from the 500 nm BHO-doped film on IBAD-MgO at 5 K, 30 K and 77 K. The spatial resolution is 7 μm for all maps.

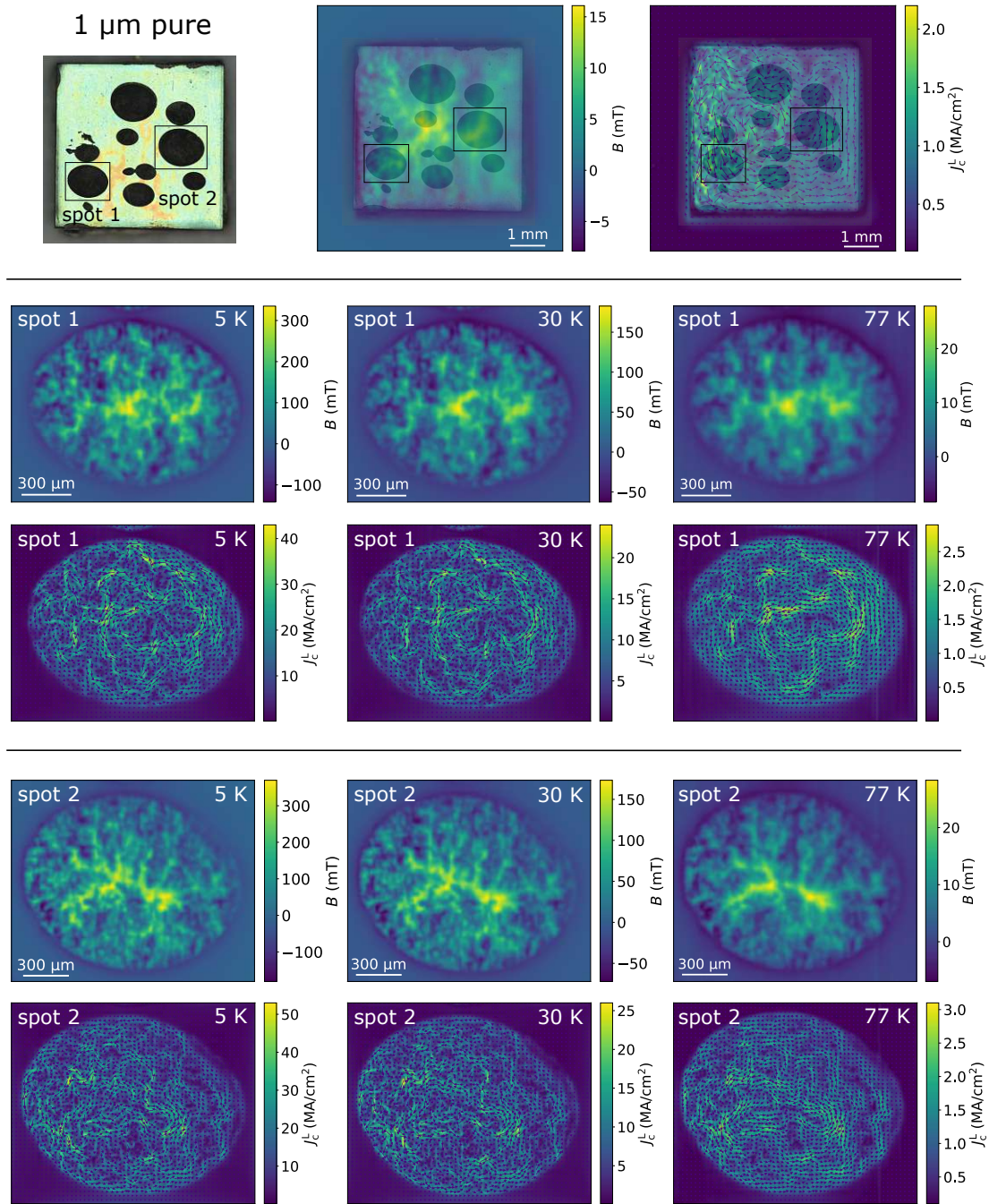


Figure B.9: Remnant field maps and local current density maps of the two spots prepared from the 1 μm pure YBCO film on RABiTS at 5 K, 30 K and 77 K. The spatial resolution is 7 μm for all maps.

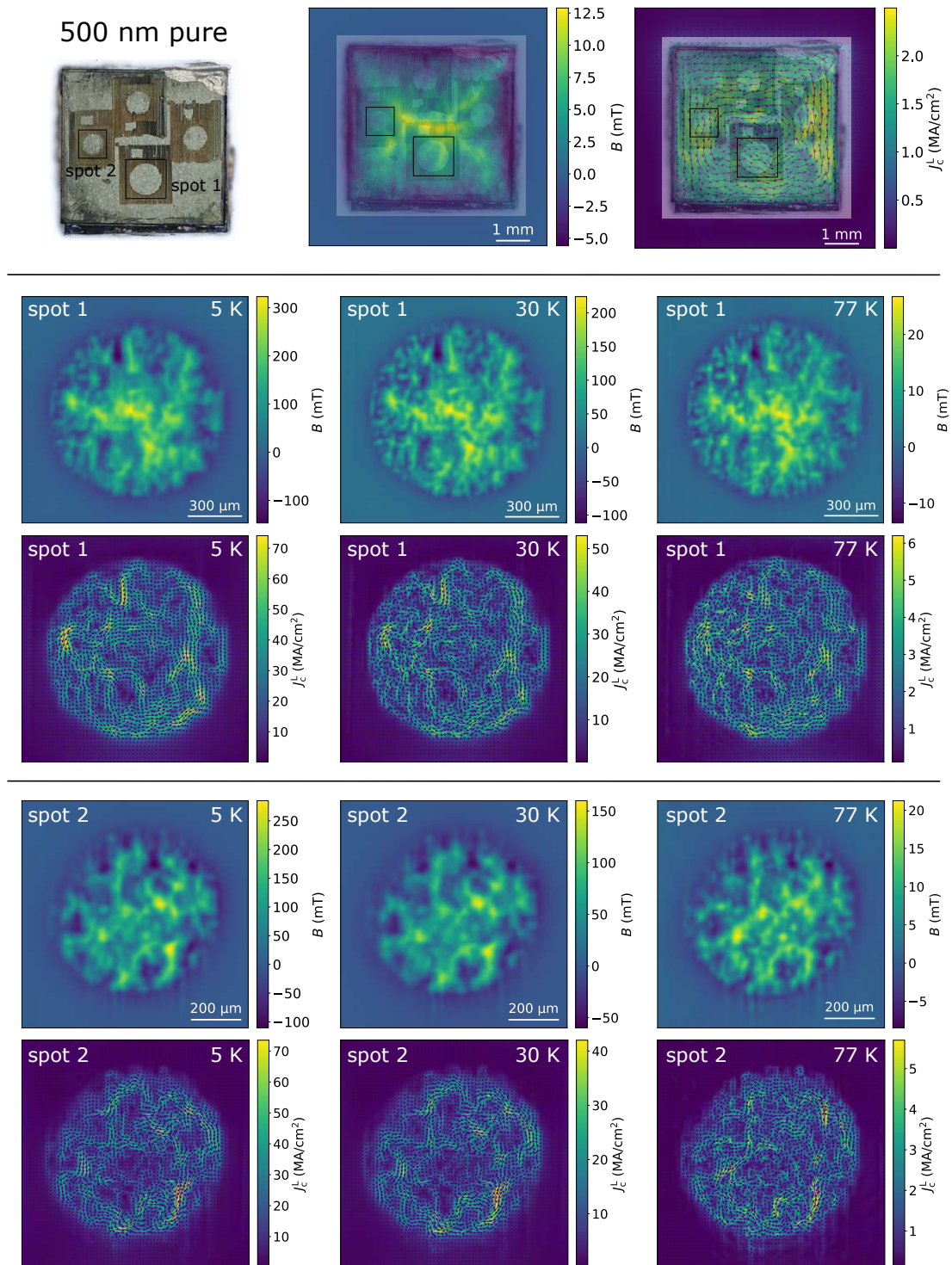


Figure B.10: Remnant field maps and local current density maps of the two spots prepared from the 500 nm pure YBCO film on RABiTS at 5 K, 30 K and 77 K. The spatial resolution is 7 μ m for all maps.

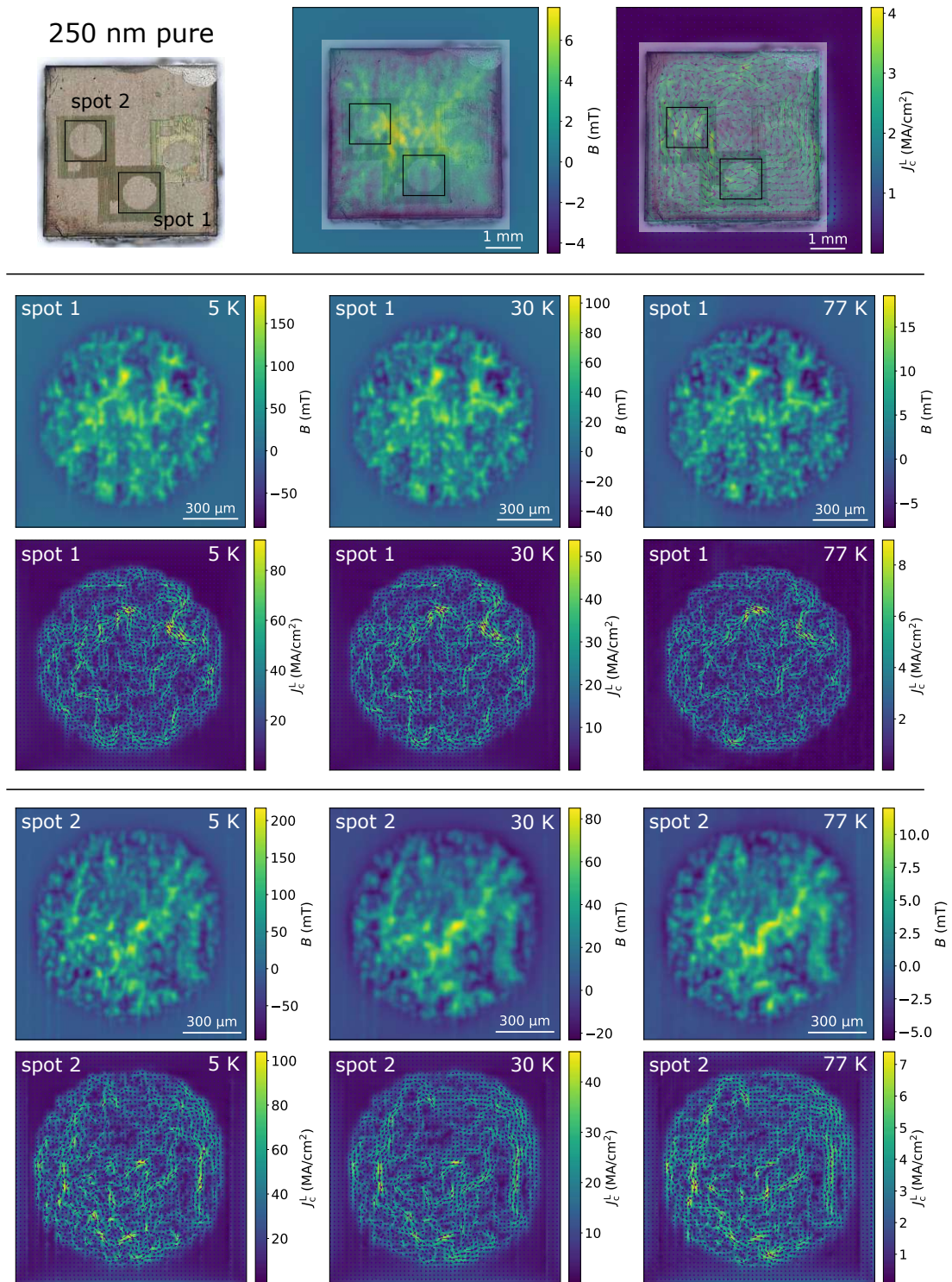


Figure B.11: Remnant field maps and local current density maps of the two spots prepared from the 250 nm pure YBCO film on RABiTS at 5 K, 30 K and 77 K. The spatial resolution is 7 μ m for all maps.

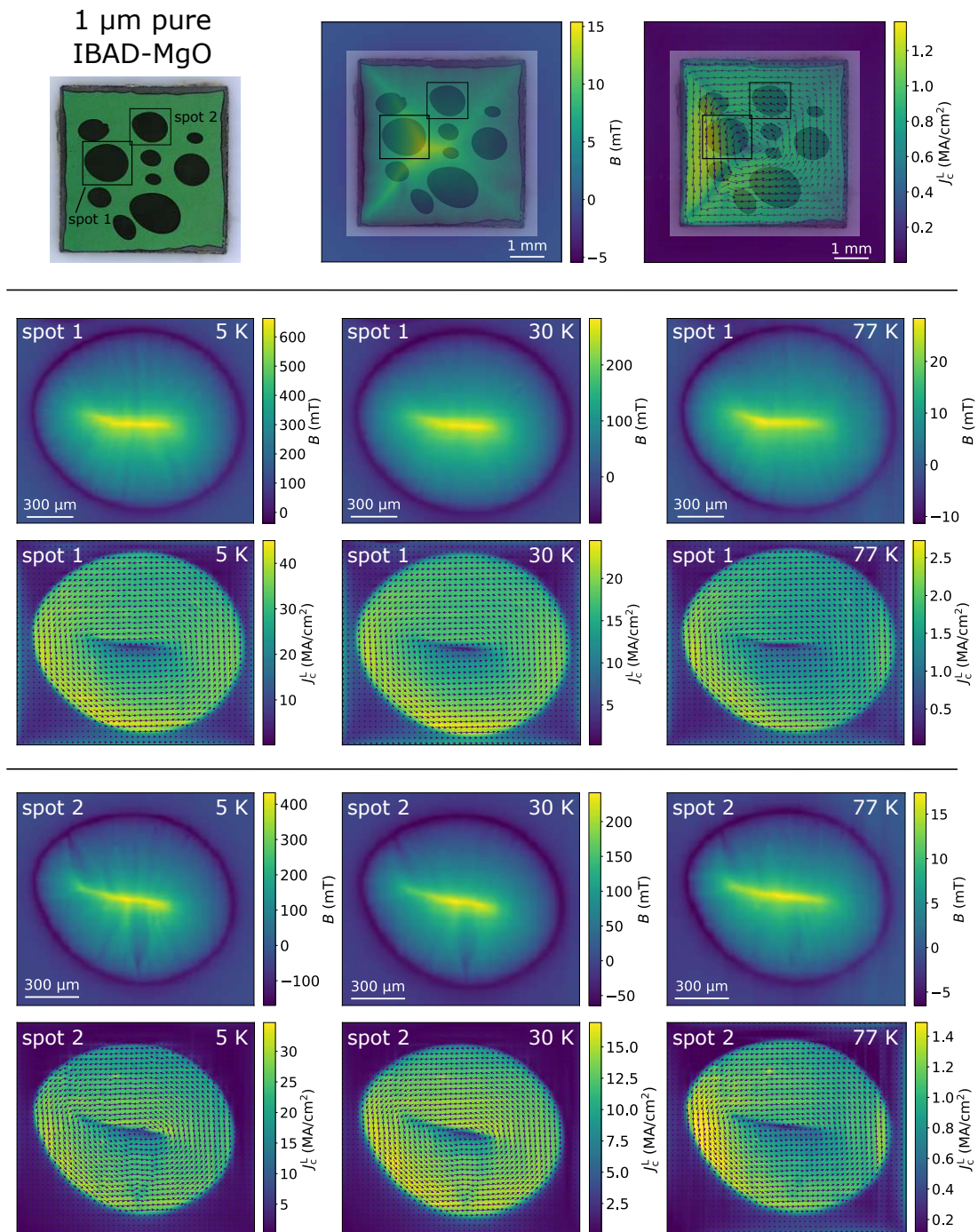


Figure B.12: Remnant field maps and local current density maps of the two spots prepared from the 1 μm pure YBCO film on IBAD-MgO at 5 K, 30 K and 77 K. The spatial resolution is 7 μm for all maps.

C YBCO - Statistical Analysis

The J_c^L distributions of all spots on RABiTS can be found in Figure C.1. A comparison of the BHO-doped and pure YBCO spots is given for all thicknesses at 5 K, 30 K and 77 K.

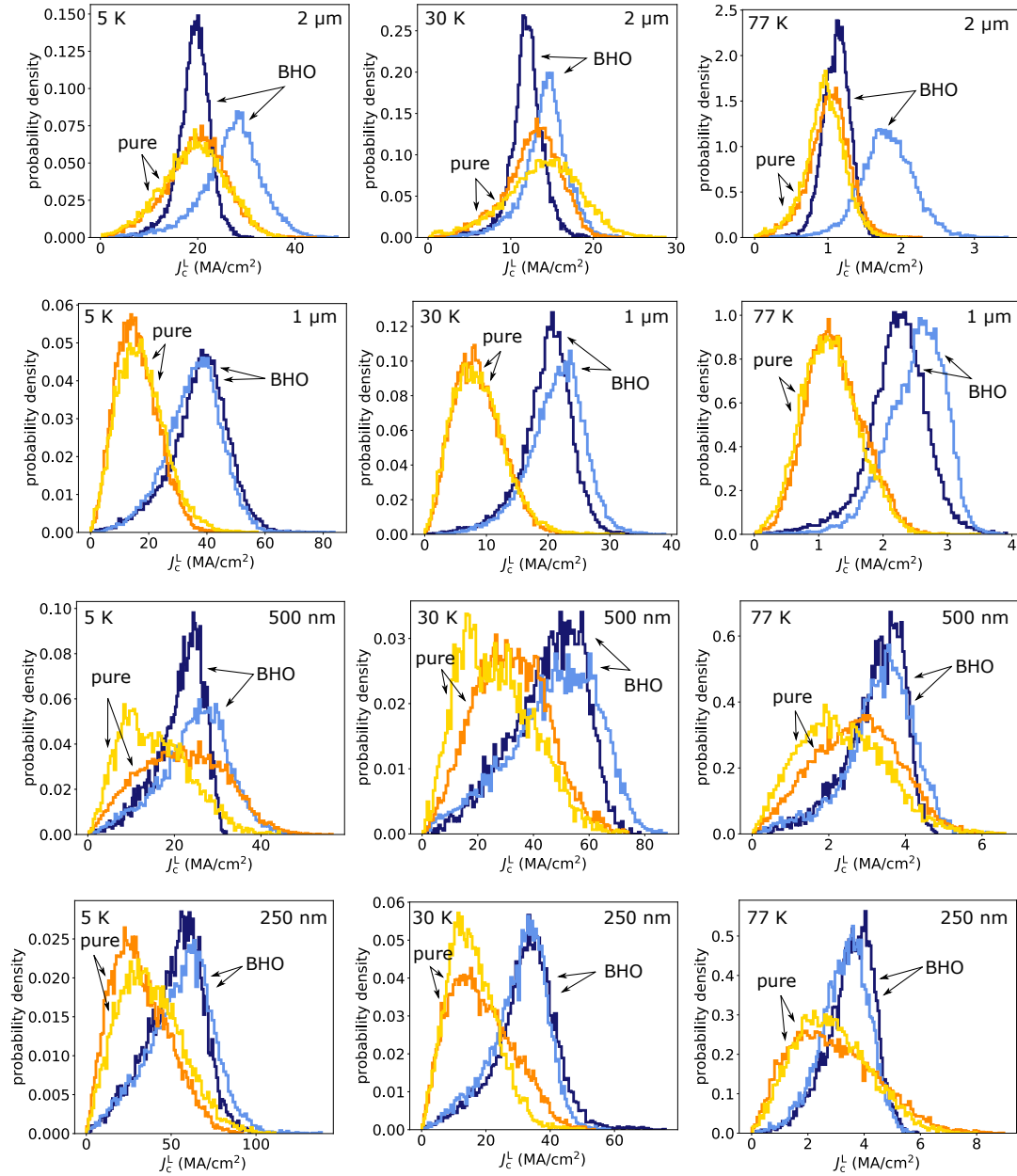


Figure C.1: Comparison of the J_c^L distributions between the BHO-doped and pure YBCO spots on RABiTS at 5 K, 30 K and 77 K.

D YBCO - TEM

The following figures show a summary of the TEM investigations of the BHO-doped and pure YBCO samples with thicknesses 1 μm and 250 nm.

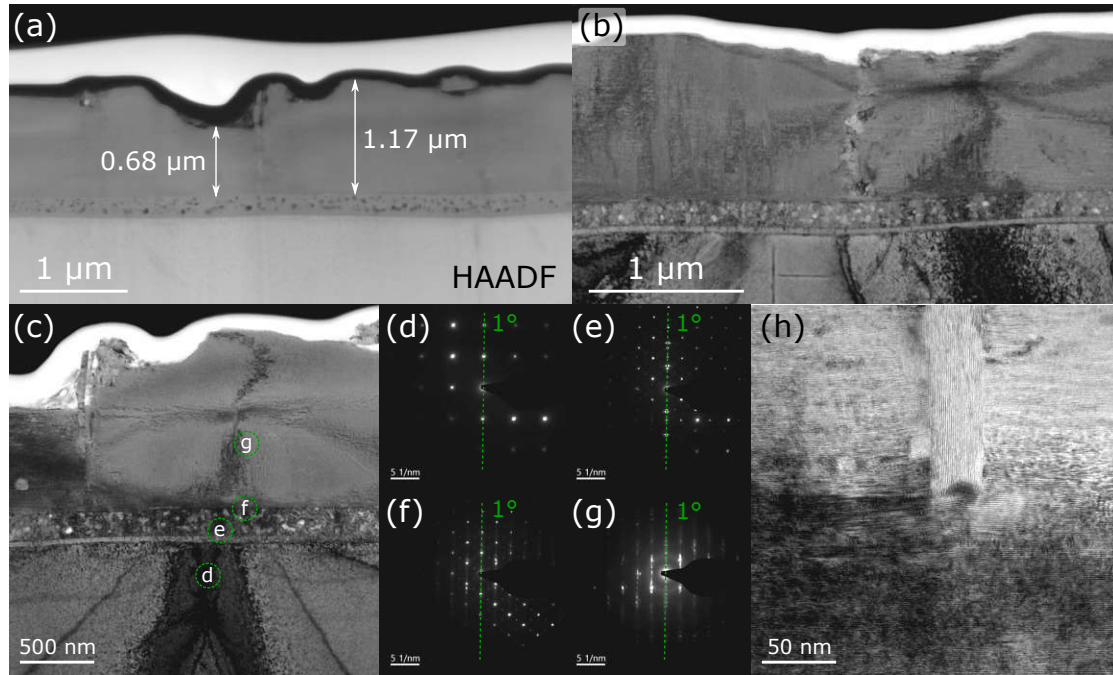


Figure D.1: TEM images of the 1 μm BHO-doped YBCO film. The HAADF image shows an overview of the TEM lamella with variations in the film thickness (a). The superconducting layer appears dense with some secondary phases present (b). Four areas in the substrate, buffer layers and YBCO layer were chosen to record diffraction patterns (c). The diffraction patterns show the epitaxial film growth, as the same line of diffraction points can be identified in all four areas (d–g). The lines of diffraction points exhibit a tilt of 1° with respect to the vertical (green dashed lines) which corresponds to an out-of-plane tilt of 1° in all layers. A high-resolution TEM image shows that an a -axis grain originates at a grain boundary in the YBCO layer (h).

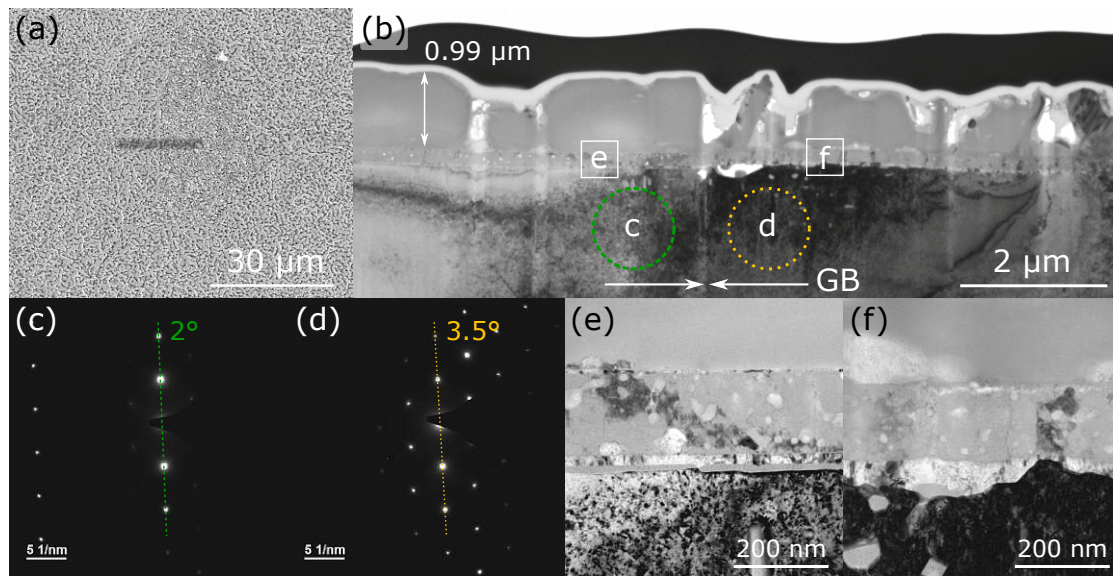


Figure D.2: TEM images of the 1 μm pure YBCO film. SEM image of the area where the TEM lamella was prepared across a GB with current flow on the left and no current flow on the right side of the GB (a). A TEM image gives an overview of the lamella, the GB in the substrate is indicated by white horizontal arrows (b). While the superconducting layer is more or less smooth with some secondary phases and pores on the left side of the GB, the film growth is clearly disturbed on the right side. The diffraction pattern of the substrate on the left side of the GB reveals an out-of-plane tilt of 2° (c), while on the right side of the GB, an out-of-plane tilt of 3.5° can be observed (d). In this case, the roughness of the Ni-W grain surface clearly has an impact on the growth of the YBCO layer on top. On the left side, a smooth transition from the substrate to the buffer layers can be observed (e), while on the right side, the rough surface of the Ni-W grain cannot completely be overcome by the buffer layers on top (f).

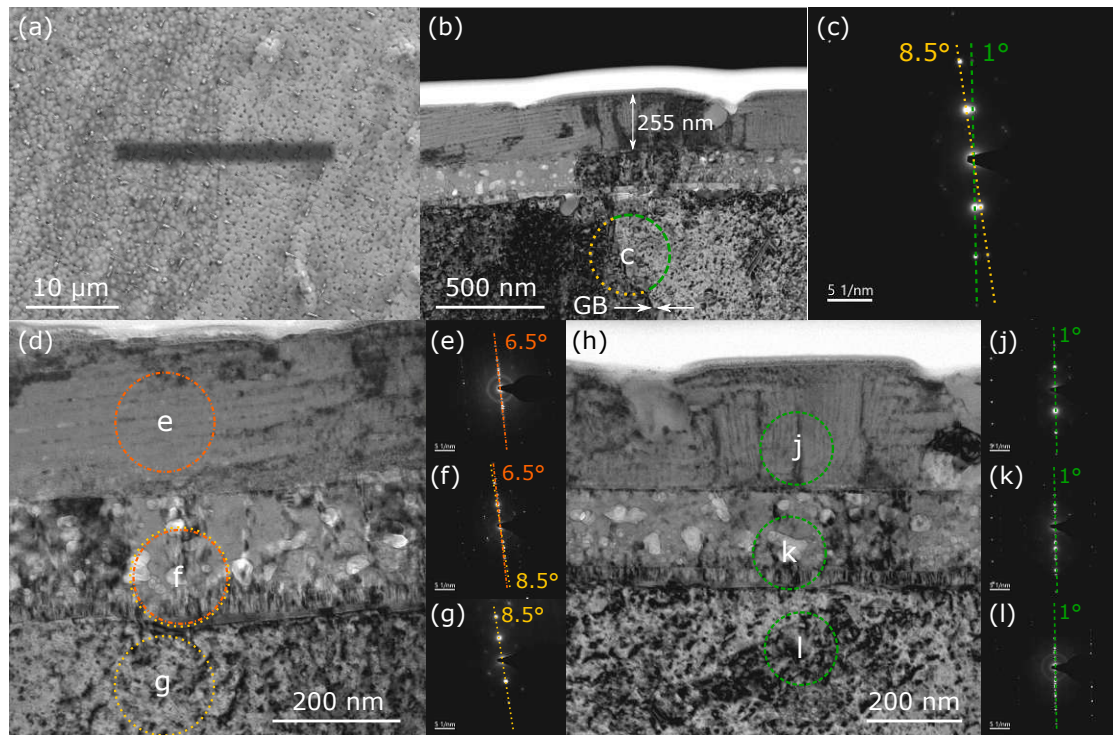


Figure D.3: TEM images of the 250 nm BHO-doped YBCO film. SEM image of the area where the TEM lamella was prepared across a GB with current flow on the right and no current flow on the left side of the GB (a). A TEM image gives an overview of the lamella, the GB in the substrate is indicated by white horizontal arrows (b). The diffraction pattern from the selected area across the GB in the substrate shows two lines of diffraction points (c). One line is tilted by 1° with respect to the vertical (green dashed line) and corresponds to the out-of-plane tilt on the right side of the GB. The other line is tilted by 8.5° with respect to the vertical (yellow dotted line) and corresponds to the out-of-plane tilt on the left side of the GB. On the left, the buffer layer reduces the out-of-plane tilt to 6.5° in the superconducting layer (d–g), while on the right, a tilt of 1° is maintained through all layers (h–l).

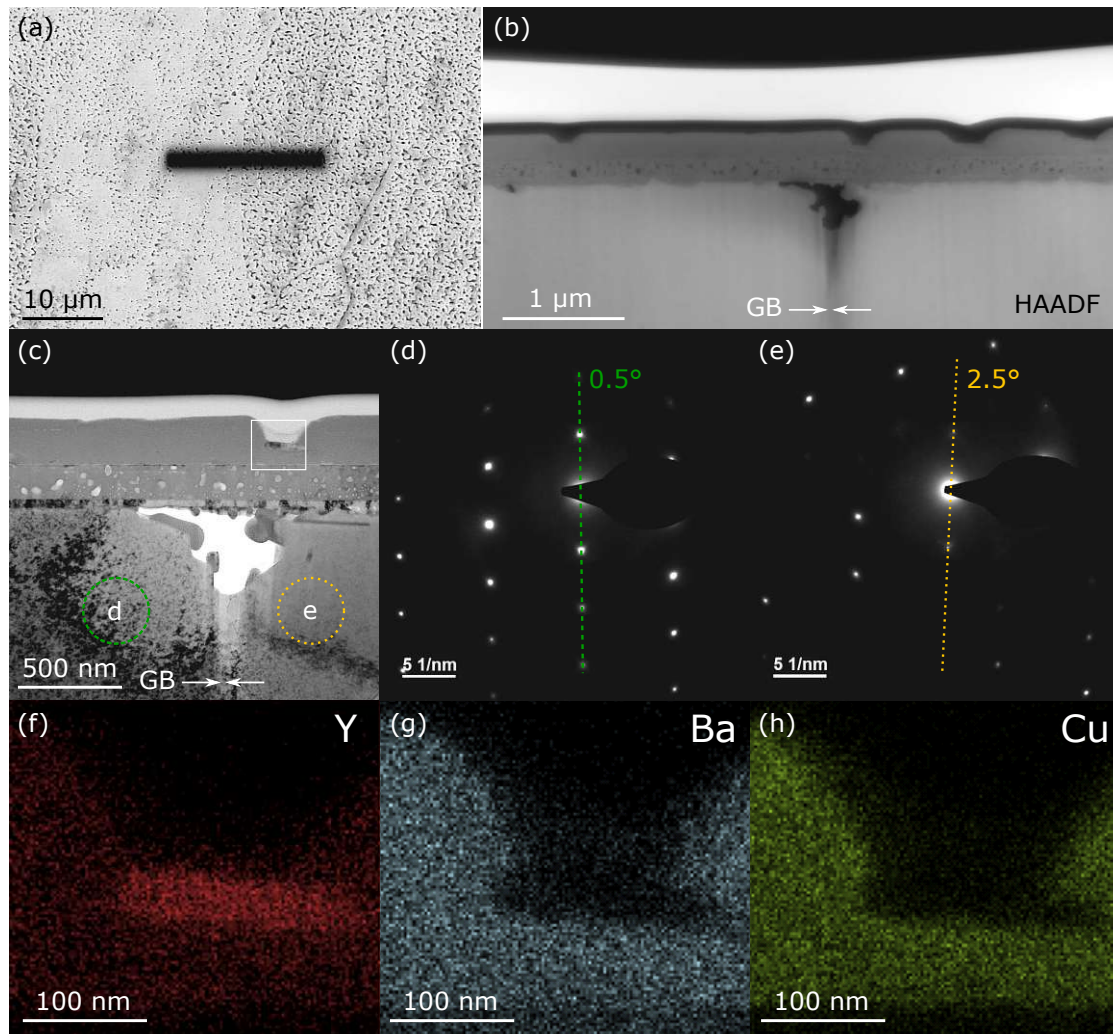


Figure D.4: TEM images of the 250 nm pure YBCO film. SEM image of the area where the TEM lamella was prepared across a GB with current flow on the left and no current flow on the right side of the GB (a). A HAADF TEM image gives an overview of the lamella, the GB in the substrate is indicated by white horizontal arrows (b). While the superconducting layer appears quite homogeneous on the left side of the GB, many pores are visible on the right side of the GB. A TEM image shows a closeup of the GB region (c). The diffraction pattern of the substrate on the left side of the GB reveals an out-of-plane tilt of 0.5° (d), while on the right side of the GB, an out-of-plane tilt of 2.5° can be observed (e). EDX elemental mapping indicates the presence of Y_2O_3 platelets in the superconducting layer, as can be seen in the elemental maps of Y (f), Ba (g) and Cu (h). Pores tend to originate at these secondary phase precipitates, as indicated by the white rectangle in (c).

Curriculum Vitae

Personal Information

Name Sigrid Kagerbauer, née Holleis
Date of birth January 6th 1990
Nationality Austrian

Academic Career

2016 – 2022 **Atominstitut, TU Wien**
Ph.D. studies in the research group for Low Temperature Physics and Superconductivity.
Local Currents in Granular High Temperature Superconductors

04/2015 – 11/2015 **Argonne National Laboratory, Illinois, USA**
Research for Master thesis in the Superconductivity and Magnetism group in the Materials Science Division.
Enhancing the High Field Performance of YBCO Coated Conductors

2013 – 2016 **TU Wien**
Master studies in physics.

10/2013 – 1/2014 **Atominstitut, TU Wien**
Bachelor thesis in the research group for Applied Quantum Physics.
Mechanical Strength of Silica Nanofibers

02/2011 – 06/2011 **Universitat Politècnica de València, Spain**
Studies in physics within the Erasmus exchange program.

2008 – 2013 **TU Wien**
Bachelor studies in physics.

2000 – 2008 **Amerlinggymnasium, Vienna**
Secondary school with emphasis on languages.

Publications

S. Holleis, I. A. Shipulin, R. Hühne, J. Bernardi and M. Eisterer; *Reduced granularity in BHO-doped YBCO films on RABiTS templates*; Superconductor Science and Technology, 35, 104001 (2022)

S. Holleis, A. A. Thomas, I. A. Shipulin, R. Hühne, A. Steiger-Thirsfeld, J. Bernardi and M. Eisterer; *Magnetic granularity in PLD-grown Fe(Se,Te) films on simple RABiTS templates*; Superconductor Science and Technology, 35, 074001 (2022)

I. A. Shipulin, A. A. Thomas, **S. Holleis**, M. Eisterer, K. Nielsch and R. Hühne; *Effect of silver doping on the superconducting and structural properties of YBCO films grown by PLD on different templates*; Materials, 15, 5354 (2022)

A. Zampa, **S. Holleis**, A. Badel, P. Tixador, J. Bernardi and M. Eisterer; *Influence of Local Inhomogeneities in the REBCO Layer on the Mechanism of Quench Onset in 2G HTS Tapes*; IEEE Transactions on Applied Superconductivity, 32(3), 6600807 (2022)

S. Ishida, D. Kagerbauer, **S. Holleis**, K. Iida, K. Munakata, A. Nakao, A. Iyo, H. Ogino, K. Kawashima, M. Eisterer and H. Eisaki; *Superconductivity-driven ferromagnetism and spin manipulation using vortices in the magnetic superconductor EuRbFe₄As₄*; PNAS, 118(37), 2101101118 (2021)

A. A. Thomas, I. A. Shipulin, **S. Holleis**, M. Eisterer, K. Nielsch and R. Hühne; *Comparative study of Fe(Se,Te) thin films on flexible coated conductor templates and single-crystal substrates*; Superconductor Science and Technology, 34, 115013 (2021)

A. Leveratto, A. Saba, **S. Holleis**, M. Himmelreich, B. Henrist, S. Fernandez-Peña, A. Moros, J. Bernardi, M. Eisterer, C. Bernini, R. Vaglio, M. Putti, C. Ferdeghini, S. Calatroni and E. Bellingeri; *Future Circular Collider beam screen: progress on Tl-1223 HTS coating*; Superconductor Science and Technology, 33, 054004 (2020)

M. Leroux, K. J. Khilstrom, **S. Holleis**, M. W. Rupich, S. Sathyamurthy, S. Fleshler, H. P. Sheng, D. J. Miller, S. Eley, L. Civale, A. Kayani, P. M. Niraula, U. Welp, and W.-K. Kwok; *Rapid doubling of the critical current of YBa₂Cu₃O_{7-δ} coated conductors for viable high-speed industrial processing*; Applied Physics Letters, 107, 192601 (2015)

S. Holleis, T. Hoinkes, C. Wuttke, P. Schneeweiss and A. Rauschenbeutel; *Experimental stress – strain analysis of tapered silica optical fibers with nanofiber waist*; Applied Physics Letters, 104, 163109 (2014)